Investigation on the Mechanical Behavior of Paper and Paper Stacks in the out-of-plane Direction

Vom Fachbereich Maschinenbau

an der Technischen Universität Darmstadt

zur

Erlangung des Grades des Doktor-Ingenieurs (Dr.-Ing.)

genehmigte

D i s s e r t a t i o n

vorgelegt von

Jian Chen, M.Sc.

aus Shandong, China

Berichterstatter: Prof. Dr.-Ing. Edgar Dörsam

Mitberichterstatter: Prof. Dr.-Ing. Samuel Schabel

Tag der Einreichung: 27.06.2016

Tag der mündlichen Prüfung: 01.11.2016

Darmstadt, 2016

D17

Erklärung

Hiermit erkläre ich, dass ich die vorliegende Arbeit, abgesehen von den in ihr ausdrücklich genannten Hilfen, selbständig verfasst habe.

Darmstadt, den 14. November. 2016

Jian Chen

Investigation on the Mechanical Behavior of Paper and Paper Stacks in the out-of-plane Direction

Abstract

The purpose of the present study is to deeply investigate the mechanical behavior of paper materials in the out-of-plane direction, especially, the compressive behavior of a single sheet or multiple sheets. In this dissertation, the mechanical behavior of paper and paper stacks was detailed discussed from three different research perspectives.

The surface roughness plays a very important role in the compressive behavior of paper materials. The first goal of the present study is to investigate the effect of the surface topography in calculating the stress-strain curve of paper. The difference between the actual and the nominal contact area was compared and a new experimental method by using carbon papers was proposed to measure the actual contact areas. With the aid of the image processing technology, the actual stress-strain curve of paper was calculated and compared with the nominal stress-strain curve. As indicated, there is an obvious difference between the actual and nominal stress-strain curves.

A second goal of this study is to establish the mathematical model for describing the force-deformation behavior of multiple sheets. Two different methods with and without considering the paper structures were selected for building the paper models. With considering the structure, the paper can be regarded as an elastic material, the body of which can be divided into two rough surfaces and one internal structure. On the basis of Hooke's law or Paetow's method, the relationship between the total deformation and surface deformation can be calculated by using the Newton-Raphson method. Then, the force-deformation relation of a single sheet was derived according to the relationship between the surface and total deformation, the model of a single sheet was extended to calculate the force-deformation curves of multiple sheets. Without considering the structure, the loading and unloading stress-strain curve of paper were expressed by using a sextic polynomial equation and a modified exponential equation, respectively. Based on the hypothesis that when the force is the same, the deformations of the paper stacks are directly proportional to the sheet numbers, the force-deformation relation of multiple sheets was derived. By comparing with the experimental results, it shows that the maximum number of sheets which can be calculated by both of the proposed models is about 140 sheets, especially, when the numbers are between 20 and 140.

In addition, without considering the effect of the surface roughness, the stress-strain curve of paper is a typical J-shaped curve. So, in this dissertation, a much easier way to simulate the paper material by using a gasket model was proposed. The material property was defined based on the experimental stress-deformation data under 100 N, then, some simulations under 20 N, 40 N, 60 N and 80 N were implemented based on the model established above. The findings indicated that, this method can be used with high confidence for the simulation of paper under different forces.

Kurzfassung

Das Ziel der vorliegenden Arbeit ist das mechanische Verhalten von Papiermaterialien in z-Richtung genauestens zu untersuchen, insbesondere das Pressverhalten von einem einzelnen Blatt oder mehreren Blättern. In dieser Arbeit wurde das mechanische Verhalten von Papier und Papierstapel aus drei unterschiedlichen Forschungsperspektiven detailliert diskutiert.

Die Oberflächenrauigkeit spielt beim Pressverhalten von Papiermaterialien eine sehr wichtige Rolle. Das erste Ziel der vorliegenden Arbeit ist es der Wirkung der Oberflächentopographie bei der Berechnung der Spannungs-Dehnungs-Kurve des Papiers zu untersuchen. Verglichen wurde die Differenz zwischen der tatsächlichen Kontaktfläche und der Nennkontaktfläche. Des Weiteren wurde eine neue experimentelle Methode vorgeschlagen, bei dem Kohlepapier angewandt wird um die tatsächlichen Kontaktfläche zu messen. Mit Hilfe der Bildverarbeitungstechnik wird die tatsächliche Spannungs-Dehnungskurve des Papiers berechnet und mit der Nennspannungs-Dehnungskurve verglichen. Wie schon angedeutet, besteht zwischen den Ist- und Soll-Spannungs-Dehnungs-Kurven eine offensichtliche Differenz.

Ein weiteres Ziel dieser Arbeit ist das mathematische Modell zur Beschreibung des Kraft-Verformungsverhalten von mehreren Blättern zu etablieren. Zwei verschiedene Methoden, mit und ohne Berücksichtigung der Papierstrukturen, werden für den Aufbau der Papiermodelle ausgewählt. Unter Berücksichtigung der Papierstruktur, kann das Papier als elastisches Material angesehen werden, dessen Körper in zwei raue Oberflächen und einer inneren Struktur unterteilt wird. Auf der Grundlage des Hookschen Gesetzes oder der Paetow Methode kann die Beziehung zwischen der Gesamtverformung und Oberflächenverformung durch Verwendung der Newton-Raphson-Methode berechnet werden. Dann wurde das Kraft-Verformungsverhalten der einzelnen Blätter abgeleitet und entsprechende Beziehungen zwischen der Oberfläche und der Gesamtverformung, das Modell des einzelnen Blattes wird erweitert, um weiterhin die Kraft-Verformungskurven von mehreren Blättern berechnen zu können. Ohne Berücksichtigung der Papierstruktur wird die Be- und Entlastung der Spannungs-Dehnungs-Kurve des Papiers jeweils durch eine Sextik Polynomgleichung und eine modifizierte exponentielle Gleichung ausgedrückt. Basierend auf der Hypothese, dass unter gleicher Kraft die Verformungen der Papierstapel direkt proportional zu den Blattnummern sind, wird die Kraft-Verformungs-Beziehung von mehreren Blättern abgeleitet. Durch den Vergleich mit den experimentellen Ergebnissen zeigt sich, dass die maximale Anzahl von Blättern, die von beiden der vorgeschlagenen Modelle, mit etwa 140 Blatt berechnet werden kann.

Darüber hinaus, ohne dabei den Effekt der Oberflächenrauigkeit zu berücksichtigen, ist die Spannungs-Dehnungs-Kurve des Papiers eine typische J-förmige Kurve. In dieser Arbeit wird ein viel einfacherer Weg vorgeschlagen, um das Papiermaterial durch die Verwendung eines Dichtungs Modell zu simulieren. Die Materialeigenschaft wurde auf Grundlage der Daten des experimentellen Druckverschlusses unter 100 N definiert, dann wurden einige Simulationen unter 20 N, 40 N, 60 N und 80 N basierend auf dem oben etabliert Modell umgesetzt. Aus den Ergebnissen zeigt sich, dass dieses Verfahren mit hoher Wahrscheinlichkeit für die Simulation von Papier unter verschiedenen Kräften verwendet werden kann.

Acknowledgements

I would like to express my gratitude to all those who helped me during the writing of this dissertation.

First of all, I gratefully acknowledge the help of my supervisor Prof. Edgar Dörsam, who gave me this opportunity to finish my Ph.D study in IDD (Institut für Druckmaschinen und Druckverfahren, TUD). In the preparation of the dissertation, he has spent much time reading through each draft and provided me with inspiring advice. Without his patient instruction and expert guidance, the completion of this thesis would not have been possible.

I also would like to thank Prof. Samuel Schabel from PMV (Fachgebiet Papierfabrikation und Mechanische Verfahrenstechnik, TUD) as the co-supervisor of my dissertation. He did not hesitate to review this dissertation for spending so much of his valuable time.

I am grateful to my colleagues in IDD for all of their support, especially Dr. Jann Neumann and Dr. Dieter Spiehl as the team leaders of our group, they have offered me many valuable suggestions in the academic studies. Also, special thanks to M.Sc. Thorsten Bitsch and M.Sc. Arash Hakimi Tehrani for spending so much time in correcting my manuscript.

In addition, I would also like to thank the China Scholarship Council (File number: 201206090026) for the financial support.

At the end, I would like to thank my family: my parents, my brother and my beloved wife, for supporting me spiritually throughout my life.

Darmstadt, November 2016

Contents

Symbols and Abbreviations

Greek Symbols

Symbol	Unit	Description
σ	(MPa)	Stress
σ_1	(MPa)	Stress of the surface structure
σ_2	(MPa)	Stress of the internal structure
σ_m	(MPa)	Stress of a random selected point in the unloading stage
σ_y	(MPa)	Stress at the start point of unloading
ε	(-)	Strain
ε_1	(-)	Strain of the surface structure
ε_2	(-)	Strain of the internal structure
ε_m	(-)	Strain of a random selected point in the unloading stage
ε_r	(-)	Residual strain
ε_y	(-)	Strain at the start point of unloading
α, β	(-)	Coefficients of the exponential unloading function

Latin Symbols

Symbol	Unit	Description
a, b, c, d	(-)	Coefficients for determining the relationship between strain and stress
$a_i (i=0,\ldots 6)$	(-)	Coefficients of the polynomial loading function
A	(mm^2)	Measured area for calculating the areal roughness

$\mathbf{A_0}$	(mm^2)	Nominal contact area
A(z)	(mm^2)	Actual contact area, which is changing with deformation z
$\mathbf{A(z_1)}$	(mm^2)	Real contact area of the surface structure
$\mathbf{A(z_2)}$	(mm^2)	Real contact area of the internal structure
$\mathbf{A_{mea}}$	(mm^2)	Measured contact area, which is regarded as equivalent to the actual contact area A(z)
$\mathbf{A_{ind}}$	(mm^2)	Nominal area of the indenter, which is equal to the value of the nominal contact area A_0
$\mathbf{b_i(i=0,\ldots4)}$	(-)	Coefficients for determining the relationship between surface deformation and total deformation (cubic curve fitting)
$\mathbf{B_0, B_1, B_2}$	(mm^4)	Coefficients for simplifying the functions
$\mathbf{c_0}$	(mm)	Width of the contact area happened in the circle element
$\mathbf{c_1, c_2}$	(-)	Coefficients for determining the relationship between surface deformation and total deformation (linear curve fitting)
d	(%)	Deviation
$\mathbf{d_{diameter}}$	(mm)	Diameter of the cylindrical indenter
$\mathbf{d_{thickness}}$	(mm)	Thickness of the copy paper
$\mathbf{e_{all}}$	(-)	Allowed error for calculating the root in the Newton-Raphson method
E	(MPa)	E-modulus, which is a constant value
$\mathbf{E^{ini}}$	(MPa)	Initial E-modulus
E(z)	(MPa)	Actual modulus, which is changing with deformation
$\mathbf{E(z_1)}$	(MPa)	Elastic modulus of the surface structure
$\mathbf{E(z_2)}$	(MPa)	Elastic modulus of the internal structure
$\mathbf{E(z_3)}$	(MPa)	Elastic modulus of the surface structure
F	(N)	Force
F(z)	(N)	Force when the deformation is z

$\mathbf{F^{l}_{loading}}$	(N)	Force applied to one sheet in the loading stage
$\mathbf{F(z_2)}$	(-)	Function built for the Newton-Raphson method
$\mathbf{F^{l}_{unloading}}$	(N)	Force applied to one sheet in the unloading stage
$\mathbf{F^{n}_{loading}}$	(N)	Force applied to n sheets in the loading stage
$\mathbf{F^{n}_{unloading}}$	(N)	Force applied to n sheets in the unloading stage
$\mathbf{h_1, h_2, h_3}$	(mm)	Initial heights of the different paper structures
$\mathbf{i_{max}}$	(-)	Desired maximum iteration times in the Newton-Raphson method
$\mathbf{k_{loading}}$	(-)	Slope in loading stage used for showing the relationship between deformation and the number of sheets
Unloading	(-)	Slope in unloading stage used for showing the relationship between deformation and the number of sheets
l	(µm)	Sampling length for calculating the profile roughness
$\mathbf{l_0}$	(µm)	Original length or thickness of the material
L	(µm)	Contact length of the fibers
$\mathbf{m_0, n_0}$	(-)	Parameters used to determine the amount of internal units
n	(-)	Number of sheets
p	(%)	Percentage of the plastic strain (deformation)
P	(MPa)	Corresponding pressure applied to the paper
$\mathbf{p_1, q_1, r_1}$	(-)	Coefficients of the equation between β and ε_y
$\mathbf{p_2, q_2}$	(-)	Coefficients of the equation between ε_r and ε_y
$\mathbf{p_3, q_3}$	(-)	Coefficients for determining the loading exponential function
$\mathbf{p_4, q_4, r_4}$	(-)	Coefficients for determining the unloading exponential function
$\mathbf{R_a}$	(µm)	Average profile roughness
$\mathbf{R_A}$	(µm)	Average value of surface roughness plus standard deviation

		of caliper
$\mathbf{R_r}$	(mm)	Radius of curvature at the point (line) where the fibers contact each other
s	(mm)	Standard deviation of the caliper
S	(MPa)	Limiting stress
$\mathbf{S_a}$	(µm)	Average areal roughness
$\mathbf{S_q}$	(µm)	Root mean square roughness
w	(mm)	Fiber width
W(z)	(MPa)	Actual contact pressure
z	(mm)	Deformation of paper in the out-of-plane direction
$\mathbf{z_1}$	(mm)	Deformation of the surface structure
$\mathbf{z_2}$	(mm)	Deformation of the internal structure
$\mathbf{z_3}$	(mm)	Deformation of the surface structure
$\mathbf{z_4}$	(mm)	Average paper-paper contact deformation
$\mathbf{z_r}$	(mm)	Residual (plastic) deformation
$\mathbf{z^n}$	(mm)	Total deformation of n sheets under 100N
$\mathbf{z^1_{loading}}$	(mm)	Deformation of one sheet in the loading stage
$\mathbf{z^1_{unloading}}$	(mm)	Deformation of one sheet in the unloading stage
$\mathbf{z^n_{loading}}$	(mm)	Deformation of n sheets in the loading stage
$\mathbf{z^n_{unloading}}$	(mm)	Deformation of n sheets in the unloading stage
Z(x)	(µm)	Profile heights
Z(x, y)	(µm)	Areal heights

Abbreviations

2D	Two dimensional
3D	Three dimensional
CD	Cross direction
MD	Machine direction
ZD	Through-thickness direction or out-of-plane direction
ABAQUS	A software suite for finite element analysis and computer-aided engineering, from ABAQUS Inc., USA
ANSYS	Engineering analysis software for finite element analysis, computational fluid dynamics, heat transfer, etc., which is from Ansys, Inc., USA
DIN	German Institute for Standardization
FEM	Finite element method, which is also referred to as finite element analysis (FEA)
IDD	Institute of Printing Science and Technology, Technische Universität Darmstadt
LWC-paper	Light weight coated paper
MATLAB	Matrix laboratory: numerical computing software from Mathworks, USA

1 Introduction

Paper is a versatile material with many uses. It is the ideal material not only for writing, but also for printing, packaging, cleaning and a number of industrial and construction processes. Today, paper materials can be found everywhere, used by everyone, every day. It has become one of the most widely used materials all around the world.

1.1 Motivation

Papermaking history

Paper has a long history stretching back to ancient Egypt in the third millennium BC. The word ‘‘paper’’ is derived from papyrus. Cyperus papyrus is a plant that was once abundant in Egypt and which was used to produce a thick, paper-like material by the ancient Egyptians, Greeks and Romans. Papyrus, however, is the predecessor of paper that is collectively known by the generic term ‘‘tapa’’ and which were mostly made from the inner bark of the paper mulberry, fig and daphne trees (Paperonline, 2015a).

As shown in Figure 1.1, the papermaking process is known to have been invented in ancient China during the Han dynasty (206 BC – 220 AD) and spread slowly to the west via the Silk Road. Papermaking and manufacturing in Europe was started by Muslims living on the Iberian Peninsula (today's Portugal and Spain), and Sicily in the 10^{th} century, and slowly spread to Italy and Southern France reaching Germany by 1400.

The craft of papermaking spread throughout the world and remained a relatively small-scale, artisan activity until paper production became industrialized during the 19^{th} century. Originally intended purely for writing and printing purposes, a dazzling array of paper products is available to today's consumer (Paperonline, 2015a).

The invention and application of the paper have played a significant role in promoting the progress of human civilization, even in the age of digital media. Until now, its influence is still continually expanding.

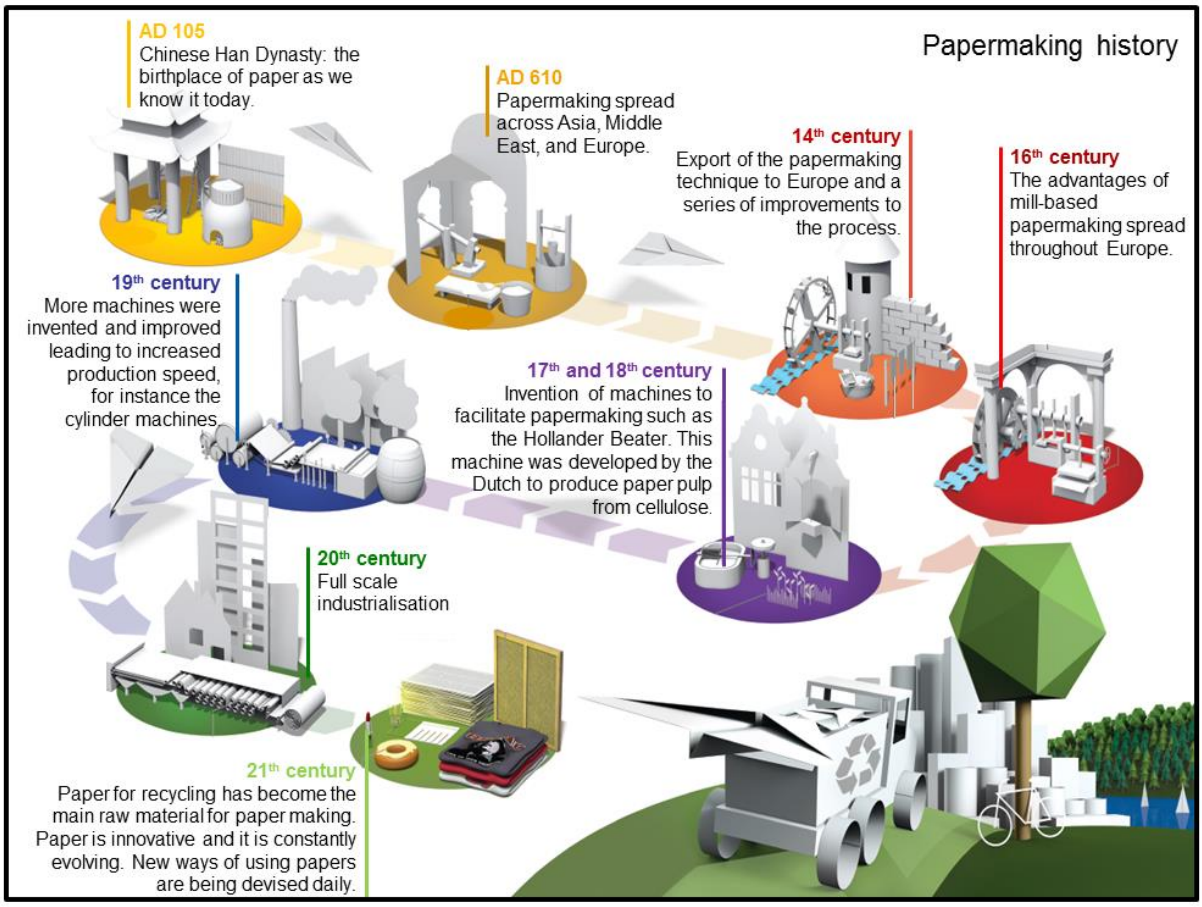

Figure 1.1: Diagram of the papermaking history cited from (Paperonline, 2015a). It describes the general historical background of papermaking. The history of paper can date back almost 2000 years to the Han dynasty of China. In the 19th century, paper production became industrialized with the inventions of papermaking machines.

Papermaking process

World-wide, paper is mostly produced from cellulose fibers. Generally, the fibers are those found naturally in softwood trees, hardwood trees, or other plants. The fibers can also come from recycled paper, such as from newspapers, old corrugated boxes, mixed paper, even recycled clothes. The first step of manufacturing paper is to convert the materials mentioned above to cellulosic pulp.

Detailed papermaking process can be seen from Figure 1.2. First of all, whole trees (Wood) must be cut into manageable lengths, and then their bark which cannot be used for papermaking is stripped (De-barking) from the logs. After being washed, the stripped logs are sent to a huge machine and chipped (Chipping) into small pieces. The cellulose fibres separated from the small wood pieces are called pulp. Basically, there are two different ways to break down the pulp used to make paper: chemically (Chemical Pulping) and mechanically (Mechanical Pulping). But it is not necessary to pulp recycled fibers (Paper for Recycling) in either of these two ways because they have already been treated before. The paper for

recycling is disintegrated into pulp (Pulping) to separate the component fibers. Adhesives and ink are removed (De-ink) using a flotation process. Fibers are then washed (Cleaning), screened and dried. Pulp is ready to be used directly or it can be bleached into white paper.

The function of the headbox (Headbox) is to evenly spread the highly diluted fiber mixture over the endless moving wire mesh (Wire Section) of the papermaking machine. The mixture runs through a slit onto a flat, fibers deposit themselves next to and on top of one another on the wire section. At the same time, water runs through the wire or sucked off from below. Here the fibers start to spread and consolidate into a thin mat. This process is called “sheet formation”. However, at the end of this process, the paper sheet or web still contains 80% water.

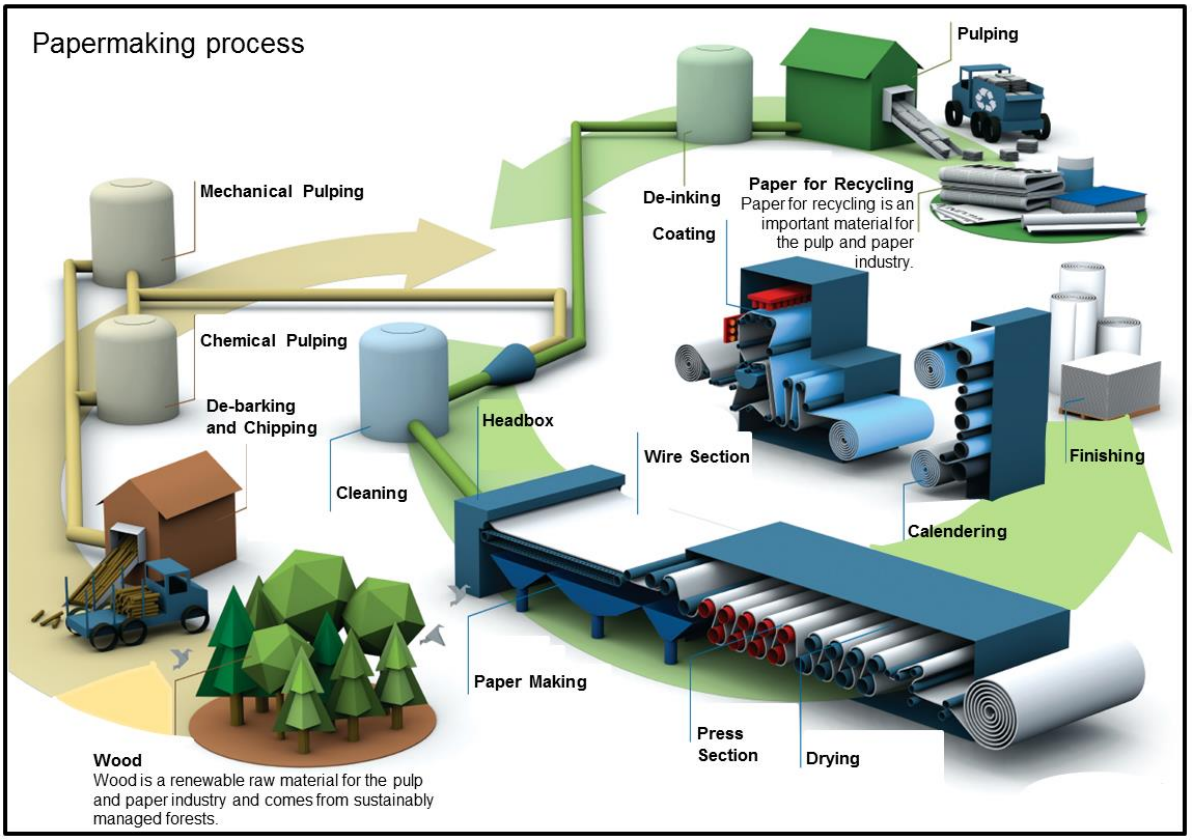

Figure 1.2: Diagram of the papermaking process taken from (Paperonline, 2015b). This simple diagram details the papermaking process and illustrates the use of wood and paper for recycling. Some post-treatment processes, such as calendaring, coating and finishing are also mentioned.

After the formation of the sheet, the paper sheet has to be further drained and compressed (Press Section) by passing through a series of steel rollers, in which process the most important properties of the sheet will be determined, not only more water is squeezed but also the sheet is stiffed. When the paper leaves the press section, it has a dry content of up to 50-55%. Then in the dryer section (Drying), the remaining excess water has to be removed by a succession of heated drying cylinders.

In some paper machines, which have an extra smoothing process called calendaring (Calendaring), by which the paper after drying will be further compacted and smoothed between rollers under high pressure. To meet some special demands, the surface of some raw paper should be further improved, such as by the method of paper coating (Coating). In the coating process, coating color is spread onto the paper surface. Coating the paper (especially, several times) often improves its printing properties. High-grade printing paper is coated up to 3 times. After coating, the paper should be calendared by the super-calendars.

In the final stage of the paper making process, paper rolls are wound into a reel or cut into sheets (Finishing), ready for printing and converting. The nature of paper and papermaking has changed very little over the past 150 years (Bajpai, 2011).

Levels of observation

During the production process, from the selection of raw materials to the process of pulp making, from the process of paper making to paper calendaring or coating, in different stages, the paper materials can be modelled at different structural levels. Depending on different research backgrounds and purposes, the observation levels can be classified in categories ranging from cellulose to a machine level (Monica et al., 2009, Heyden, 2000). For paper materials, each modelling level has particular advantages and disadvantages, as shown in Table 1.1.

Table 1.1: Different levels of observation used in the papermaking process.

Structure	Length (m)	Level of observation	Literature
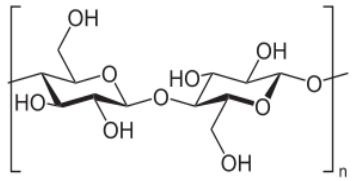	Nano 10^{-9} m	cellulose	· Persson, 2000
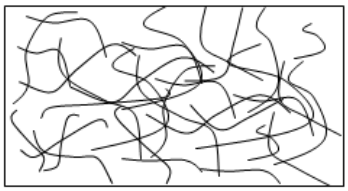	micro 10^{-6} m	fibre and network	· Bronkhorst, 2003 · Ekman et al., 2012 · He, 2005 · Heyden, 2000 · Lavrykov et al., 2012 · Madrigal, 2013 · Marulier et al., 2012 · Picu, 2011 · Strömbro and Gudmundson, 2008

			· Vincent et al., 2005
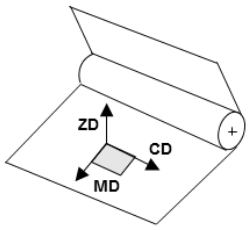	macro 10^{-2} m	paper sheet	· Andersson, 2006 · Monica et al., 2009 · Stenberg, 2002
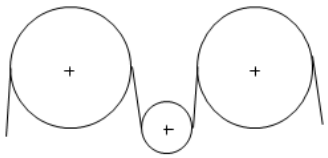	machine 10^{0} m	moving web (machine)	· Beex and Peerlings, 2009 · Eckstein, 2014 · Eckstein and Hagedorn, 2014 · Huang et al., 2014 · Nagasawa et al., 2003 · Nygårds et al., 2009 · Simon et al., 2014

Cellulose is found in large amounts in nearly all plants, and is potentially a major food source. Cellulose is a long chain of linked sugar molecules that gives wood its remarkable strength. It is the main component of plant cell walls, and the basic building block for many textiles and for paper. In the laboratory, ashless filter paper is a source of nearly pure cellulose. Cotton is the purest natural form of cellulose. Cellulose fibers in wood are bound in lignin, a complex polymer. Papermaking involves treating wood pulp with alkalis or bisulfites to disintegrate the lignin, and then pressing the pulp to matte the cellulose fibers together. The aim of the research in this level is to understand the influence of hydrogen bonding on the sheet properties. Very few models on the fiber level and below exist to predict mechanical behavior (Persson, 2000).

Tensile strength is the most commonly used parameter for describing the mechanical properties of a sheet of paper, the important parameters for tensile strength of paper include fiber length, fiber strength, bond strength, relative bonded area (RBA), number of fiber-fiber contacts, dimensions of fiber cross-section and apparent density, and so on (He, 2005). There is a great number of research works (Ekman et al., 2012, Madrigal, 2013, He, 2005, Heyden, 2000, Lavrykov et al., 2012, Marulier et al., 2012, Vincent et al., 2005, Bronkhorst, 2003, Strömbro and Gudmundson, 2008, Picu, 2011) related to the fiber and network level, by which the influence of fiber and bond properties on sheet properties was predicted, the paper formation process was also simulated.

From the level of paper sheet, the mechanical behavior of paper structure can be predicted. The manufacturing process has the effect, that most of the fibers are oriented in the direction of the machine and that almost no fibers are oriented in the through-thickness direction. This phenomenon leads to the anisotropy of paper. The paper is usually treated as an orthotropic

material and the three different directions (MD, CD and ZD) of the paper machine are used as principle directions of the paper, as shown in Table 1.1. The paper is highly anisotropic with the stiffness in the machine direction (MD) being 1-5 times larger than in the cross direction (CD), and around 100 times larger than in the through-thickness direction (ZD) (Andersson, 2006, Monica et al., 2009, Stenberg, 2002). MD and CD directions are also called in-plane directions and ZD direction is also called the **out-of-plane direction**. Most of the research works presented up to now are mainly focused in this level.

The research in the moving web (machine) level mainly focused on building the models for paper web together with the papermaking machine or the calendaring machine (Eckstein, 2014, Eckstein and Hagedorn, 2014). To illustrate the end use products, some processes such as the folding or creasing of paperboard were investigated (Beex and Peerlings, 2009, Nagasawa et al., 2003, Nygårds et al., 2009, Simon et al., 2014, Huang et al., 2014).

Research in the level of paper sheet

As mentioned above, the properties of paper have been studied in numerous papers. But until now, it is still very hard to build a unified model which can be used for paper or paper stacks. According to different classification criteria, the paper models can be classified into various groups, as shown in Table 1.2.

Table 1.2: Classification of paper models. According to different classification criteria, the paper models can be classified into various groups.

Classification criteria	Types of models	Literature
Essential physical characteristics	Constitutive	· Andersson, 2006 · Gavelin, 1949 · Mäkelä and Östlund, 2003 · Ramasubramanian and Wang 2007 · Ribeiro and Costa, 2007 · Stenberg, 2003 · Xia et al., 2002
	Non-constitutive	· Paetow and Göttsching, 1990 · Pfeiffer, 1981 · Schaffrath and Gottsching, 1991 · Schaffrath and Göttsching, 1992b · Schaffrath, 1993
Surface topography	Rough surface	· Alam, 2012 · Alam et al., 2011 · Pino and Pladellorens, 2009 · Schaffrath and Gottsching, 1991 · Schaffrath, 1993 · Schaffrath and Göttsching, 1992b · Teleman et al., 2004

	Smooth solid	· Andersson, 2006 · Eckstein, 2014 · Eckstein and Hagedorn, 2014 · Kaulitz, 2009 · Kaulitz and Dörsam, 2008	· Pfeiffer, 1981 · Rättö, 2005 · Ribeiro and Costa, 2007 · Simon et al., 2014 · Stenberg, 2002 · Stenberg, 2003 · Teleman et al., 2004
Direction of the applied force	In-plane	· Alam, 2012 · Alam et al., 2011 · Bronkhorst, 2003 · Kaulitz and Dörsam, 2008	· Mäkelä and Östlund, 2003 · Paetow and Göttsching, 1990 · Simon et al., 2014 · Xia et al., 2002
	Out-of-plane	· Gavelin, 1949 · Huang et al., 2014 · Ivarsson, 1956 · Nagasawa et al., 2003 · Pfeiffer, 1981 · Pino and Pladellorens, 2009 · Rättö, 2005	· Ribeiro and Costa, 2007 · Stenberg, 2002 · Stenberg, 2003 · Schaffrath and Gottsching, 1991 · Schaffrath and Göttsching, 1992b · Schaffrath, 1993
	Both in and out-of planes	· Andersson, 2006 · Kaulitz, 2009 · Nygårds et al., 2005	· Nygårds et al., 2009 · Stenberg, 2003
Research methods	Experimental	· Alam, 2012 · Alam et al., 2011 · Beex and Peerlings, 2009 · Gavelin, 1949 · Huang et al., 2014 · Kaulitz and Dörsam, 2008 · Kaulitz, 2009 · Nygårds et al., 2005 · Nagasawa et al., 2003	· Pino and Pladellorens, 2009Rättö, 2005 · Ramasubramanian and Wang, 2007 · Schaffrath and Gottsching, 1991 · Schaffrath, 1993 · Schaffrath and Göttsching, 1992b · Simon et al. · Singh, 2008, 2014 · Teleman et al., 2004
	Simulation	· Andersson, 2006 · Beex and Peerlings, 2009 · Huang et al., 2014	· Nygårds et al., 2009 · Ramasubramanian and Wang, 2007 · Ribeiro and Costa, 2007

		· Lavrykov et al., 2012 · Mäkelä and Östlund, 2003 · Nygårds et al., 2005	· Simon et al., 2014 · Stenberg, 2003
	Analytical	· Andersson, 2006 · Gavelin, 1949 · Kaulitz, 2009 · Nagasawa et al., 2003 · Paetow and Göttsching, 1990 · Pfeiffer, 1981 · Ramasubramanian and Wang 2007	· Ribeiro and Costa, 2007 · Schaffrath, 1993 · Schaffrath and Gottsching, 1991 · Schaffrath and Göttsching, 1992b · Stenberg, 2003 · Xia et al., 2002

Based on the law of the essential physical characteristics of materials, the models of paper materials can be divided into constitutive models (Ramasubramanian and Wang, 2007, Xia et al., 2002, Stenberg, 2003, Andersson, 2006) and non-constitutive models (Schaffrath and Gottsching, 1991, Schaffrath, 1993, Schaffrath and Göttsching, 1992b). Generally, the constitutive models are used to describe the response behavior of natural and manufactured materials under different mechanical and environmental conditions, which describe the physical properties of a given material. For constitutive models of paper materials, the properties such as elasticity, plasticity and viscosity were modelled, respectively, by using spring, dry friction and dashpot elements (Ribeiro and Costa, 2007, Gavelin, 1949). According to this method, the differences of these constitutive models mainly lie in the different combinations of these elements. A considerable number of free parameters are needed by doing experiments in these constitutive models. Moreover, most of these parameters are very difficult to be measured (Stenberg, 2003, Xia et al., 2002, Andersson, 2006).

According to the surface topography, the analysis models of paper can be divided into rough surface models and smooth solid models. Generally, the paper is modelled as smooth solid material, the ignorance of the surface roughness brings lots of convenience for analyzing the processes such as paper delivery and paper calendaring (Eckstein, 2014, Eckstein and Hagedorn, 2014). The surface topographical differences between the cross direction and the machine direction for newspaper and paperboard was investigated (Alam, 2012, Alam et al., 2011). When compressing thin sheets, it is very important to be aware of the influence of surface roughness (Rättö, 2005). The surface topography plays an important role in obtaining the stress-strain curve of paper materials. The influence of surface roughness was also discussed in some papers. For example, the paper surface topography under compression was studied by Teleman (Teleman et al., 2004). According to the surface topography, the paper body was considered as being composed of two rough surfaces and an internal structure, the

force-deformation relationship of paper was derived by using the Newton formula (Schaffrath and Göttsching, 1992b, Schaffrath and Göttsching, 1992a).

According to the direction of the applied force, the models can be classified as in-plane (Mäkelä and Östlund, 2003, Bronkhorst, 2003, Xia et al., 2002, Kaulitz and Dörsam, 2008, Paetow and Göttsching, 1990) or out-of-plane models (Stenberg, 2002, Stenberg, 2003, Gavelin, 1949, Ivarsson, 1956, Nagasawa et al., 2003). Each of them can also be further subdivided into tension or compression researches. In some models, that the paper was described as a three-dimensional engineering material, the in-plane and out-of-plane behavior were combined together (Kaulitz, 2009, Andersson, 2006).

In addition, from the standpoint of research methods, the research of paper can also be classified as experimental, simulation or mathematical analysis (Ribeiro and Costa, 2007), etc. Different experimental methods were evaluated for characterizing the smoothness of handsheets (Nygårds et al., 2005, Pino and Pladellorens, 2009, Singh, 2008). Only very few references attempt to establish a simulation model in finite element (FEM) software (Mäkelä and Östlund, 2003, Ramasubramanian and Wang, 2007, Andersson, 2006, Lavrykov et al., 2012, Nygårds et al., 2005, Beex and Peerlings, 2009, Huang et al., 2014, Nygårds et al., 2009, Simon et al., 2014). But even in those which have been done, the results remained inconclusive in some respects. There is still no material model provided in FEM software which can be used directly for paper simulation. Furthermore, the compressive behavior of paper stack is related to the aspect that there is interaction between the individual sheets. These kinds of simulation models are also very difficult to be extended to the research of multiple sheets.

Research about the out-of-plane behavior of paper

As mentioned above, according to the direction of the applied force, the researches of paper can be divided into in-plane or out-of-plane researches. The research of this dissertation is mainly focused on the mechanical behavior of paper in the out-of-plane direction.

As shown in Figures 1.2 and 1.3, the sections of paper machines consist of headbox, wire section, press section, dryer section, and calender section. Because of this specific manufacturing process of paper materials, the mechanical behavior of paper is quite different from some other materials. The distribution and arrangement of the fiber from headbox to wire section (forming section) determine the intrinsic properties of paper materials, some essential differences between in-plane direction and out-of-plane direction generated in this process. The moisture content of paper after pressing and drying also has a big influence on the mechanical behavior of paper.

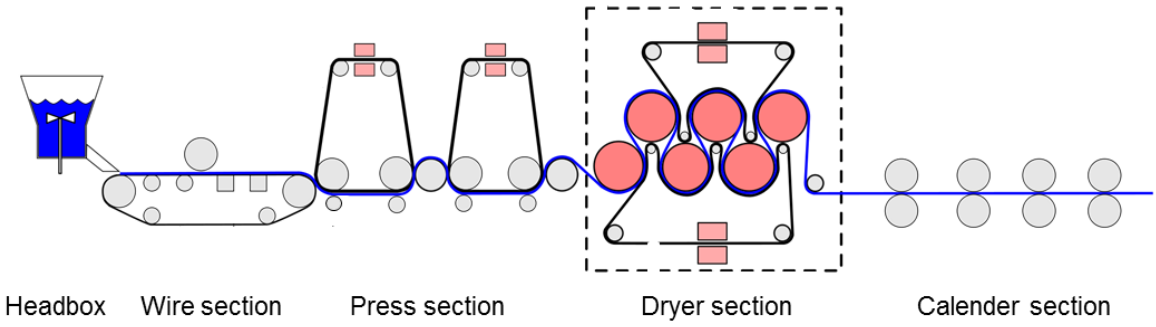

Figure 1.3: Diagram of a papermaking machine (Fourdrinier machine) taken from (Egmason, 2010). The sections of paper machine consist of headbox, wire, press, dryer and calender. Firstly, the fiber-water suspension is sprayed through a headbox onto the wire section, most of the water is drained through the wire section, and then the moisture content will be further reduced by the press section and dryer section. Finally, through the calender section, the thcikness of paper will be further compressed.

Compared to the in-plane dimensions, the thickness of paper material is very thin. It may sometimes be hard to imagine the use for an out-of-plane material model (Stenberg, 2002). However, the mechanical behavior of paper has a very close relationship with many operations in the papermaking or printing industries, such as paper calendering, counting, folding, creasing, cutting, book binding, traditional printing, and so on. In these examples, the importance of the out-of-plane behavior is enhanced. Most of these examples have been described in (Stenberg, 2002) in detail.

In spite of the mechanical behavior of paper in the out-of-plane direction is very important, but only very few publications deal with the behavior of paper materials in this direction. Because of the complexity of the material, the knowledge of the mechanical properties of paper materials in the out-of-plane direction is still not clear.

A compression tester was constructed by Ivarsson to obtain deformation curves of paper materials (Ivarsson, 1956). When the change of deformation is linear with time, the repeated load deformation curves for cellulose fiber sheet were obtained. The effect of moisture content, different pulps and beating time on the shapes of compression curves were further discussed.

Between the years 1991 and 1993, Schaffrath (Schaffrath and Gottsching, 1991, Schaffrath and Göttsching, 1992b, Schaffrath and Göttsching, 1992a, Schaffrath, 1993) divided the elastic body of paper into three parts, one internal structure and two rough surfaces, then developed the mathematical models by using two different methods and derived the force-deformation relationship of paper materials by using the Newton–Raphson method. The increase of E-modulus accompanied with increasing loading was also concerned. The elasticity and plasticity of paper stacks were also discussed according to the experimental results.

Stenberg published some articles (Stenberg, 1999, Stenberg, 2002, Stenberg, 2003, Stenberg and Fellers, 2002, Stenberg et al., 2001) between 1999 and 2003, in which he summarized the literature in this area, developed a new device to measure the stress-strain properties of paperboard in the out-of-plane direction, did some deep research about the Poisson's ratios and the out-of-plane shear, built an elastic-plastic model for paper materials.

Based on the model provided by Stenberg, some students from Ruhr-University Bochum implemented some experiments and simulations, in which the elastic-plastic model was verified (Pietryga, 2003).

For multiple sheets, the amount of published research is still quite limited. A characteristic equation for paper stacks in exponential form was proposed in (Pfeiffer, 1981), the K_1 and K_2 factors were measured for paper stacks. Based on the descriptive equations proposed by Pfeiffer (1981), the E-moduli of a single light weight coated paper (LWC-paper) as well as 500 sheets in the out-of-plane direction were calculated and compared, the problem of position shifts of multiple sheets happended in the paper winding process was investigated (Hoffmann, 2010). When the surface roughness of paper was taken into consideration, the force-deformation behavior of paper stacks was investigated (Schaffrath and Gottsching, 1991). Based on the model proposed by Schaffrath, an empirical formula was built for paper stacks to show the relationship between height and number of sheets (Diaz et al., 2009).

So until now, most of the researches are still focused on only one sheet, the paper is regarded as smooth solid material without considering the surface topography. Most of the works presented up to now are trying to build the constitutive models. The simulation work and the research about paper stacks are still not sufficient, which should be the main research direction in the future.

1.2 Objectives

In this dissertation, the author will do some research about the mechanical behavior of paper materials in the out-of-plane direction. Some works related to surface roughness, multiple sheets and paper simulation will be discussed.

The stress-strain curve of paper materials have been described in many references. Many researchers paid attention to the mechanical behavior of paper affected by the surface roughness, but the actual stress-strain curve of paper affected by the actual contact area was never investigated before.

Some previous works attempted to establish the constitutive model for a single sheet in the out-of-plane direction, but until now there's still no model for multiple sheets. The extension of the model of one sheet to multiple sheets is very difficult.

For paper simulation, which is very similar to the theoretical analysis, all the models proposed before are mainly based on the constitutive models.

According to the analysis above, the objectives of this dissertation can be summarized from three aspects:

- Finding a solution to calculate the actual stress-strain curve of paper.
- Building the mathematical model for paper stacks.
- Implementing the simulation of paper in a much easier way.

To achieve these objectives, the following research problems will be investigated and answered in this dissertation:

Firstly, the surface topography of paper is responsible for many important paper properties, such as gloss and printability. The measurement and characterization of the paper's surface structure is a very important task. The paper's surface topography can range from very rough to extremely smooth, which has also obviously influence on mechanical properties of paper materials, especially the compressive behavior. So what is the difference between the nominal and actual contact areas? How is the mechanical behavior of paper affected by the surface roughness?

Secondly, the surface of paper is not smooth, the internal structure of paper consists of many fibers, both of which play a very important role in the mechanical behavior of paper sheets. If the surface topography and the internal structure are taken into account, how can one build up the analysis models of a single sheet as well as paper stacks?

Thirdly, a mathematical descriptive model for spiral wound gasket was proposed by Takaki (Takaki and Fukuoka, 2000). Then the stress-strain relation for asbestos sheet gasket was proposed in the same way (Takaki and Fkuoka, 2001). After that, these models were widely used for calculating the stress-strain curve of gasket material (Fukuoka et al., 2007, Fukuoka and Takaki, 2003, Takaki and Fukuoka, 2002a, Takaki and Fukuoka, 2002b, Takaki and Fukuoka, 2003, Fukuoka et al., 2012, Nagata et al., 2002). So by using the same method, if it is possible to establish the descriptive model for paper material and actualize the descriptions of the stress-strain curve of a single sheet as well as the force-deformation curves of paper stacks?

Fourthly, as mentioned above, because of the complexity of the paper materials, there is still no material model provided in FEM software which can be used directly for paper simulation. All simulation works presented up to now are based on constitutive models, in which a considerable number of free parameters are needed to be obtained by experiments. Additionally, measurements of most of these parameters are very difficult and time consuming. So the author will try to find a much easier simulation method for evaluating the stress-strain relationship of paper materials.

1.3 Outline of the dissertation

The dissertation is organized as follows:

In Chapter 2, some basic knowledge of the mechanical behavior of paper in the out-of-plane direction will be introduced. The equipment and experimental method for measuring the force-deformation behavior will be explained in detail.

In Chapter 3, a new method for measuring the actual contact area will be proposed, with the aid of a microscope, an approach based on image processing technique will be presented to calculate the relationship between force and actual contact area. With the help of this method, the actual modulus and the actual stress-strain relation of paper will be calculated.

In Chapter 4, the relationship between the total and surface deformations will be further discussed through a comparison between different curve fitting methods. For stacks of papers, the theoretical model will be proposed and validated by doing experiments.

In Chapter 5, by establishing the mathematical model for a single sheet, the stress-strain behavior of paper under different compressive forces will be deeply investigated. Based on the stress-strain relation of one sheet, the model for describing the force-deformation behavior of multiple sheets will also be derived.

In Chapter 6, the compressive simulation of paper materials by using gasket elements will be implemented in the FEM software, the accuracy of this new method will be verified by comparing with the experimental results. The compressive simulation of paper under some further selected forces will also be calculated and verified based on the established material model.

The dissertation closes with the conclusions and outlook in Chapter 7.

2 Mechanical behavior of paper in the out-of-plane direction

This dissertation is mainly focused on the mechanical behavior of paper in the out-of-plane direction. This chapter firstly makes an introduction to the experimental setup used for measuring the force-deformation behavior of paper in the out-of-plane direction. After that, some basic knowledge about the typical force-deformation curve (J-shaped curve) of paper materials will be introduced. And then gives an overview of the materials which show J-shaped curves. The J-shaped curve of paper affected by the platform and the heterogeneous density will also be discussed in Sections 2.1.4 and 2.1.5. Finally, the elastic and plastic behavior of paper materials will be presented from different study perspectives.

2.1 Force-deformation curve of paper

In this section, the force-deformation curve of paper will be introduced from different aspects, such as the experimental setup, the applied speed and force in a loading cycle, what's the typical J-shaped curve, which kinds of materials show J-shaped curves, how the force-deformation curve of paper is affected by the platform and heterogeneous density etc., will be introduced in detail.

The paper selected in this dissertation for doing the research is the normal copy paper (copy paper, DIN A4, 210×297 mm, 80 g/m^2), produced by the Steinbeis Paper GmbH in 2013. The actual average thickness is $d_{thickness}$ = 84.7 μm.

The normal copy paper is one of the most representative papers which we can find everywhere, use it every day. If we can do the research by using the normal copy paper, we can also extend the research method to some other papers. So the normal copy paper was selected to prove the usability of the proposed methods.

2.1.1 Experimental setup

All the experiments in this dissertation were performed in the air-conditioned laboratory of the Institute of Printing Science and Technology (IDD). To eliminate the effect of climate conditions of the environment on the mechanical force-deformation behavior, the experimental studies were performed under standardized climatic conditions. The climate is specified in DIN 50014 and prescribed a range of 23 ± 0.5°C for the temperature and a range of 50 ± 1.5% for the relative humidity (Kaulitz, 2009). As an example, the changes of the temperature and relative humidity on 1st of July, 2015 are plotted in Figures 2.1 and 2.2, respectively.

The paper material is sensitive to changes in temperature and humidity. The temperature and relative humidity are maintained within the small range of margin. Even for the same paper stack under same force, small difference of temperature and humidity can make a considerable deviation between different experiments. It can be seen from Figure 2.1 that from 8 am to 20 pm, the change of temperature is around 0.8°C.

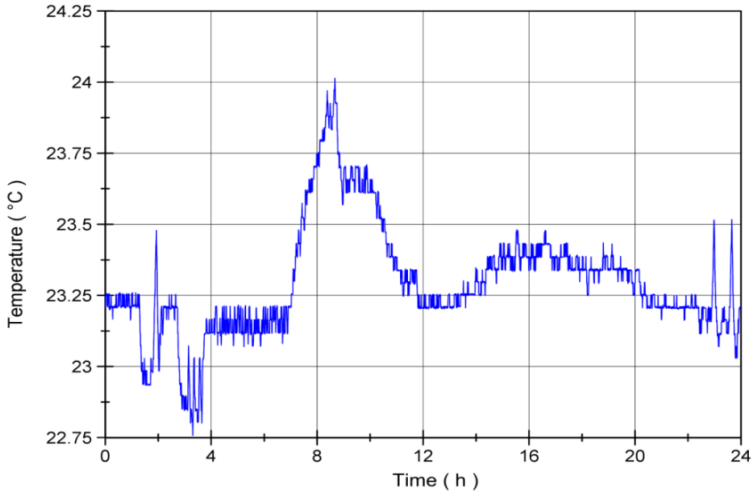

Figure 2.1: Changes of temperature in the air-conditioned laboratory of the IDD on 1st of July, 2015. From 8 am to 20 pm, the temperature changed from 24 °C to around 23.2 °C.

The change of relative humidity mainly happened in the morning (see Figure 2.2), from 8 am to 12 am, the change is around 2.5%.

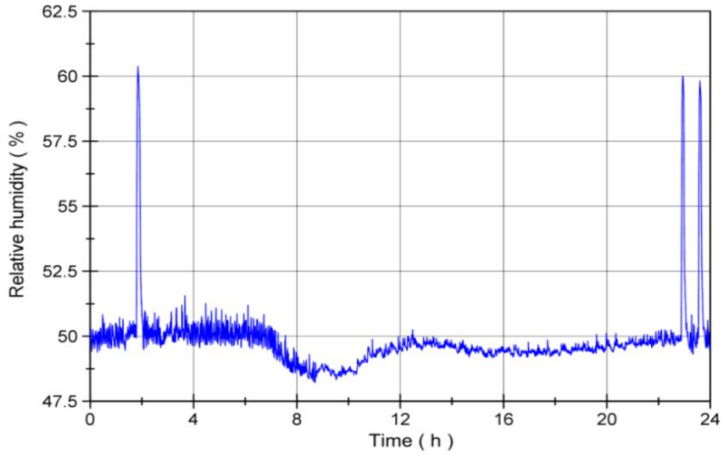

Figure 2.2: Changes of the relative humidity in the air-conditioned laboratory of IDD, which has been recorded on 1st of July, 2015. The changes of the relative humidity mainly happened in the morning from 8 am to 12 am.

Most of the experiments were finished at the time between 14 pm and 20 pm. During this period of time, the changes of temperature and relative humidity are relatively small.

The loading process was finished on ZWICK Z050, which can be utilized for strain, shear and bending tests with different substrates and machine components with high accuracy of the cross head speed (0.0005-2000 mm/min), position repetition accuracy (±2 µm), drive system's travel resolution (27 nm) (Chen et al., 2014a, Desch et al., 2009, Kaulitz, 2009, Kaulitz and Dörsam, 2008). The structure of the compression device in the ZWICK machine is shown in Figure 2.3, which was constructed by Kaulitz (Kaulitz, 2009).

In the device below, the diameter of the cylindrical indenter (pressure head) is 6 mm, the area of the indenter is shown in Figure 2.3. The areal roughness of the indenter and the platform can be measured by using the Sensofar PLu Neox with the objective EPI 10X-N in confocal profiling mode. The areal roughness of the indenter is about 385 nm, the areal roughness of the platform is around 650 nm.

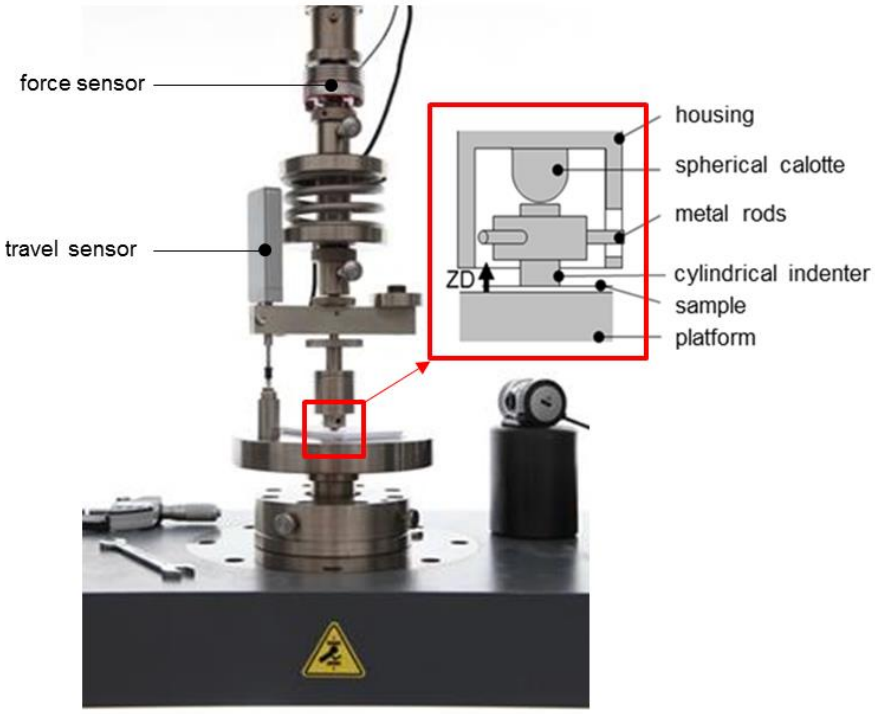

Figure 2.3: Test equipment for obtaining the force-deformation curve of paper constructed by Kaulitz (Kaulitz, 2009) in IDD. The travel sensor (Heidenhain-Metro MT 2581) is produced by Heidenhain firm, with the resolution of 50 nm and the repetition accuracy of 0.2 µm, the diameter of the cylindrical indenter (pressure head) is 6 mm.

Figure 2.4 shows the settings of the loading speed and the corresponding force. At the beginning of the loading condition, the indenter moves down from the original position at the speed of 20 mm/min, until the indenter comes into contact with the surface of the paper. The preload here is set to 1 N. When the change in the amount of force is 1 N, the compression process will begin with a velocity of 0.05 mm/min. Until the force reaches the desired maximum force, the indenter will move up at the speed of 0.05 mm/min. When the force decreases to 1 N, the indenter returns back to the original position at the speed of 20 mm/min.

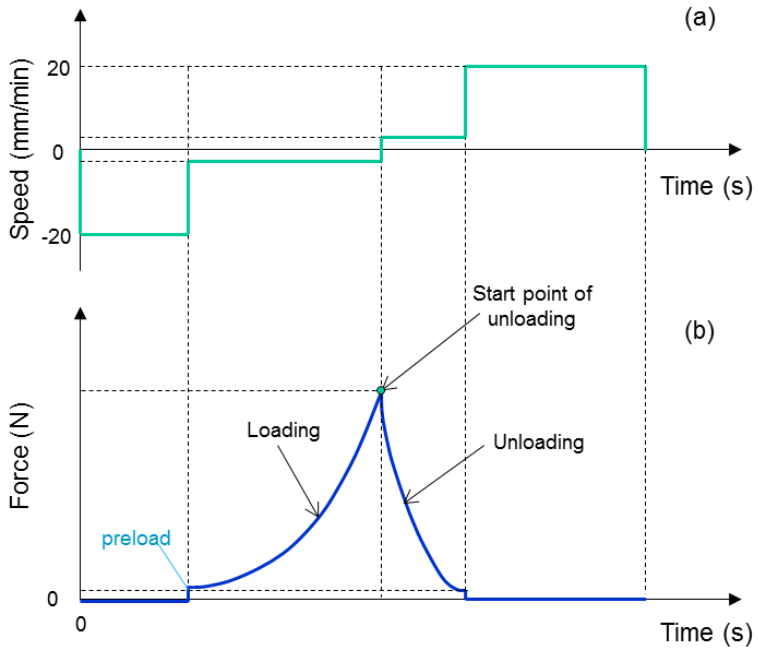

Figure 2.4: Schematic of the applied speed and force in a loading cycle. Two different parts are shown in the above figure, part (a) shows the changes of speed in a complete cycle, negative value means the speed is opposite to ZD direction (see Figure 2.3). Part (b) shows the corresponding forces.

The obtained data of experiments can be used for studying the elasticity and plasticity of paper materials, establishing the descriptive model and comparing its results with the calculation or simulation results, and so on.

2.1.2 Typical J-shaped curve

As you may already know, many engineering materials, such as metals, show Hookean elasticity in which the tensile or compressive stress applied to a sample is directly proportional to the resultant strain. Within the range of Hookean elasticity, the stress-strain curves on loading and unloading are identical. Such linear elasticity is the usual assumption in engineering design.

However, the elasticity of most materials in living systems is much more complicated. Paper material is a very good example of nonlinear materials. The mechanical stress-strain (force-deformation) curve of paper is obviously affected by many factors: the surface roughness, temperature, humidity as well as compression speed, and so on. The mechanical behavior of paper is quite different from other materials.

Based on the experimental setup established above, the compressive force-deformation behavior of paper materials can be obtained easily.

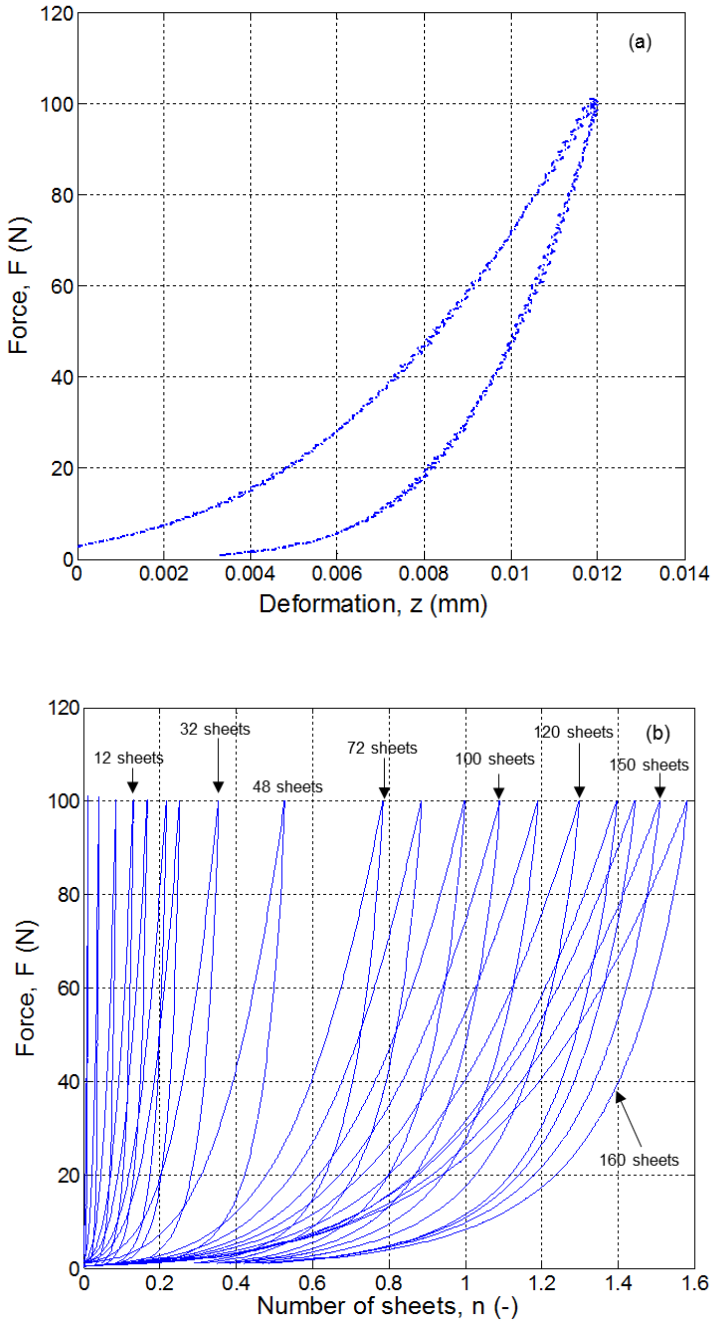

Figure 2.5: Typical force-deformation curves of single sheet and multiple sheets. Two pictures are provided here. Picture (a) shows the typical force-deformation curve of one sheet, the maximum implemented force is 100 N. Picture (b) shows the force-deformation curves of multiple sheets, the number of sheets is between 1 and 160.

It is clear from Figure 2.5 that the mechanical behavior of paper materials under compression is highly nonlinear. Without concerning the influence of the surface topography, the compressive curves of single paper and multiple sheets in the loading stage are typical examples of materials with J-shaped stress-strain curves. These curves show that initially, small increases in stress give large deformations. However, at larger deformations the material

becomes stiffer and more difficult to be compressed. And it also exhibits quite complicated unloading behavior when compression is released. According to the size of the indenter (pressure head) and paper thickness, the force-deformation curve can be easily transferred into a stress-strain curve.

2.1.3 Materials show J-shaped curves

Not only paper materials, but many other materials also exhibit J-shaped type of stress-strain curves, for example: biomaterials, gasket materials, porous materials, polymer materials, and so on. In some cases, the models or the research methods of different materials are interchangeable. Some of the relative literatures about the materials with J-shaped curves are summarized in Table 2.1.

Table 2.1: Materials with J-shaped stress-strain curves and their relative literatures.

Materials	Literature	
Natural biomaterials	· Chirita and Ionescu, 2011 · Gautieri et al., 2011 · Guarino et al., 2012 · Holzapfel, 2001 · Kim and Mooney, 2000	· Liu et al., 2014 · Newberry et al., 2005 · Poolthong, 1998 · Picu, 2011 · Shergold et al., 2006
Gasket materials	· Cartraud and Wielgosz, 1996 · Fukuoka et al., 2007 · Fukuoka et al., 2012 · Fukuoka and Takaki, 2003 · Jorwekar et al., 2006 · Murali Krishna et al., 2007	· Takaki and Fkuoka, 2001 · Takaki and Fukuoka, 2000 · Takaki and Fukuoka, 2002a · Takaki and Fukuoka, 2002b · Takaki and Fukuoka, 2003
Porous materials	· Aboraia et al., 2011 · Alzoubi et al., 2014 · Caliri Júnior et al., 2012 · Croop et al., 2009 · De Vries, 2009 · Du Bois, 2009 · Gurevitch and Silverstein, 2012 · Kolling et al., 2007	· Li and Hu, 2003 · Ramon et al., 1990 · Serifi et al., 2003 · Slik et al., 2006 · Szyniszewski et al., 2014 · Tita and Caliri Júnior, 2012 · Yu and Banhart, 1997
Polymer materials	· Bhat et al., 2011 · Bakarich et al., 2012 · Dong et al., 2013 · Harrass et al., 2013	· Jang et al., 2015 · Kato et al., 2015 · Lamouche et al., 2012 · Liu et al., 2013

	· Hu et al., 2014a · Hu et al., 2014b · Imran et al., 2010	· Neel et al., 2006 · Tronci et al., 2013
Other materials	· Chen et al., 2013 · Chen et al., 2014b	· Katta and Rasmuson, 2008 · Santi et al., 2000

Natural biomaterials

Many biomaterials exhibit J-shaped type of stress-strain curves, for example, ligaments, tendons, blood vessels, skins or articular cartilages, and so on (Holzapfel, 2001). (Chirita and Ionescu, 2011) provided an overview of available tools and several parametric models to characterize the mechanical properties of blood vessels, different descriptive models for J-shaped stress-strain materials were calculated and compared. In (Shergold et al., 2006), the compressive stress-strain responses of pig skin and silicone rubber at low and high strain rates have been measured, a constitutive model was introduced to describe the rubber-like behavior. The research of collagen micrifibrils was divided into different hierarchical levels in (Gautieri et al., 2011). The J-shaped stress-strain curves of wet and dry fibrils were compared in (Liu et al., 2014). Some other biomaterials, such as bone-like composite material (Guarino et al., 2012), tooth (Poolthong, 1998), smooth muscle (SM) tissues (Kim and Mooney, 2000), dry mutton wool (Picu, 2011) or wheat flour doughs (Newberry et al., 2005), which also show typical J-shaped stress-strain curves.

Gasket materials

As mentioned in the first chapter, the stress-strain behavior of gasket materials has been investigated by many researchers (Fukuoka et al., 2007, Fukuoka et al., 2012, Fukuoka and Takaki, 2003, Takaki and Fkuoka, 2001, Takaki and Fukuoka, 2000, Takaki and Fukuoka, 2002a, Takaki and Fukuoka, 2002b, Takaki and Fukuoka, 2003, Jorwekar et al., 2006, Cartraud and Wielgosz, 1996, Murali Krishna et al., 2007), which show that the stress-strain curves of most gasket materials are also J-shaped curves.

Porous materials

Foam materials and cellular materials are typical porous materials. Generally, the stress-strain curves of porous materials show S-shaped (Alzoubi et al., 2014, Caliri Júnior et al., 2012, Slik et al., 2006, Szyniszewski et al., 2014, Tita and Caliri Júnior, 2012, De Vries, 2009, Yu and Banhart, 1997) or J-shaped curve (Ramon et al., 1990, Serifi et al., 2003), some materials show the curves of both of them (Aboraia et al., 2011, Du Bois, 2009, Croop et al., 2009, Gurevitch and Silverstein, 2012, Kolling et al., 2007 , Li and Hu, 2003). For S-shaped stress-strain curve, if a pre-stress is imposed to the materials, the S-shaped stress-strain curve would be changed to J-shaped.

Polymer materials

Many polymer materials used in tissue engineering also show J-shaped stress-strain curves. To show the potential application of the scaffolds in tissue-engineering, novel chitosan-halloysite nanotubes (HNTs) nanocomposite (NC) scaffolds were developed in (Liu et al., 2013). The results of mechanical and thermal properties show that the NC scaffold exhibited significant enhancement in compressive strength, compressive modulus and thermal stability. The chitosan-HNTs NC scaffords exhibited great potential for applications in tissue engineering or as drug/gene carriers. A method of producing low modulus thin film materials with stress-strain responses that can precisely to match the biological tissues was presented (Jang et al., 2015), which provides possible applications that range from soft biomedical devices to constructs for tissue engineering.

Hydrogels are fascinating polymer materials with high water content and low surface friction that can be used for numerous applications (Harrass et al., 2013). It can be seen from many papers that the stress-strain behavior of hydrogels shows typical J-shaped curves. For example: By composing of cross-linked six arm star-shaped poly (sPEDPO) as the primary networks and the polyacrylamide (PAAm) as the secondary network, the presented double-network (DN) hydrogels show a fully reversible J-shaped behavior in repeated loading-unloading experiments (Harrass et al., 2013). A new method was developed (Dong et al., 2013) to fabricate nanocomposite double-network (DN) gels, the test results show that by compositing of carbon nanotubes (CNTs) without organic modification, the gels have excellent mechanical properties. The compressive stress-strain curves for nanocomposite DN hydrogels are typical J-shaped curves. In the works of Hu (Hu et al., 2014a, Hu et al., 2014b), the resulting hydrogels with different salecan composition ratios and preparation temperatures were characterized. In addition, by introducing the hydrophilic salecan, the swelling capability and the mechanical properties of the hydrogels were investigated.

Some other relative researches about the mechanical behavior of polymer materials can also be found (Bhat et al., 2011, Bakarich et al., 2012, Kato et al., 2015, Tronci et al., 2013, Neel et al., 2006, Lamouche et al., 2012, Imran et al., 2010).

Other materials

Katta (Katta and Rasmuson, 2008) observed the mechanical behavior of the spherical crystallization of benzoic acid and found that the stress-strain curves are J-shaped, which are well correlated by an exponential-polynomial equation. The relative real contact area of an aluminium sheet under force was calculated in the presented papers of Chen (Chen et al., 2013, Chen et al., 2014b). By considering the real contact area, the stress-strain behavior of aluminium sheet also shows typical J-shaped curve. In the work of Santi et al., different types of stress-strain curves and the corresponding rock types were summarized. Some rocks such as: sandstone, granite, dolomite, diabase, etc., show plastic-elastic (J-shaped) curves. The

different methods of calculating elastic modulus were also introduced in detail (Santi et al., 2000).

2.1.4 J-shaped curve affected by the platform

Most of the J-shaped materials are very thin (paper, gasket, hydrogels, etc.) and the platform is not ideal stiff which has its own stiffness (the red line shown in Figure 2.6). When the experiments are implemented, the influence from the platform is not considered (the lime curve shown in Figure 2.6). If the hardness of the platform is taken into account, the ideal force-deformation curve of J-shaped curve should be a little different (the green curve shown in Figure 2.6). The force-deformation curve of the copy paper (the green curve in Figure 2.6) was calculated by the deformation of the copy paper with platform (the lime curve in Figure 2.6) minus the deformation of the platform (the red curve in Figure 2.6).

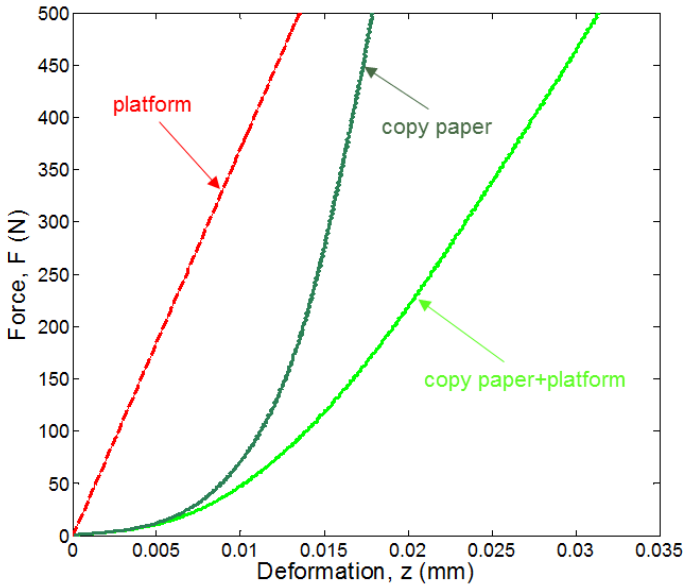

Figure 2.6: Force-deformation curves of paper affected by the platform. Three different curves are provided here: the ideal force-deformation curve of the platform (the red line), the ideal force-deformation curve of copy paper (the green curve) and the actual force-deformation curve of paper (paper together with the platform, the lime curve).

In most of the situations, the influence from the platform can be ignored. But in some special research problems, it should be investigated carefully.

2.1.5 J-shaped curve affected by the heterogeneous density

As shown in Figure 2.7, even for the same sheet, the force-deformation behavior of paper are a little different in different positions because of the different densities generated in the papermaking process.

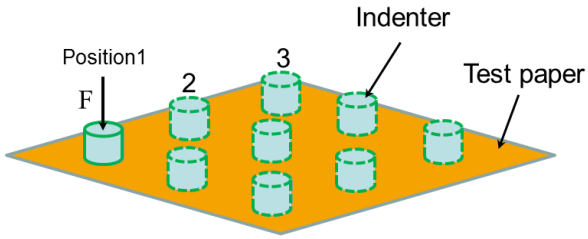

Figure 2.7: Schematic diagram of the different compression positions on paper. In different positions, the density of paper is a little different, which can lead to the differences of the compression curves.

Eight tests were implemented to compare the different force-deformation curves of paper in different positions. The results of seven different tests were plotted in Figure 2.8.

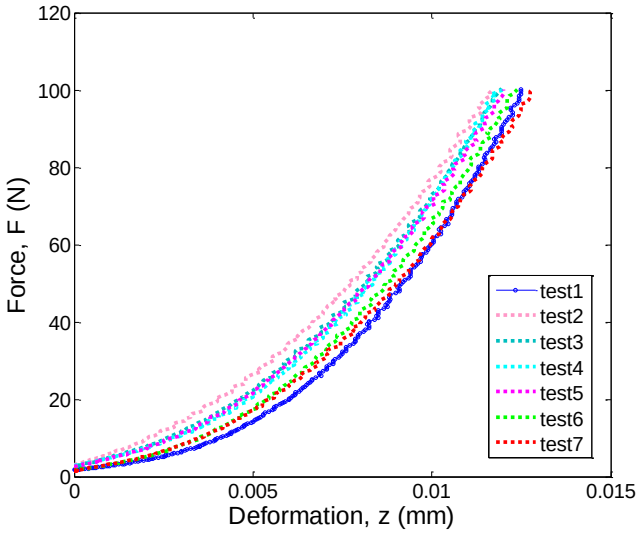

Figure 2.8: Force-deformation curves of paper at different positions. The force-deformation curves of paper in different positions are a little different, which is caused by the heterogeneous density of paper.

It is clear from Figure 2.8 that the force-deformation curves of paper in different positions are a little different. This problem will lead to big deviations, especially, in the experiments when the numbers of sheets are very small. For the experiments of several sheets, the deviations between different tests will be decreased because of the average effect.

2.2 Elastic-plastic behavior of paper

Elasticity and plasticity are the two most common properties of materials. The force-deformation curve of paper material is a J-shaped curve. It's not easy to distinguish the elastic

deformation or the plastic deformation from this kind of curve. In this section, the elastic-plastic behavior of paper and paper stacks will be introduced from different perspectives.

2.2.1 Compressive behavior under different preloads

In the experimental process, the preload is often used in testing a specimen, for a process when the crosshead moves to load the specimen to a specified value before a test starts. The use of preload can improve the accuracy and repeatability of results. For different preloads, the obtained stress-strain curves are also very different. Some experiments under different preloads were implemented, the preloads set in these experiments are: 1 N, 20 N, 40 N, 60 N, 80 N and 100 N.

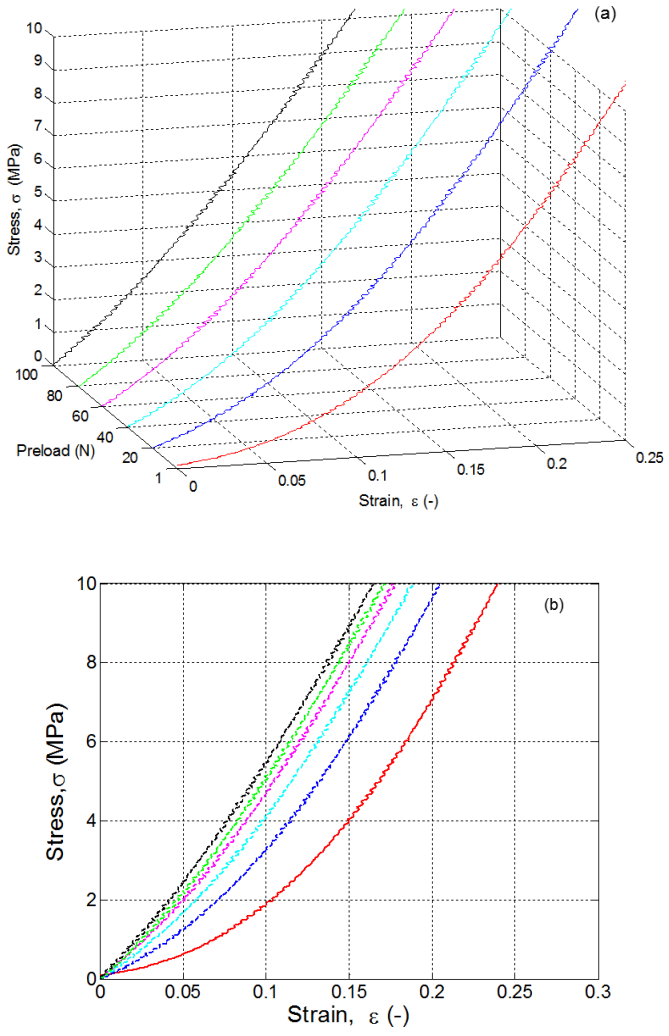

Figure 2.9: Stress-strain curves of paper under different preloads. Two pictures are provided, picture (a) shows the 3D stress-strain curve of paper under different preloads, picture (b) shows the corresponding 2D stress-strain curve. The preloads set in these experiments are: 1 N, 20 N, 40 N, 60 N, 80 N and 100 N. The red curve is the stress-strain curve when the preload is 1 N. The black line is the result when the preload is 100N

Figure 2.9 shows the loading behavior of paper under different preloads. It can be seen that with the increase of the preload, the stress-strain curve of paper (calculated by the nominal contact area) becomes much closer to linear curve. The paper materials show elastic properties under high pressure.

2.2.2 Compressive behavior under cyclic loads

The elasticity and plasticity behavior of paper can be shown much clearer from the stress-strain curve under cyclic loading, which is shown in Figure 2.10. Three cyclic loading processes were implemented, which are drawn with different colors.

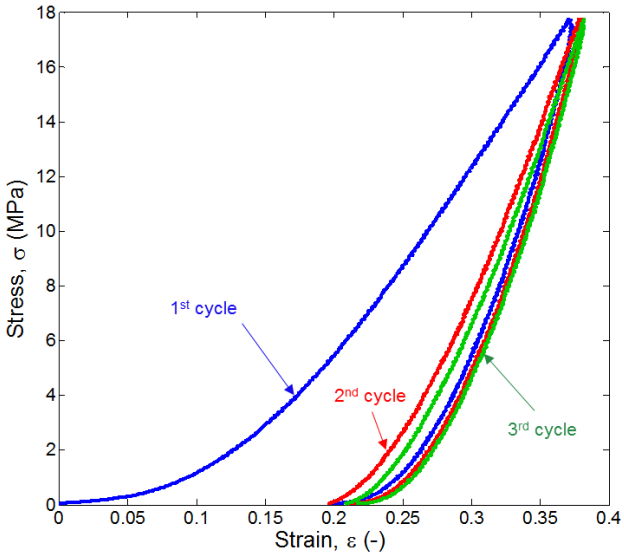

Figure 2.10: Stress-strain curves of paper under three consecutive loading-unloading cycles. After the first loading cycle, the stress-strain curves of paper at the second and third loading cycles are much closer to linear curves.

From the stress-strain curves of paper at the second and third cycles, it is apparent that after the first cycle, the stress-strain curve of paper is much closer to a linear curve. The stress-strain curve is not exactly linear, but the deformation (strain) can recover to the original shape. This behavior is affected by the loading speed, which can also be regarded as viscoelasticity, but anyway, after compression at a certain degree, the paper material can be regarded as an elastic material.

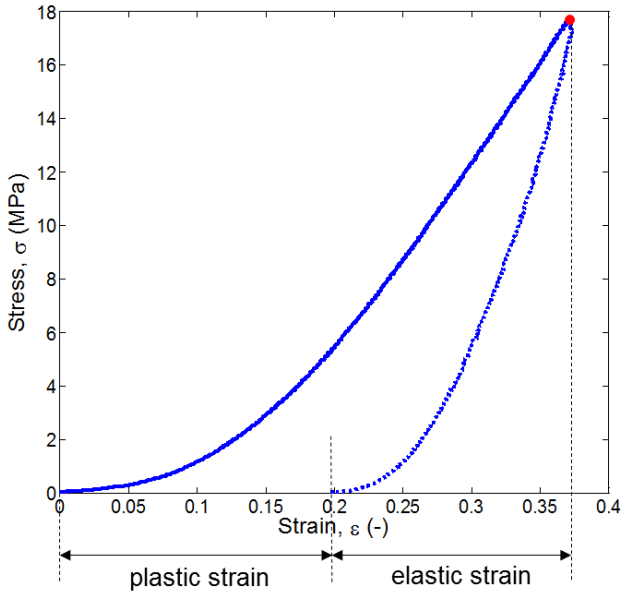

Figure 2.11: Typical stress-strain curves of paper. The strain can be divided into two parts: the elastic strain and the plastic strain.

According to the analysis above, the deformation (or strain) of one sheet can be divided into two parts: plastic deformation (strain) and elastic deformation (strain), as shown in Figure 2.11. The plastic strain (residual strain) normally is a dimensional change that will not disappear when the initiating stress is removed, this kind of deformation is permanent. For the elastic strain, when the stresses are removed, the material always returns back to its original shape, deformation is reversible, there's no permanent deformation occurs.

So, that's the reason why in the case of paper calendaring, the paper plastification caused by the loading in the first roller pair is nearly 40% of the total deformation, which is much bigger than the plastification caused in the subsequent pairs (smaller than 2%) (Eckstein, 2014, Eckstein and Hagedorn, 2014).

2.2.3 Single sheet under different forces

As analysis above, the deformation of one sheet can be divided into elastic deformation and plastic deformation. But when the forces are different, the percentage of the plastic deformation may also be quite different. According to the experimental results, the force-deformation curves of paper under different forces were drawn in Figure 2.12. In the following figure, the maximum forces used in these experiments are: 20 N, 40 N, 80 N and 120 N.

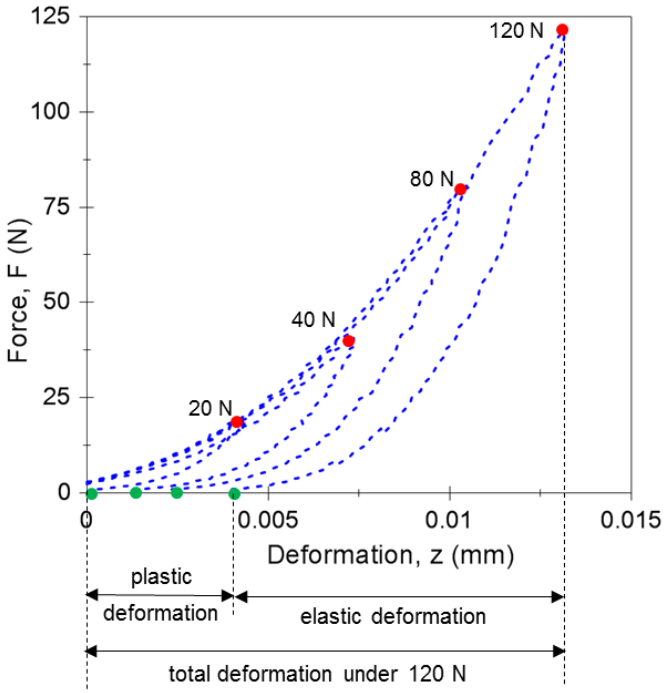

Figure 2.12: Elastic and plastic deformation of a single sheet. The maximum forces used in these experiments are: 20 N, 40 N, 80 N and 120 N. In this figure, these blue curves are the experimental force-deformation curves, the red points show the positions of the biggest deformations and the green points show the plastic (residual) deformations.

It is clear from Figure 2.12 that there's not a great deal of difference between the loading curves, which are coincide with each other. In the unloading stage, different plastic (residual) deformation z_r occurs. The experiments of measuring the force-deformation behavior under some other forces were also implemented. The percentage p of the plastic deformation z_r occupied in the whole deformation z was calculated and listed in Table 2.2.

Table 2.2: Percentages of the plastic deformations calculated according to the experiments of one sheet. In these experiments, the diameter of the indenter is 6 mm, so the contact area can be calculated. The maximum deformation is the deformation at the start point of unloading.

Force F (N)	Pressure P (MPa)	Total deformation z (mm)	Plastic deformation z_r (mm)	Percentage of the plastic deformation p (%)
0	0.00	0.00	0.00	0.00
20	0.71	0.42×10^{-2}	0.02×10^{-2}	4.82
40	1.41	7.15×10^{-3}	1.35×10^{-3}	18.88

60	2.12	8.65×10^{-3}	1.80×10^{-3}	20.81
80	2.83	10.35×10^{-3}	2.30×10^{-3}	22.22
100	3.54	11.9×10^{-3}	3.25×10^{-3}	27.31
120	4.24	12.95×10^{-3}	3.90×10^{-3}	30.12
200	7.07	17.15×10^{-3}	6.40×10^{-3}	37.32
400	14.15	24.55×10^{-3}	10.30×10^{-3}	41.96
600	21.22	33.75×10^{-3}	17.95×10^{-3}	53.19
800	28.29	36.95×10^{-3}	20.70×10^{-3}	56.02

According to the data provided above, the percentage of the plastic strain (deformation) p can be drawn in the following figure (the pink points shown in Figure 2.13). Then the changing of the percentage can be described by using the curve fitting method (the dashed curve shown in Figure 2.13).

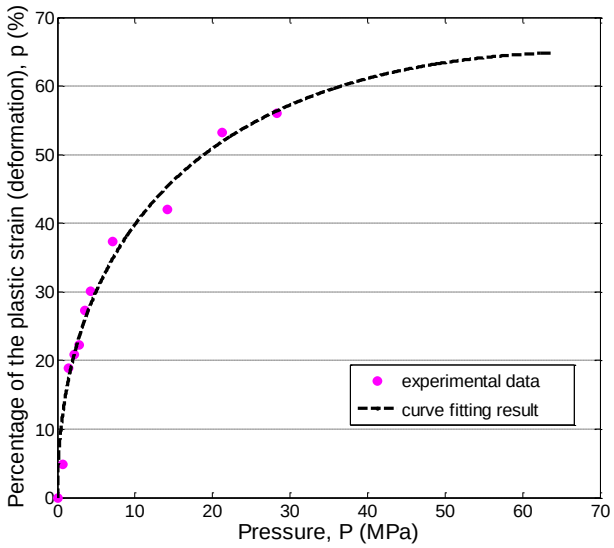

Figure 2.13: Percentage of the plastic deformation of a single sheet occupied in the maximum deformation. The pink points are the experimental results. The black dashed line is the fitting curve, the coefficient of determination: $R^2 = 0.972$.

According to Table 2.2 and Figure 2.13, it can be seen that the percentage of the plastic strain (deformation) is increasing with the enhancement of the pressure, which can be described by using the following fitting equation:

$$p = -0.927 \cdot P + 15.52 \cdot \sqrt{P} \tag{2.1}$$

Where, p is the percentage of the plastic strain (deformation). P is the corresponding pressure applied to the paper. The graph illustrates that, with increase of the pressure, the maximum percentage of the plastic strain (deformation) is approaching to about 65%.

2.2.4 Multiple sheets under a certain maximum force

For multiple sheets, the total deformation can also be divided into elastic deformation and plastic deformation (Schaffrath, 1993, Schaffrath and Göttsching, 1992a).

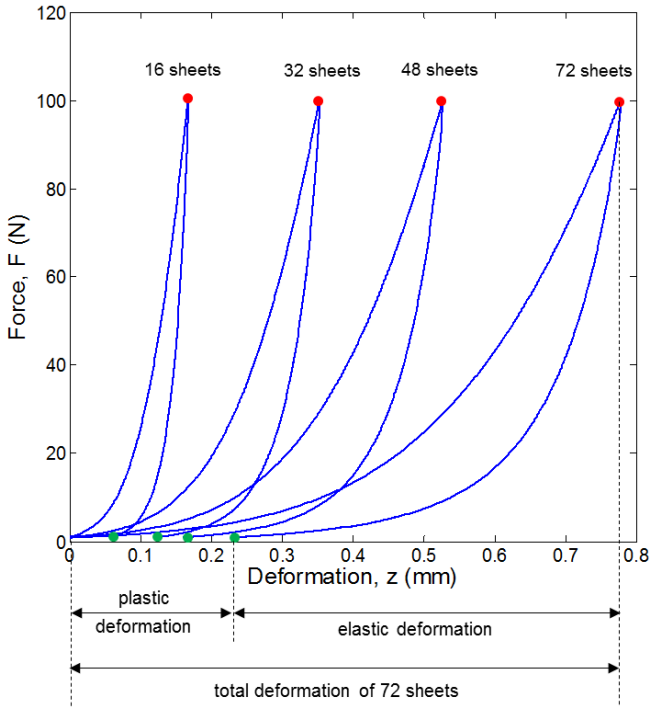

Figure 2.14: Elastic and plastic deformation of multiple sheets. The maximum force used in these experiments is 100 N. These blue curves are the experimental force-deformation curves, the red points show the positions of the biggest deformations, the green points show the plastic (residual) deformations and the sheet numbers are 16, 32, 48 and 72.

As can be seen from Figure 2.14, for 72 sheets, when the maximum force is 100 N, the maximum deformation z is about 0.778 mm, when the force is removed, the plastic (residual) deformation z_r is about 0.227 mm, which is around 29.2% of the maximum deformation z. For other sheets, the percentage of the plastic deformation p can also be calculated according to the experimental results, which are shown in Table 2.3.

Table 2.3: Percentage of the plastic deformation of multiple sheets. The maximum force used in these experiments is 100 N.

Number of sheets n	Total deformation z (mm)	Plastic deformation z_r (mm)	Percentage of the plastic deformation p (%)
1	1.19×10^{-2}	0.33×10^{-2}	27.31
2	1.95×10^{-2}	0.66×10^{-2}	33.85
4	4.06×10^{-2}	1.48×10^{-2}	36.33
8	8.55×10^{-2}	3.18×10^{-2}	37.13
12	13.00×10^{-2}	4.63×10^{-2}	35.60
16	16.66×10^{-2}	5.76×10^{-2}	34.58
20	21.64×10^{-2}	8.06×10^{-2}	37.22
24	25.12×10^{-2}	8.82×10^{-2}	35.10
32	35.23×10^{-2}	12.02×10^{-2}	34.10
48	52.67×10^{-2}	15.91×10^{-2}	30.20
72	77.80×10^{-2}	22.71×10^{-2}	29.18
80	88.40×10^{-2}	30.83×10^{-2}	34.87
100	109.05×10^{-2}	36.99×10^{-2}	33.92
120	129.90×10^{-2}	41.98×10^{-2}	32.31
140	144.42×10^{-2}	46.87×10^{-2}	32.45
160	158.23×10^{-2}	48.12×10^{-2}	30.41

According to the data provided in Table 2.3, the percentages of elastic and plastic strain (deformation) of different sheets were drawn in Figure 2.15. The numbers of sheets are various from 1 to 160.

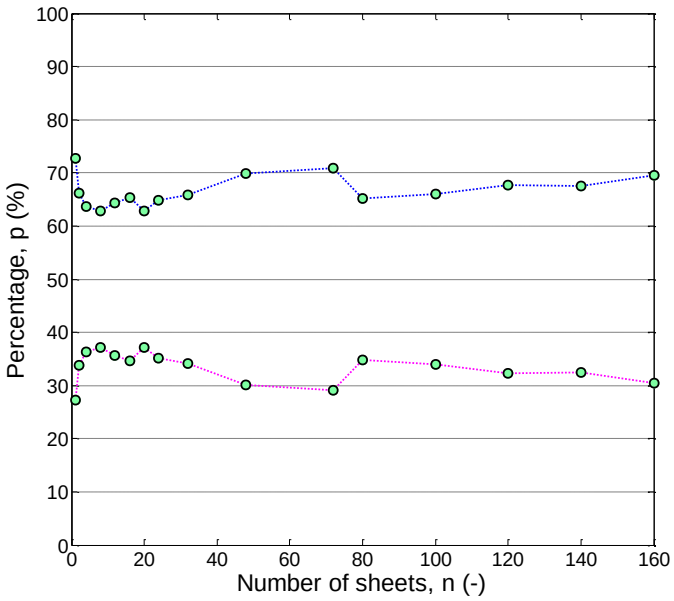

Figure 2.15: Percentage of the elastic and plastic deformation calculated according to the experimental results of multiple sheets. Two curves are provided in this picture, the blue dashed curve shows the percentage of the elastic deformation and the pink dashed curve shows the percentage of the plastic deformation. In these experiments, the maximum force implemented is 100 N. The numbers are various from 1 sheets to 160 sheets.

We can see from Figure 2.15 that, for multiple sheets with a constant maximum force, the percentage of the plastic deformation changes a little with the increasing of the number, which can be regarded as a constant value. For elasticity, which occupied around 66.18%, the percentage of the plasticity is about 33.82%.

2.3 Summary

In this chapter, some basic knowledge about the out-of-plane behavior of paper materials such as its applications and the previous studies on this subject were introduced in detail. The experimental results of the elasticity and plasticity of paper and paper stacks were also analyzed from different standpoints.

But actually, the elastic behavior of paper is much more complicated. The differences between the pure elasticity and the viscoelasticity were ignored in this chapter, which should be discussed in the future studies.

3 Mechanical behavior of paper affected by the actual contact area

In this chapter, Section 3.1 firstly gives a brief introduction about the previous research of the surface roughness. Then, the differences between the nominal and actual contact area will be explained in Section 3.2. Sections 3.3 and 3.4 describe the method of showing the actual contact areas by using carbon paper in detail, in which the concepts of actual contact modulus and the actual stress-strain curve will be proposed. After that, the force sensitivity of different carbon papers will be compared in Section 3.5. A much more precise experimental scheme will be implemented. Section 3.6 discusses the influence of carbon paper on the compressive behavior of copy paper from different perspectives. Finally, this chapter concludes with a discussion of future consideration in Sections 3.7.

Part of the work described in this chapter were published in (Chen et al., 2014a, Chen et al., 2016):

Jian Chen, Jann Neumann, Edgar Dörsam: *Investigation on deformation behavior of paper in Z-direction*. Progress in paper physics seminar, Raleigh, North Carolina, USA; 09/2014

Jian Chen, Edgar Dörsam, Dieter Spiehl, Arash Hakimi Tehrani and Jun Da: *Stress-strain behavior of paper affected by the actual contact area*. Progress in paper physics seminar, Darmstadt, Hessen, Germany; 08/2016

3.1 Studies of surface roughness

Generally, the surface topography is rated by using smoothness or roughness (Pino and Pladellorens, 2009). Roughness plays an important role in determining how a real object will interact with its environment. A roughness value can either be calculated on a profile (line) or on a surface (area). For the profile roughness, the average roughness R_a is the most widely used parameter. For areal roughness parameters, the average areal roughness, S_a, is more common.

The measurement and characterization of surface roughness are very important not only for paper materials but also for metal or other materials. For example, Buchner (Buchner et al., 2009, Buchner, 2008) presented a new method for evaluating the relationship between the real contact area and the normal load, the relative real contact area of an aluminium sheet under force was calculated. In the presented papers of Chen (Chen et al., 2013, Chen et al., 2014b), the effect of surface roughness on the nanoindentation measurements was investigated by

using finite element method, the material AISI 316 L stainless steel was used in the simulation and a 3D model with seven levels of surface roughness was developed to simulate the load-displacement behavior in an indentation process.

For paper materials, the influence of surface roughness on the compressive behavior of different papers was studied by Rättö (Rättö, 2005), who pointed out that when compressing thin sheets, it is important to be aware of the influence of surface roughness. In the model proposed by Schaffrath (Schaffrath and Gottsching, 1991, Schaffrath and Göttsching, 1992b, Schaffrath and Göttsching, 1992a, Schaffrath, 1993), the paper body was described as one internal structure and two rough surfaces, the surface topography was described by using pyramid elements. In addition, the modification of the micro-structure at various scales of the paper surface due to the calendering process was described (Vernhes et al., 2009, Vernhes et al., 2008, Vernhes et al., 2010).

Most other studies about paper surface roughness are still focused on experimental aspects. A large number of techniques are available for characterizing the topographical features of paper surface. Four different methods were evaluated for characterizing the smoothness of the handsheets (Singh, 2008). A fast photometric stereo method was used for the determination of surface topography and reflectance in (Hansson and Johansson, 2000). The paper surface topography under compression was also studied (Teleman et al., 2004). Furthermore, the surface topographical differences between CD and MD directions for newspaper and paperboard were investigated (Alam et al., 2011).

3.2 Differences between the nominal and actual contact areas

According to the metrology definitions, surfaces are classified as three groups: nominal surface, actual (real) surface and measured surface. Nominal surface is the ideal surface defined by the design, in practice this surface does not exist; actual surface is the real physical surface that limits the body; measured surface is the obtained surface by any measurement system.

Normally, the stress-strain relations of most of the materials are calculated by using the nominal contact area. The difference between actual and nominal contact area is ignored, actually, for contact surface, the nominal contact area A_0 and the actual contact area $A(z)$ should be very different, can not be neglected in all situations. The schematic diagram of the difference between nominal and actual contact areas is shown in Figure 3.1.

Generally, when the indenter is very smooth, the actual contact area is much smaller than the nominal contact area because of the paper surface roughness. So, how to show the actual contact area is really a very important topic in the research areas of contact mechanics or surface engineering.

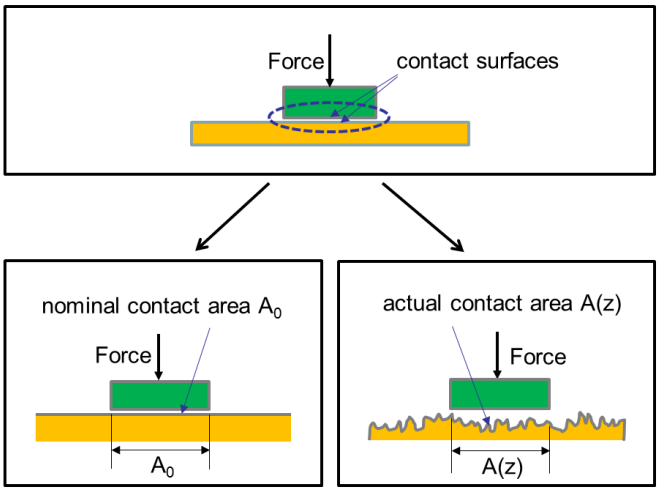

Figure 3.1: Schematic diagram of the difference between nominal and actual contact area.

In this chapter, a new experimental method for evaluating the relationship between the actual contact area and the normal load is proposed. A carbon paper is introduced in this method, and it is assumed that the measured contact areas between carbon paper and copy paper are regarded as the actual contact areas between the indenter and copy paper. Based on this assumption, the mechanical behavior of paper in the out-of-plane direction can be discussed by deducing the actual modulus and calculating the actual stress-strain relation.

3.3 Materials and methods

As mentioned in Section 2.1, the paper selected in this dissertation for doing the research is the normal copy paper, produced by the Steinbeis Paper GmbH.

3.3.1 Experimental setup

The setup of this experiment is shown in Figure 3.2. In order to show the actual contact areas between the indenter and copy paper, a carbon paper (carbon paper, DIN A4, Blue, 29 g/m^2, Geha-1, which is produced by Geha Werke Hannover) was put above the copy paper (copy paper, DIN A4, 80 g/m^2, which is produced by Steinbeis Paper GmbH).

For carbon paper, which has two sides, only one side is the ink side. The ink side should directly contact with the copy paper and then the load was imposed on the other side of carbon paper. When the force was removed, the ink of the carbon paper would be transferred to the surface of copy paper. In the following calculations, the actual contact areas between the indenter and copy paper were replaced by the measured contact areas between carbon paper and copy paper.

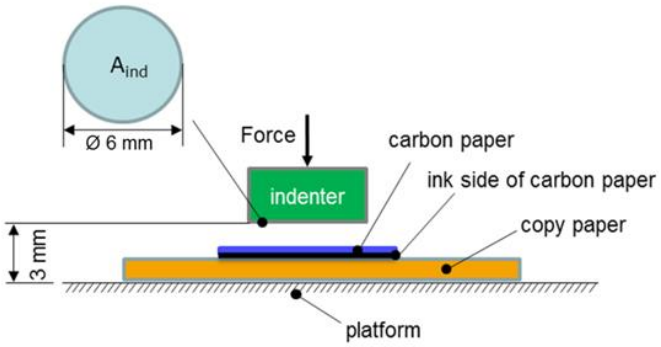

Figure 3.2: Experimental setup used for measuring the actual contact area. The average thickness of the copy paper is about 84.7 µm, the average thickness of the carbon paper (Geha-1) is about 43.6 µm and the diameter of the cylindrical indenter is 6 mm.

The loading process has been introduced in the last chapter. At the beginning of the loading process, the indenter moves down until it comes into contact with the surface of the carbon paper. When the change of force is equal to the preload, the compression process begins. When the force reaches the desired maximum force, the indenter moves up and returns back to the original position.

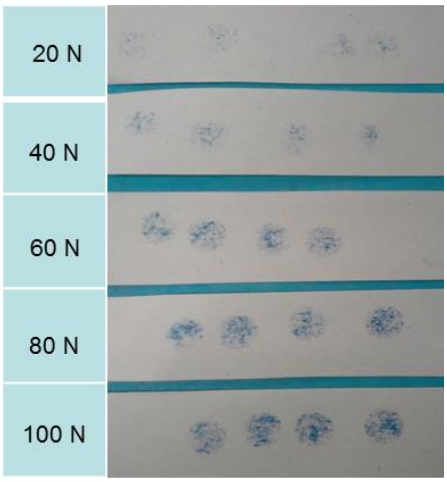

Figure 3.3: Measured contact areas between the carbon paper and copy paper under different forces.

Five groups of experiments were carried out. The applied forces are 20 N, 40 N, 60 N, 80 N and 100 N. The marks of contact areas are shown in Figure 3.3. It is obvious that different forces lead to different contact areas.

3.3.2 Enlarging and transferring the pictures

The image processing technique was used to separate the contact area from the background. The surface of the specimen was magnified 25 times under a binocular microscope and

captured by a camera with pixels of 1600×1200. Then by the aid of MATLAB 8.1 (MATLAB Help, 2013), all pictures were transferred into binary images (see Figure 3.4).

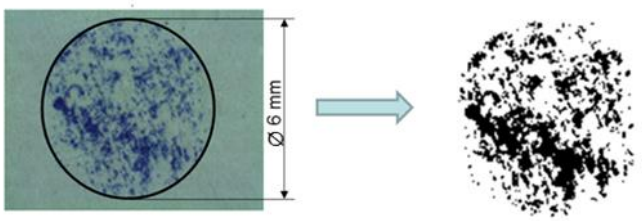

Figure 3.4: Difference between the original and binary pictures. The pixels of these pictures are 1600×1200 (see Appendix A1), the diameter of the indenter is 6 mm.

Binary images are often produced by thresholding a greyscale or color image, in order to separate an object in the image from the background. The color of the object is referred as the foreground color. The rest is referred to as the background color.

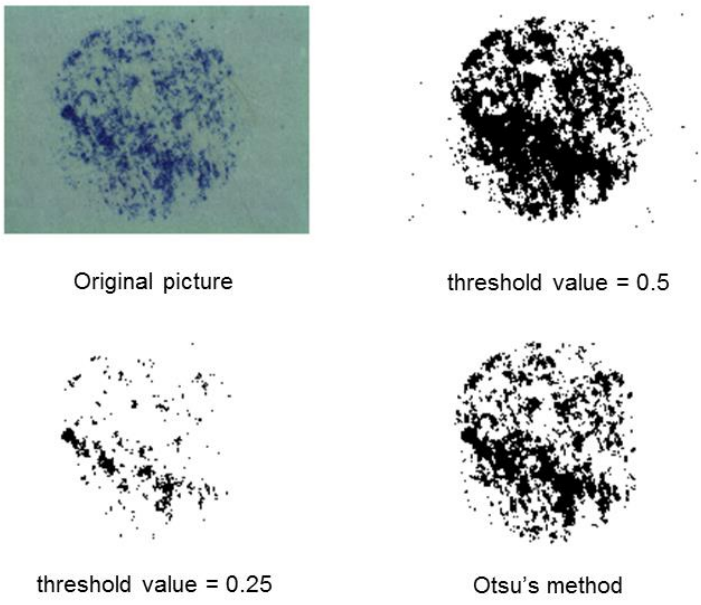

Figure 3.5: Examples of calculating contact areas. The pixels of these pictures are 1600×1200 (see Appendix A2).

MATLAB provides some methods to transfer an original picture to a binary picture. The key problem here is how to determine the threshold value, because the final result is directly determined by this value. Figure 3.5 shows an example of the calculation results by using different threshold values with amounts of 0.5, 0.25 and calculated by the Otsu's method (Otsu, 1979). The three sets of figures are significantly different compared to the original picture, but the result of Otsu's method is the closest result to the original picture.

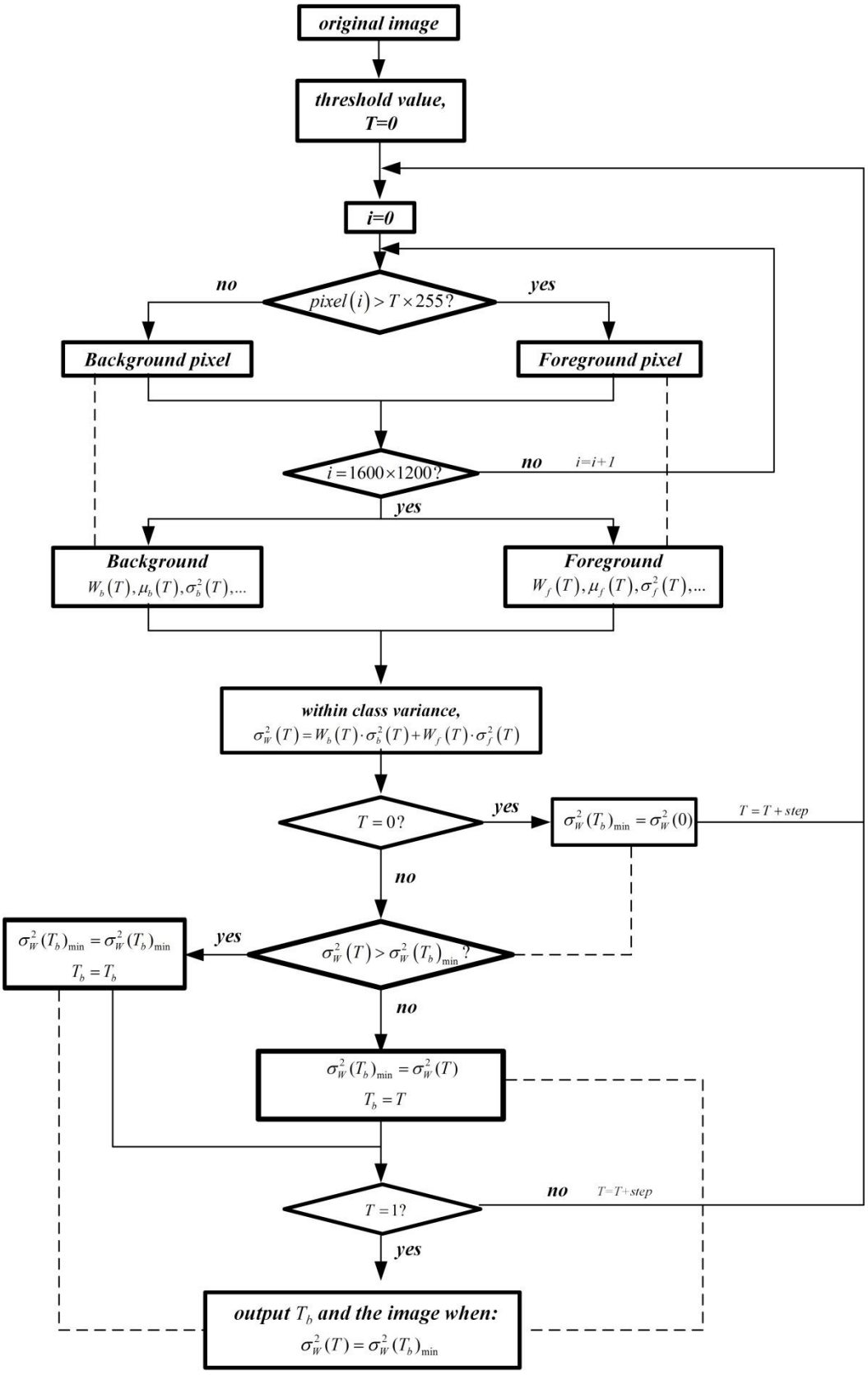

Figure 3.6: Flowchart of the Otsu's method. This method was invented by Nobuyuki Otsu (Otsu, 1979) in the year 1979 and then was widely used in the area of image processing.

Otsu's method, named after its inventor Nobuyuki Otsu (Otsu, 1979), is one of the most popular binarization algorithms. In computer vision and image processing, Otsu's method is used to automatically perform clustering-based image thresholding or reduction of a gray level image to a binary image. As shown in Figure 3.6, for a given threshold value, all pixels of the original image can be divided into two classes of pixels following bi-modal histogram (foreground pixels and background pixels), the whole pixels of the original image here is 1600×1200. After that, calculating the weight ($W_b(T)$, $W_f(T)$), mean ($\mu_b(T)$, $\mu_f(T)$) and variance ($\sigma^2_b(T)$, $\sigma^2_f(T)$) values of the foreground and background, respectively. The next step is to calculate the ''Within-Class Variance'', $\sigma^2_w(T)$. This is simply the sum of the two variances multiplied by their associated weights. It then tries to find the threshold value where the sum of foreground and background spreads is at its minimum (Otsu, 1979). Now, this method has been widely used for transferring an image to a binary picture. A ''graythresh ( )'' command (MATLAB, 2013) is provided in MATLAB for automatically calculating the threshold value of an image by using the Otsu's method.

3.3.3 Calculating the contact area

For different pictures, the Otsu's method will produce different threshold values. The average threshold value was calculated and used to obtain the whole black area. Five groups of experiments (20 N, 40 N, 60 N, 80 N and 100 N) were implemented and in each group, four tests were performed (see Figure 3.7).

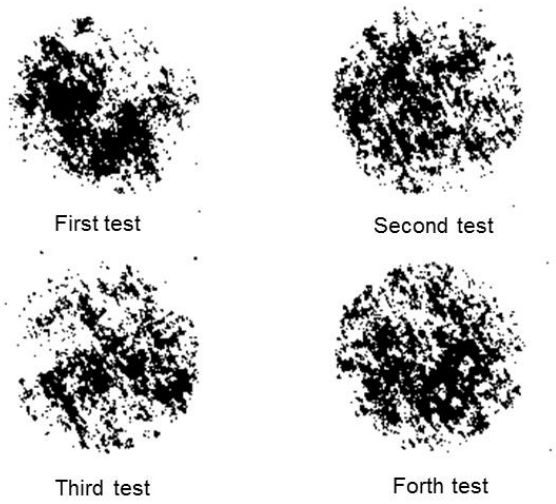

Figure 3.7: Example of contact area calculation for four different tests under 100 N (average threshold value = 0.4514, force = 100 N, the pixels of these pictures are 1600×1200).

The pixels of the binary pictures are 1600×1200, which are the same as the original pictures. The number of the pixels which belongs to the black area can be easily calculated by using the ''bwarea ( )'' command (MATLAB, 2013) in MATLAB. Then, according to the proportional relation between the pixels of black area and the whole area of the original

picture (1600×1200), the value of the black area can be calculated, which is the measured contact area A_{mea}. In this chapter, the measured area A_{mea} is regarded as equivalent to the actual contact area A (z).

3.3.4 Calculating the force-contact area relation

The described experiments were performed under some discrete forces. When the changes of these forces are very small, it is reasonable to assume that the deformation behavior of the material under small forces accord with the theory of elasticity.

Hooke's law is the law of elasticity under small deformation, which states that, for relatively small deformations of an object. The displacement or the size of deformation is directly proportional to the deforming force or load. Hooke's law can also be expressed in terms of stress (σ) and strain (ε). According to Hooke's law:

$$\sigma = E \cdot \varepsilon \;\Leftrightarrow\; F = \frac{E \cdot A_0}{l_0} \cdot z \tag{3.1}$$

Where, A_0 is the nominal contact area, l_0 is the original length or thickness of the material, z is the deformation under the force F. Here, the value of z (or ε) in the out-of-plane direction is regarded as a positive value. For paper structure, the force-deformation relation can be expressed as follows:

$$F(z) = \frac{E(z) \cdot A(z)}{d_{thickness}} \cdot z \tag{3.2}$$

E(z) is the actual modulus, which is changing with the discrete force F(z). A(z) is the actual contact area, which is the discrete area calculated by the experiments above. $d_{thickness}$ is the thickness of copy paper.

The actual modulus of paper under different forces can be expressed as the product of actual contact pressure (W(z)), paper thickness ($d_{thickness}$, which is a constant value, the average thickness is $d_{thickness}$ = 84.7 μm) and the inverse of the total deformation (z).

$$E(z) = \frac{F(z)}{A(z)} \cdot \frac{1}{z} \cdot d_{thickness} = W(z) \cdot \frac{1}{z} \cdot d_{thickness} \tag{3.3}$$

Where:

$$W(z) = \frac{F(z)}{A(z)} \tag{3.4}$$

is the actual contact pressure.

All the variable values can be obtained according to the experiments implemented above. This method can only be used for small deformation under discrete forces. For paper materials, small deformation means when the strain is smaller than 0.2% in the MD/CD direction or the strain is smaller than 20% in the ZD direction (Kaulitz, 2009).

3.4 Calculation results

According to the experiments implemented above, the measured contact areas under different forces were calculated. Five groups of experiments (20 N, 40 N, 60 N, 80 N and 100 N) were implemented. For each of the group, four tests were executed. The results of the measured contact areas are shown in Table 3.1 and Figure 3.8.

Table 3.1: Experimental results of the measured contact areas under different forces. For each group, four tests are executed. The average and standard deviation values are also calculated.

Force (N)	First test (mm^2)	Second test (mm^2)	Third test (mm^2)	Fourth test (mm^2)	Average (mm^2)	Standard deviation (mm^2)
20 N	3.2765	3.5448	3.5448	3.2137	3.3950	0.0031
40 N	5.8110	5.8852	5.5028	4.5209	5.4300	0.0110
60 N	9.6013	10.4746	9.5271	9.0133	9.6541	0.0106
80 N	10.2691	11.5078	9.3787	12.6095	10.9413	0.0248
100 N	10.9085	13.0148	12.6209	13.2089	12.4383	0.0184

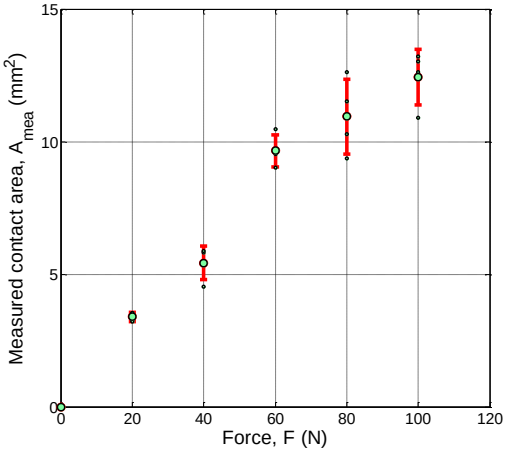

Figure 3.8: Measured contact areas under different forces. The error bar represents the average (mean) value and the standard deviation of measured contact areas under different forces.

Figure 3.8 shows the measured contact areas under 20 N, 40 N, 60 N, 80 N and 100 N. The error bar represents the average (mean) value and the standard deviation of each group. The average value of each group is also plotted in Figure 3.9 as the discrete points. Then the values of measured contact areas under other forces can be calculated by using the quadratic curve fitting method.

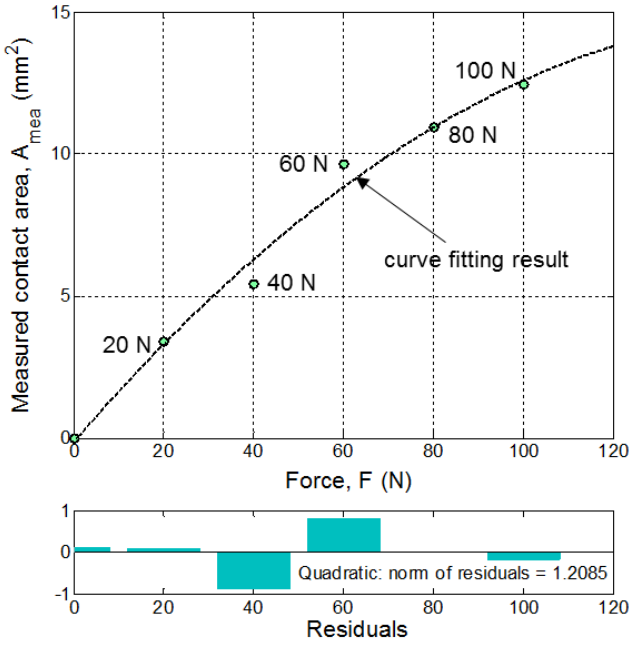

Figure 3.9: Measured contact areas under different forces. The quadratic curve fitting method is used in the first graph. The second graph shows the corresponding residuals. The coefficient of determination: $R^2 = 0.988$.

In Figure 3.9, the dashed black line is the quadratic fitting curve of these discrete values. The fitting function is provided as Equation 3.5.

$$A_{mea} = 5.56\times10^{-4}\cdot F^2 + 0.183\cdot F - 0.127 \tag{3.5}$$

As shown in Figure 3.9, the norm of residuals is equal to 1.2085, the coefficient of determination: $R^2 = 0.988$. The calculation results show that this method can be well used to calculate the measured (actual) contact area A_{mea} (A(z)) under different forces F(z), as well as the relationship between force and actual contact area.

According to Equations 3.3, 3.4 and the calculation results obtained in Figure 3.9, the values of the actual modulus E(z) and actual pressure W(z) can be calculated. The values are listed in the following table.

Table 3.2: Experimental and calculation results of the parameters (→ 0 means near to 0).

F (z) (N)	0	20	40	60	80	100
z (µm)	0	3.66	5.68	7.26	8.62	9.78
A (z) (mm^2)	→ 0	3.40	5.43	9.65	10.94	12.44
W (z) ($N \cdot mm^{-2}$)	0	5.89	7.37	6.22	7.31	8.04
E (z) (MPa)	0	136.30	109.90	72.57	71.83	69.63

In Table 3.2, some discrete contact pressure values under different forces were obtained. The values of force F(z) and the deformation z were directly obtained by the Zwick machine. The values of the actual contact area A(z) and the actual contact pressure W(z) were obtained by the new experiment method and Equation 3.4. E(z) was calculated according to Equation 3.3. With the method of curve fitting, the relationship between actual contact pressure and deformation was calculated and shown in Figure 3.10.

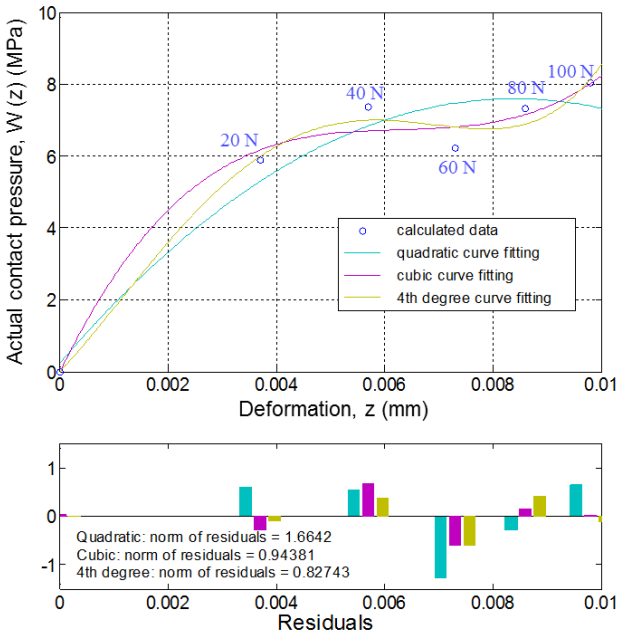

Figure 3.10: Relationship between the actual contact pressure and the deformation. The discrete points are the values of W(z) provided in Table 3.2. Three different curve fitting methods are used here. The picture below shows the corresponding residuals.

Figure 3.10 shows the relationship between the actual contact pressure W(z) and the deformation z. Three different curve fitting methods were used there. The functions of which are provided in Equation 3.6.

$$\begin{cases} quadratic\ curve\ fitting: W(z) = -0.105 \cdot z^2 + 1.76 \cdot z + 0.243 \\ cubic\ curve\ fitting: W(z) = 0.0265 \cdot z^3 - 0.499 \cdot z^2 + 3.16 \cdot z - 0.029 \\ 4^{th}\ degree\ curve\ fitting: W(z) = 5.22 \cdot 10^{-3} \cdot z^4 - 0.0829 \cdot z^3 + 0.227 \cdot z^2 + 1.66 \cdot z - 6.41 \cdot 10^{-3} \end{cases} \quad (3.6)$$

Comparisons of corresponding residuals between different curve fitting methods are shown in the second part of the figure, which are used to see whether the lines are good fit with the discrete data, both of the quadratic (the coefficient of determination: R^2 = 0.936), cubic (the coefficient of determination: R^2 = 0.980) and 4th degree (the coefficient of determination: R^2 = 0.985) curve fitting methods can be used for describing the trend of the calculated data. The residual values of cubic and 4th degree curve fitting are much smaller than the quadratic curve fitting. From the view of physical properties, no matter by using which kinds of curve fitting methods, the stress-strain curve of paper with considering the surface roughness is very similar to the general elastic-plastic materials (Brinson, 2008). In this section, cubic curve fitting method was chosen for describing the actual stress-strain curve.

When the force is changed from 0 N to 20 N, the deformation of the paper is nearly 4 µm, when the force is changed from 20 N to 100 N, the deformation of the paper is only 6 µm. At the beginning of contact, the compressive behavior of paper is obviously affected by the surface structure. When the thickness of paper is very thin, the influence of surface roughness on the compressive response is very important and cannot be neglected.

Paper is not an elastic material. The actual modulus of a non-linear material is not a constant value, which cannot be simply described by using the E-modulus (Mark et al., 2001). According to Equation 3.3 and Table 3.2, the actual modulus E(z) of paper under different deformation z (or strain, ε) can be calculated by using the quadratic curve fitting method (Equation 3.7). The numerical trend can be described.

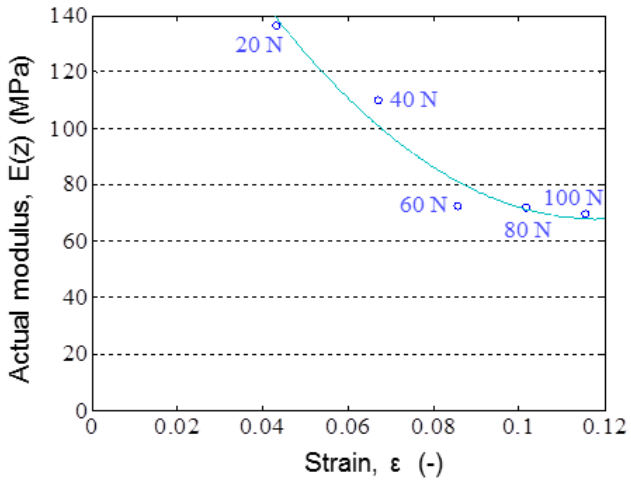

Figure 3.11: Actual modulus of paper calculated by the actual contact area. The discrete data are calculated according to Equation 3.3 and Table 3.2. The blue curve is the corresponding curve fitting result, the coefficient of determination: R^2 = 0.954.

Figure 3.11 shows the relationship between the actual modulus and the strain. The blue curve is the corresponding curve fitting result (see Equation 3.7), the coefficient of determination: $R^2 = 0.954$. When the force is changed from 20 N to 100 N, the actual modulus of paper will decrease from 136.3 MPa to around 70 MPa.

$$\begin{cases} E(z) = 1.77\times10^{6}\cdot z^{2} - 3.53\times10^{4}\cdot z + 244.6 \\ z = 0.0847\varepsilon \end{cases} \tag{3.7}$$

Generally, the behavior of paper in the in-plane direction can be regarded as the elastic-plastic behavior (Xia et al., 2002). The modulus of wood materials is considered range from about 10 MPa to 25 GPa (Drexler, 2009). Unfortunately, only very few researches discussed the modulus of paper in the out-of-plane direction. The modulus of paper in the in-plane direction is much bigger than the modulus in the out-of-plane direction. For example, the E-modulus of a single paperboard provided by Xia (Xia et al., 2002) in the MD direction is about 5.6 GPa, in the CD direction is about 2.0 GPa, the initial modulus in the ZD direction is 18 MPa. The initial E-modulus of another single paperboard in the out-of-plane was measured by Stenberg (Stenberg, 2003), this value is 34 MPa and the E-modulus of this paperboard for fully compacted is about 5 GPa.

Based on the above findings, it can be seen that the calculation result of the actual modulus is reasonable. During the compression process, the actual modulus of paper decreases with increasing deformation (strain). While the contact area approaches to the maximum contact area (approximately equal to the nominal contact area A_0), the actual modulus will be decreased to a constant value.

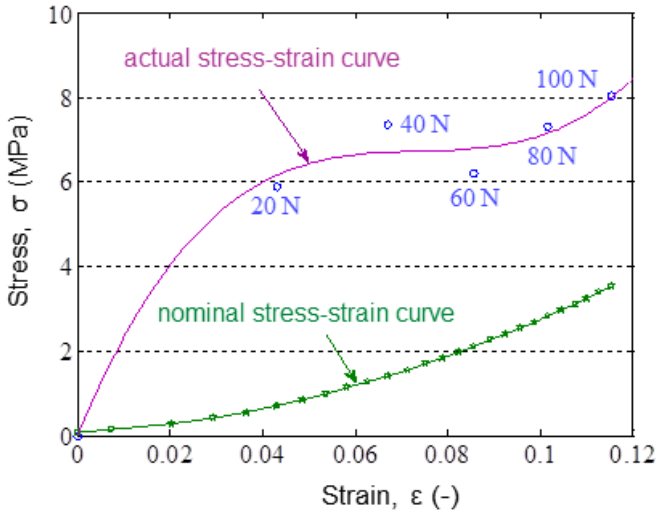

Figure 3.12: Compressive stress-strain curves of paper. The red curve is the stress-strain curve of paper calculated by using the actual contact area, the green curve is calculated by using the nominal contact area.

Figure 3.12 unfolds a clear comparison between the stress-strain curves of paper calculated by different methods. The compressive behavior of paper under actual contact area is obviously different from the result calculated by using the nominal contact area.

According to the actual stress-strain curve calculated by the curve fitting method, at the beginning of the loading process, the stiffness of paper increases with the enhancement of the load. The relationship between stress and strain is nearly linear, especially when the force is smaller than 20 N, but after that the stiffness decreases with increasing of the load, which is very similar to other elastic-plastic materials (Brinson, 2008). For the nominal stress-strain curve, the loading process shows a typical J-shaped curve. So, the calculation method of the contact area plays a very important role in the results of the stress-strain curve.

To sum up, based on the results above, especially, the comparisons between the actual stress-strain curve and the nominal stress-strain curve, we can reasonably infer that the surface topography has a very big influence on the compressive behavior of paper materials.

3.5 Force sensitivity of the carbon paper

As mentioned before, the carbon paper that used for experiments is Geha-1. When the applied force is smaller than 20 N, this type of carbon paper is not sensitive enough to show the contact area. Figure 3.13 shows the force sensitivity of carbon paper (Geha-1). It can be seen that the contact area is not clear anymore when the force is smaller than 20 N. To improve the accuracy of the calculation results, some other tests should be implemented. It is better to find a much more sensitive material, to show the actual contact areas.

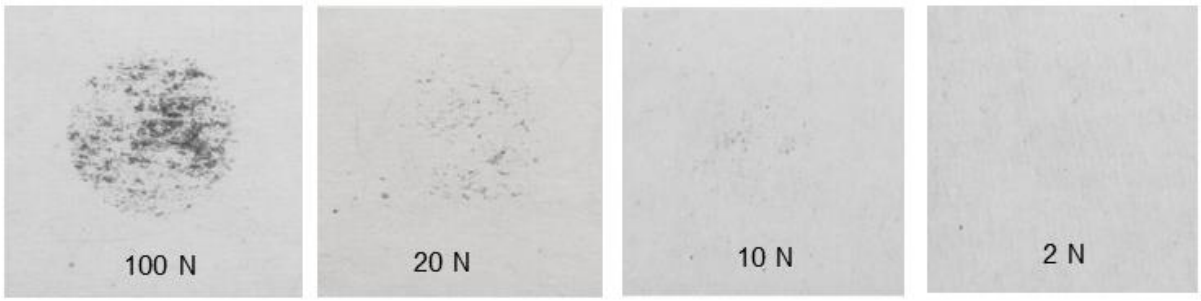

Figure 3.13: Sensitivity tests of carbon paper (Geha-1). Four different forces are imposed on the surface of carbon paper. We can see that when the force is smaller than 20 N, the carbon paper cannot show the contact area clearly.

The material which used here to show the contact area is carbon paper. Some other materials such as Fuji-pressure measuring film (Fujifilm) can also be used to show the actual contact areas (Bachus et al., 2006, Endres, 2006). The pressure measuring films of Fujifilm have different types (Fujifilm, 2016), which are shown in Table 3.3.

Table 3.3: Types of prescale films. Six types of pressure films are available for a wide range of pressures (Fujifilm, 2016). In the table below, W means two-sheet, this type of film is composed of an A-Film, which is coated with a micro-encapsulated color-forming material, and a C-Film, which is coated with a color-developing material. The A-Film and C-Film must be positioned with the coated sides facing each other. S means Single-sheet, the color-developing material is coated on a polyester base, with the micro-encapsulated color-forming material layered on top.

Film type	Pressure range (MPa)
Ultra super low pressure (LLLW)	0.2-0.6
Super low pressure (LLW)	0.5-2.5
Low pressure (LW)	2.5-10
Medium pressure (MW)	10-50
Medium pressure (MS)	10-50
High pressure (HS)	50-130

Fujifilms can be used for measuring the distribution of pressure (Luong, 2000), but in this dissertation, Fujifilms are used to determine the force sensitivities of carbon papers. They are not selected for measuring the distribution of pressure on copy papers, which main because of the following two reasons:

Firstly, the Fujifilms which can be used for measuring the low pressure are W types, which means two films (A-Film and C-Film) should be used at the same time. The maximum force used here is 100 N, the contact area is around 28.27 mm^2, the ideal contact pressure is around 3.54 MPa. When the force is very small, for example 2 N, the pressure is only about 0.07 MPa. To keep the uniformity and correctness of the results, we cannot use three different types of films in the same test.

Secondly, compared with the thickness of copy paper and the surface roughness of the A-Film and C-Film, these kinds of films are not suitable to be used for the experiments here. The measuring results are not accurate.

But Fujifilm can be used for comparing with the carbon paper, and determining the force sensitivities of different carbon papers. The force sensitivities of various carbon papers are very different. In this part, to make the experiments much more precise, the force sensitivity of the carbon papers will be discussed. Seven other different types of carbon papers (SH-1, SH-2, SH-3, DL-1, DL-2, DL-3, Geha-2) from three different companies were selected. Two types of Fujifilm (Fuji-LLW and Fuji-LLLW) were also tested here. SH carbon papers (SH-1, SH-2 and SH-3) are produced by Shanghai Huideli Co., Ltd. DL carbon papers (DL-1, DL-2

and DL-3) are produced by Deli Group Co., Ltd. And Geha carbon papers (Geha-1 and Geha-2) are produced by Geha Werke Hannover. For each of the carbon papers, four different forces (2 N, 10 N, 20 N and 100 N) were imposed on the materials. The effects of the ink on the copy paper are shown in Table 3.4.

It can be seen from Table 3.4 that the sensitivities of different carbon papers are quite different, only SH-1, Geha-2 and Fuji-LLLW can be used for measuring low pressure. The sensitivity of SH-1 is very close to the sensitivity of Fuji-LLLW. When the force is smaller than 10 N, the contact areas can also be shown on the copy paper. The SH-1 carbon paper was selected in the following part for showing the contact areas under different forces.

Table 3.4: Sensitivity tests of different carbon papers and Fujifilms. Seven different carbon papers and two different Fujifilms are tested here. SH carbon papers are produced by Shanghai Huideli Co., Ltd. DL carbon papers are produced by Deli Group Co., Ltd. Geha carbon papers are produced by Geha Werke Hannover.

Carbon papers and Fujifilms	100 N	20 N	10 N	2 N
SH-1	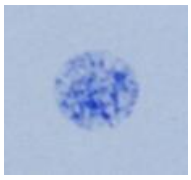	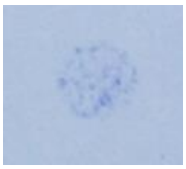		
SH-2	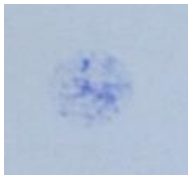			
SH-3				
DL-1	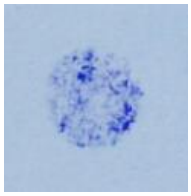			

DL-2	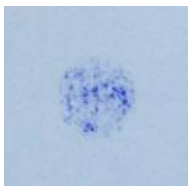			
DL-3	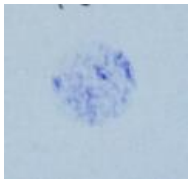			
Geha-2	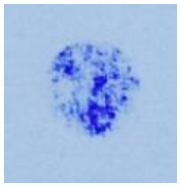			
Fuji-LLW				
Fuji-LLLW				

According to the results obtained above, the SH-1 carbon paper was selected for measuring the actual contact areas. The experimental process in the previous section (Section 3.3.1) was reorganized: the force is changed from 0 N to 100 N, with the length of the substep 2 N, which means 50 groups of experiments (2 N, 4 N, 6 N, 8 N,…, 96 N, 98 N, 100 N) were implemented, for each group, 20 tests were finished. An example of contact area measurement is shown in Figure 3.14.

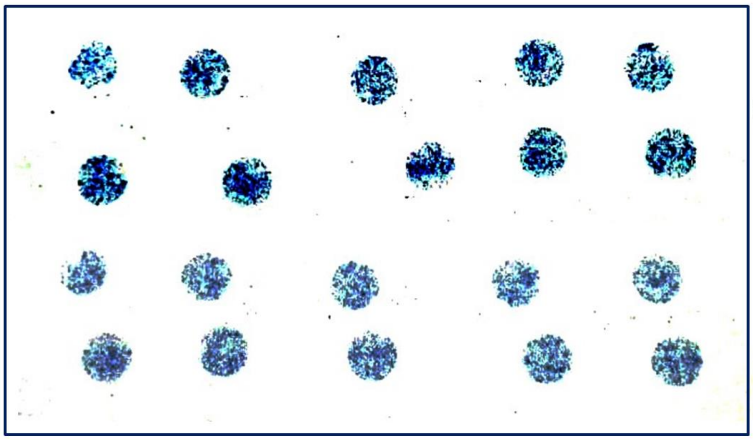

Figure 3.14: Example of measured contact areas (the force here is 90 N). For this group, 20 tests are implemented. The average value of these contact areas is calculated and it is considered as the actual contact area when the force is 90 N.

Then the same method in Section 3.3 was used. The image processing technique was also used to separate the contact area from the background. The surface of the specimen was magnified under a binocular microscope and captured by a camera. The pictures were transferred into the binary images, and then the contact areas can be calculated. The calculated results are shown in Figure 3.15.

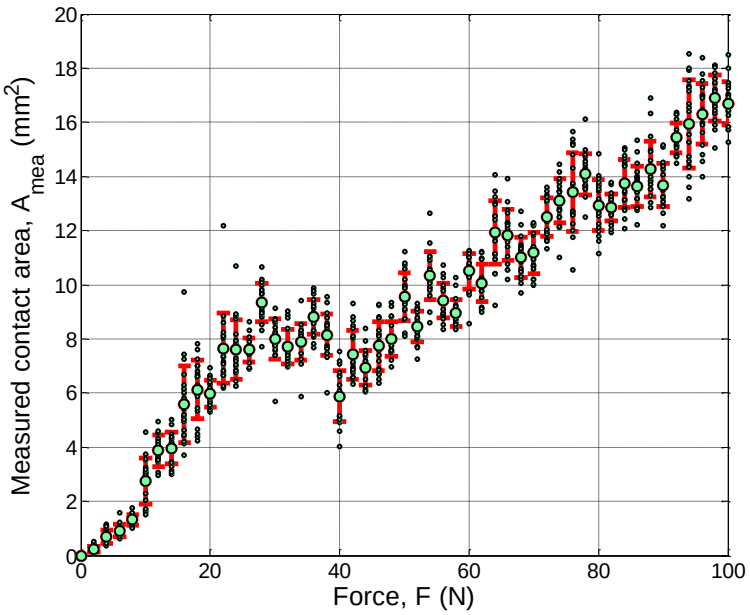

Figure 3.15: Measured contact areas under forces between 0 N and 100 N. The error bar represents the average (mean) value and the standard deviation of measured contact areas under different forces.

Figure 3.15 shows the measured contact areas, the forces were changed from 0 N to 100 N with the substep of 2 N. The error bars represent the average (mean) values and the standard deviations of measured contact areas under different forces.

The average values of the measured contact areas under different forces are plotted in Figure 3.16 as discrete points. The relationship between the measured contact area A_{mea} and force F can be drawn by the curve fitting method. The cubic curve fitting method was used here, the fitting function is provided as follows:

$$A_{mea} = 3.6\times10^{-5}\cdot F^3 - 5.7\times10^{-3}\cdot F^2 + 0.39\cdot F - 0.24 \tag{3.8}$$

The calculation result (the coefficient of determination: $R^2 = 0.953$) shows that this method can be well used to calculate the measured (actual) contact area A_{mea} (A(z)) under different forces F(z).

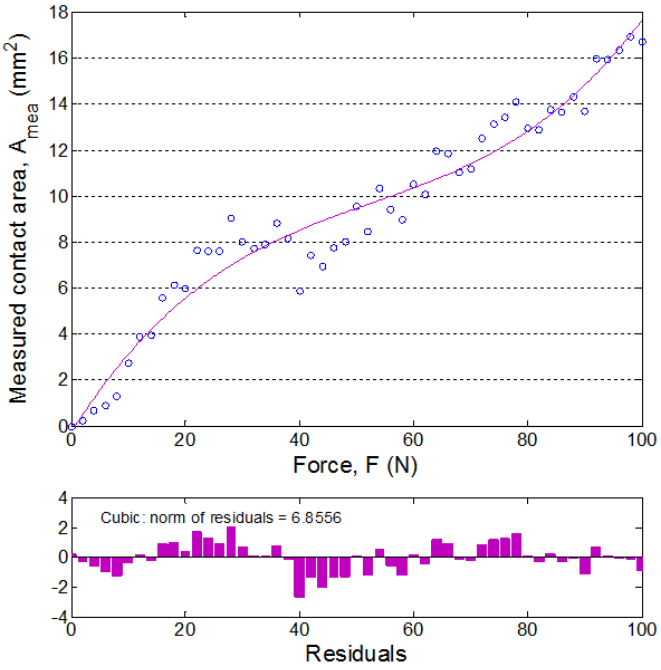

Figure 3.16: Measured contact areas under different forces. The cubic curve fitting method is used in the above picture, the picture below shows the corresponding residuals, the coefficient of determination: $R^2 = 0.953$. The forces are changed from 0 N to 100 N with the substep of 2 N. Each point represents the average contact area of 20 tests under same force.

By using this new method, we can redraw the actual modulus–strain curve (see Figure 3.17) and the actual stress-strain curve (see Figure 3.18).

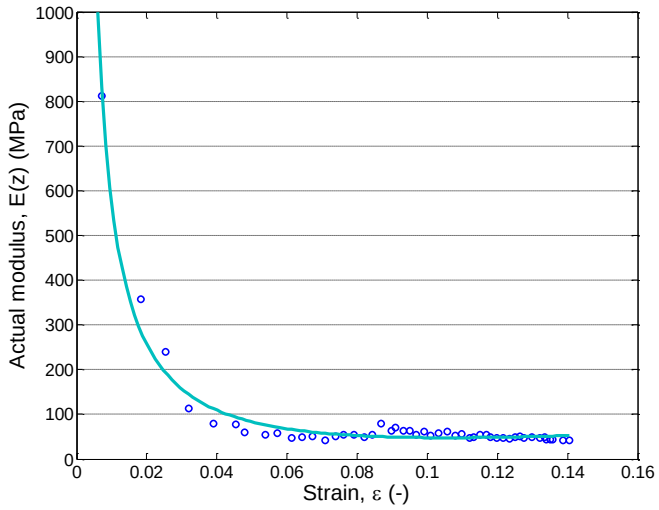

Figure 3.17: Relationship between the actual modulus and strain. The discrete data are calculated according to Equation 3.3. The blue curve is the corresponding curve fitting result, the coefficient of determination: $R^2 = 0.977$.

Figure 3.17 shows the relationship between the actual modulus and the strain (or deformation). The discrete data are calculated according to Equation 3.3. The blue curve is the corresponding curve fitting result (Equation 3.9), the coefficient of determination: $R^2 = 0.977$.

$$\begin{cases} E(z) = -72.73 + 6730.15 \cdot z + 0.54 \cdot \dfrac{1}{z} \\ z = 0.0847 \cdot \varepsilon \end{cases} \tag{3.9}$$

The actual modulus here can also be called as apparent modulus, or the dynamic modulus, which is calculated by using the measured contact areas. The actual modulus is not the true modulus under the ideal situation.

According to Figure 3.17, when the force is changed from 2 N to 100 N, the actual modulus of paper will decrease from 812 MPa to around 50 MPa. As mentioned before, at the beginning of the compression process, the actual modulus of paper is very big which is mainly because the actual contact area is very small. When the contact area approaches to the maximum contact area, the actual modulus will be decreased to a constant value.

According to Equations 3.4 and 3.8, the actual stress-strain curve of paper can also be recalculated. The new actual stress-strain curve is shown in Figure 3.18.

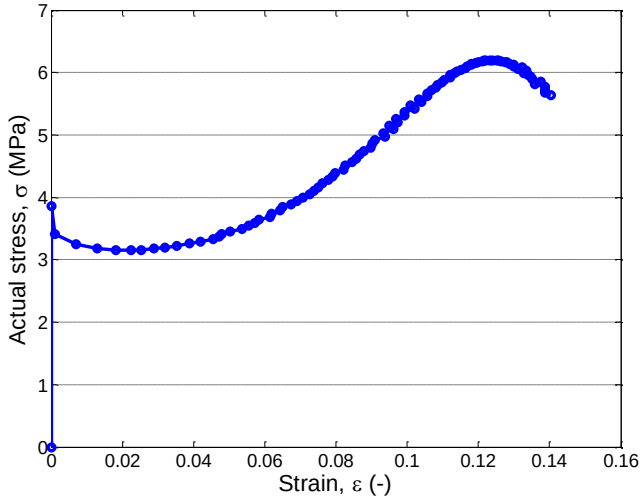

Figure 3.18: Compressive stress-strain curve of paper calculated by using the actual contact area. It shows that if the surface roughness of paper materials is taken into account, the paper materials will be very typical elastic-plastic materials. Here, the stress-strain curve is very similar to other engineering materials such as steel.

From Figure 3.18, we can see that by considering the surface roughness, the stress-strain curve of paper material is a typical elastic-plastic material, which is very similar to other engineering materials, such as steel. Some typical characteristics used for determining the elastic-plastic material, for example, elastic part, plastic part, the yield stress, ultimate stress, etc., all of these behaviors can be found easily in this curve.

On the other hand, for the compression behavior of paper material, the stress-strain curve after ultimate stress is decreasing, rather than increasing, which may be caused by the change of the internal structure or the selected curve fitting function in Figure 3.16.

3.6 Discussion

In the experiments above, a carbon paper was put above the copy paper. The influence of carbon paper on the compressive behavior of normal copy paper should be further discussed.

3.6.1 Analysis of the surface structure

Some experiments for the investigation of the surface roughness of copy paper and carbon paper were finished in the Institute of Printing Science and Technology (IDD) by using the Sensofar PLu Neox, which is a profilometer that combines confocal microscopy, white-light interferometry, phase-shift interferometry and atomic force microscopy in a very unique way. The profilometer is equipped with a controlled displaceable vacuum table capturing samples

with the maximum size of 30×30 cm. The measured topography of copy paper and carbon paper were shown in Figure 3.19. Both of the scan areas are 1274×955 µm.

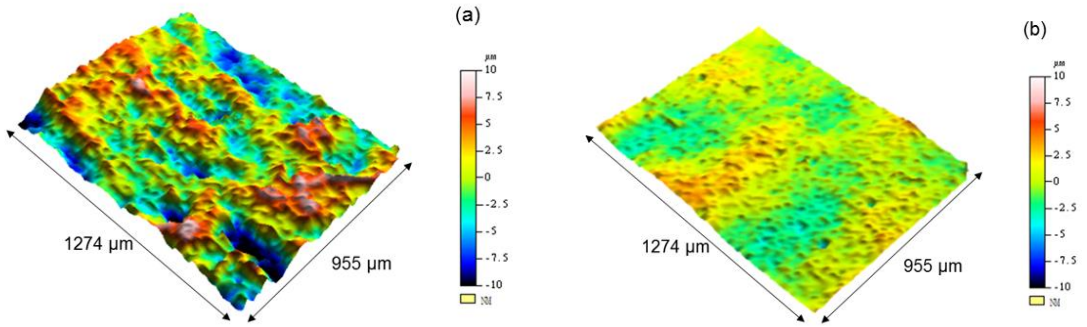

Figure 3.19: 3D Surface topographies of copy paper (a) and carbon paper (Geha-1) (b). The scan area is 1274×955 µm, the range of the color bar is set from -10 µm to 10 µm. For copy paper, S_a = 3.39 µm, S_q = 4.35 µm and for carbon paper, S_a = 1.47 µm, S_q = 1.87 µm.

From the pictures above, it can be clearly seen that the surface of carbon paper is much smoother than the surface of copy paper. For copy paper, the average height of the surface topography is around 10.0 µm, but the distribution of the color scale varies from -10.0 µm to 10.0 µm. For carbon paper, the average height of the surface topography is around 4.0 µm, but it is different from copy paper, the range of the color scale concentrates around 0 ± 2.5 µm.

As mentioned above, a roughness value can either be calculated on a profile (line) or on a surface (area). For the profile roughness, the average roughness R_a is the most widely used parameter. For areal roughness parameters, the average areal roughness, S_a, is more common. Generally, R_a (Equation 3.10) and S_a (Equation 3.11) are calculated according to the following equations:

$$R_a = \frac{1}{l}\int_0^l \left|Z(x)\right| \,\mathrm{dx} \tag{3.10}$$

R_a expresses the arithmetical mean of the absolute values of the profile heights Z(x) in a sampling length l.

$$S_a = \frac{1}{A}\iint_A \left|Z(x,y)\right| \,\mathrm{dxdy} \tag{3.11}$$

S_a is a 3D parameter expanded from the roughness (2D) parameter R_a. It expresses the average of the absolute values of the areal heights Z(x, y) in the measured area A.

The root mean square height value S_q:

$$S_q = \sqrt{\frac{1}{A}\iint_A \left(Z(x,y)\right)^2 \,\mathrm{dxdy}} \tag{3.12}$$

The roughness parameters of carbon paper and copy paper were measured by using the Sensofar PLu Neox, the values are listed in the following table.

Table 3.5: The average roughness data of different papers that measured by using the Sensofar PLu Neox with the objective EPI 10X-N in Confocal Profiling mode. Each of the roughness values which listed below are the average values of three different tests.

Paper type	Side	Profile roughness R_a (µm)		Areal roughness S_a (µm)
		MD direction	CD direction	
Copy paper	side1	1.44	1.95	3.07
	side2	1.79	2.74	4.20
Carbon paper (Geha-1)	side1	0.75	0.92	1.71
	side2 (ink)	0.85	0.88	1.55

As mentioned before, MD is the machine direction and CD is the cross-machine direction. In Table 3.5, R_a is the average profile roughness that calculated in a random line in MD or CD direction, S_a is the mean surface roughness of the whole area. For copy paper, the R_a values are different in different sides. For carbon paper, side2 is the ink side, which is directly contact with the surface of copy paper, the S_a value of side2 is much smaller than side1.

The areal roughness value, S_a, is more important. The S_a value of carbon paper is nearly one third of the S_a value of copy paper. The surface of carbon paper is much smoother than the surface of copy paper. So, during the contact process, the surface of the copy paper is the major source of the deformation. But on the other hand, it should still be further discussed, how to describe the influence of the areal roughness from the standpoint of contact mechanics qualitatively.

3.6.2 Analysis of the mechanical behavior

Four experiments were implemented here to discuss the mechanical behavior influenced by the carbon paper. All the setups (a, b, c and d) are shown in Figure 3.20. The experimental procedure and parameters used for the experiments are the same as mentioned in the preceding section.

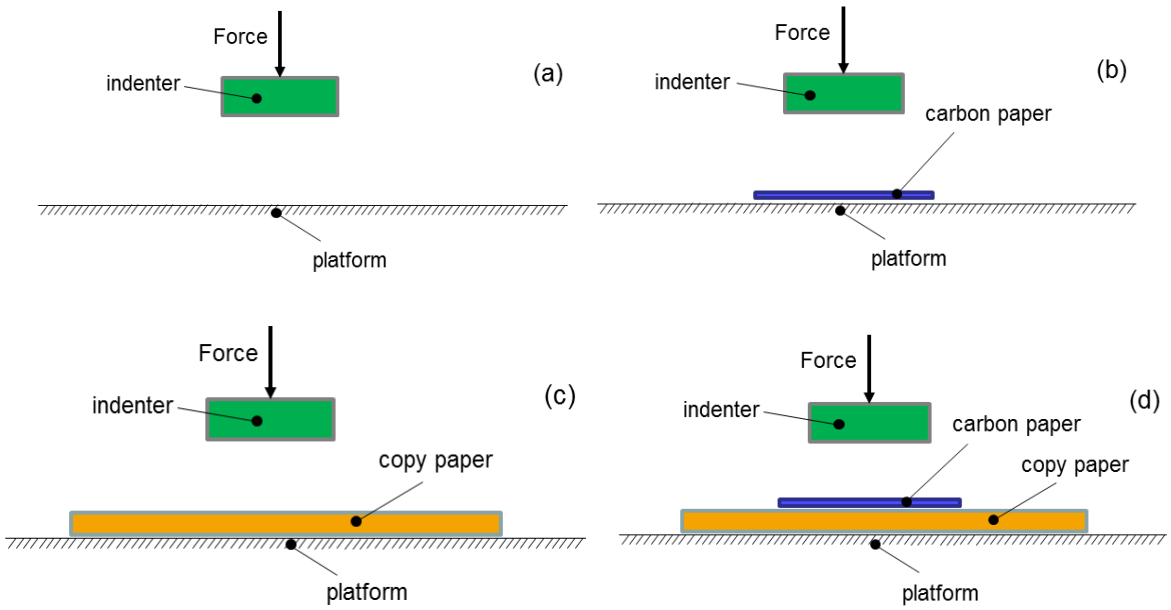

Figure 3.20: Setups used for comparing the compressive behavior of platform, carbon paper and copy paper. (a) is the setup for measuring the stress-strain behavior of the platform. Setup (b) is used for measuring the stress-strain curve of carbon paper. Likewise, setup (c) is used for only copy paper. (d) is the setup used for carbon paper together with the copy paper.

The experimental results of the above loading processes are shown in Figures 21, 22 and 23.

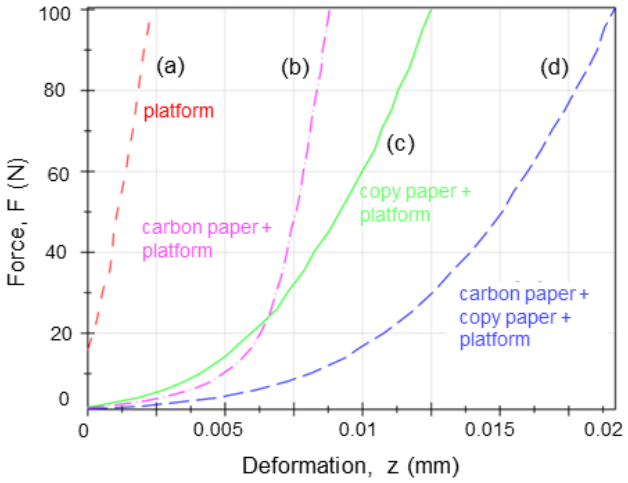

Figure 3.21: Compression curves of the platform, carbon paper (Geha-1) and copy paper. In this picture, curve (a) is the force-deformation curve of the platform, which is made of steel, the curve of the platform is linear. Curve (b), (c) and (d) are the force-deformation curves of paper materials together with the platform, which are typical J-shaped curves.

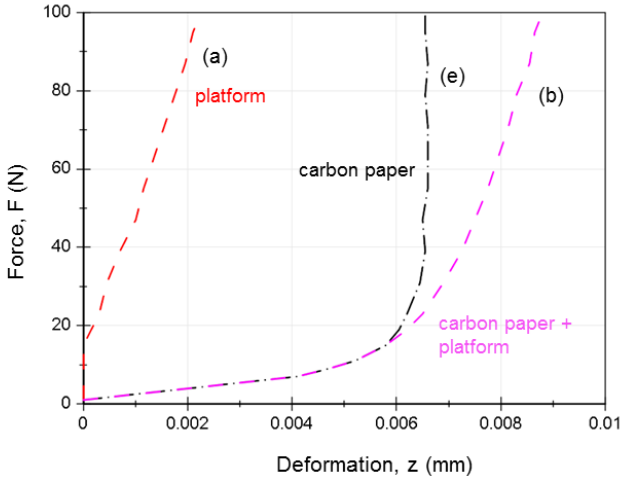

Figure 3.22: Comparison of the compression curves between platform and carbon paper (Geha-1). Curve (a) is the force-deformation curve of the platform, curve (b) is the force-deformation curve of carbon paper together with the platform, curve (e) is the force-deformation curve of only carbon paper, which is calculated by the deformation of carbon paper with platform (curve (b)) minus the deformation of the platform (curve (a)).

Figure 3.22 shows the comparisons of the force-deformation behavior between the platform and the carbon paper. We can see from curve (e) that the deformation of carbon paper mainly occurs under the condition of force smaller than 20 N, when the force is bigger than 20 N, the deformation of carbon paper will be very small. The force-deformation curve is nearly parallel to the force axis. Therefore, if the imposed force on the paper surface becomes more than 20 N, the mechanical behavior of paper influenced by the carbon paper will be quite limited.

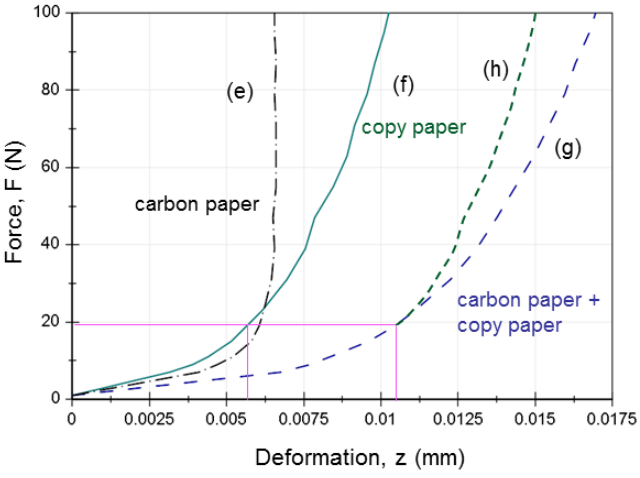

Figure 3.23: Comparison of the compression curves of copy paper (curve (f)) and carbon paper (Geha-1) together with copy paper (curve (g)). Curve (e) is the force-deformation curve of carbon paper. The dashed line (curve (h)) is the force-deformation curve of copy paper under the force changed from 20 N to 100 N, it is created by the movement of the original position of the curve (f).

Figure 3.23 shows the different compressive behaviors of copy paper (curve (f)) and carbon paper together with copy paper (curve (g)). The influence of the carbon paper mainly lies on the stage of force under 20 N. When the force is bigger than 20 N, the influence of the carbon paper on the compressive behavior of copy paper will be quite limited. Compared with only carbon paper, during the force changes from 20 N to 100 N, the deformation of carbon paper together with copy paper changed only around 0.0019 mm, which is around 10% of the total deformation (0.02 mm).

3.7 Summary

First of all, two important concepts were presented in this chapter: the actual compression modulus and the actual stress-strain curve of paper. On one hand, paper is not a linearly elastic material. But because of the long experience with linearly elastic metals, the idea of an E-modulus was usually carried over to the paper material. Actually, the physical meaning of such a modulus for paper is not clear (Mark and Borch, 2001). So in this paper, the concept of actual modulus was presented, the actual compression modulus of paper was calculated. On the other hand, nearly all presented researches up to now discussed the stress-strain curve of paper by using the nominal contact area. But actually, the stress-strain curve of paper is apparently affected by the surface topography. So the concept of actual stress-strain curve was introduced here to study the mechanical behavior of paper materials.

The next, a new experimental method was proposed to calculate the actual contact areas. Its calculation results identified the practicability of the method. Different types of carbon papers have been selected and compared here, with the help of actual contact areas obtained here, the actual compression modulus and the actual stress-strain curve of copy paper were calculated. The calculation results show the crucial differences between the actual and nominal stress-stain behaviors.

Furthermore, the influence of the carbon paper was also discussed from the standpoints of surface topography and mechanical behavior. From the standpoint of surface topography, the surface of carbon paper is much smoother than the surface of copy paper, the surface of the copy paper is the major source of the deformation. From the standpoint of mechanical behavior, the platform is not ideally stiff and the carbon paper shows a J-shaped curve. The comparison results indicate that the influence of the carbon paper on the compressive behavior of copy paper mainly exists when the force is smaller than 20 N.

In summary, according to the above research results, the stress-strain curve of paper calculated by using the actual contact area is totally different from the calculation result of the nominal contact area. The mechanical behavior of paper materials under compressing by considering the surface roughness is very close to the general elastic-plastic materials. The influence of the surface roughness cannot be ignored, special attention should be given to the research of the paper surface topography.

4 Theoretical model for paper and paper stacks

In this chapter, paper is regarded as an elastic material. With considering the structure of paper, the paper body is divided into two surface structures and one internal structure. Two different calculation methods proposed by Schaffrath (Schaffrath and Gottsching, 1991, Schaffrath, 1993, Schaffrath and Göttsching, 1992b, Schaffrath and Göttsching, 1992a) will be introduced and compared in Sections 4.1 to 4.3, in which the relationship between the surface (internal) deformation and total deformation will be calculated by using the Newton-Raphson method. Then, the calculation model of one sheet will be extended to calculate the force-deformation relationship of multiple sheets in Section 4.4. After that, the results between the calculation and experiments will be compared. Section 4.5 summarizes the results of this investigation.

Part of the work described in this chapter was published in (Chen et al., 2014a):

Jian Chen, Jann Neumann, Edgar Dörsam: *Investigation on deformation behavior of paper in Z-direction*. Progress in paper physics, Raleigh, North Carolina, USA; 09/2014

4.1 Schaffrath's model of a single sheet

According to the model proposed by Schaffrath (Schaffrath and Gottsching, 1991, Schaffrath and Göttsching, 1992b, Schaffrath and Göttsching, 1992a, Schaffrath, 1993), the paper body was expressed as two rough surfaces and one internal structure, which is shown in Figure 4.1.

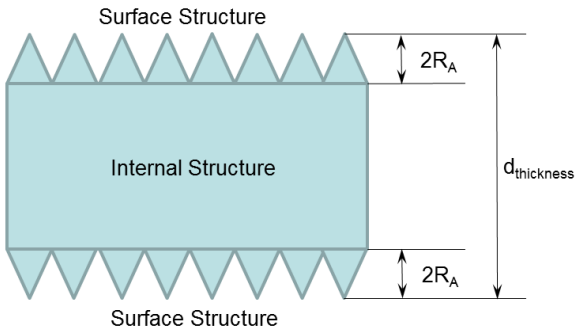

Figure 4.1: Schematic diagram of the abstraction model of paper structure proposed by Schaffrath. The paper structure consists of three parts: two surface structures and one internal structure. In this picture, $d_{thickness}$ is the thickness of the paper, R_A is the average value of the surface roughness plus standard deviation of the caliper (Schaffrath and Gottsching, 1991, Schaffrath and Göttsching, 1992b, Schaffrath and Göttsching, 1992a, Schaffrath, 1993) .

In this model, the paper surface structure was described by using the pyramid elements, as shown in Figure 4.2, the internal structure was described by using the tubular elements, as shown in Figure 4.3.

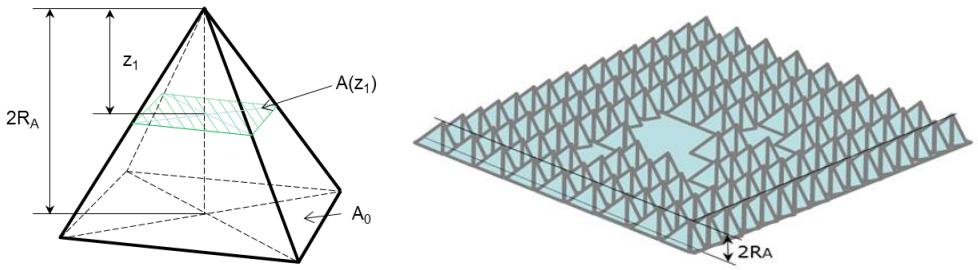

Figure 4.2: Elementary unit of the surface structure. The rough surface is expressed by using the pyramid elements, z_1 is the deformation of the surface, $A(z_1)$ is the contact area of the surface, A_0 is the nominal area of the surface (Schaffrath and Gottsching, 1991, Schaffrath, 1993, Schaffrath and Göttsching, 1992b).

For the surface element, when the deformation of the surface structure is z_1, the relationship between the surface deformation z_1 and the actual contact area $A(z_1)$ can be described as:

$$A(z_1) = \frac{A_0 \cdot (z_1)^2}{4 \cdot (R_A)^2} \tag{4.1}$$

As described in Figures 4.1 and 4.2, in Equation 4.1, z_1 is the surface deformation, A_0 is the nominal area of the surface. $A(z_1)$ is the actual contact area of the surface, R_A is the value of adding the surface roughness R_a and the standard deviation of the caliper s together.

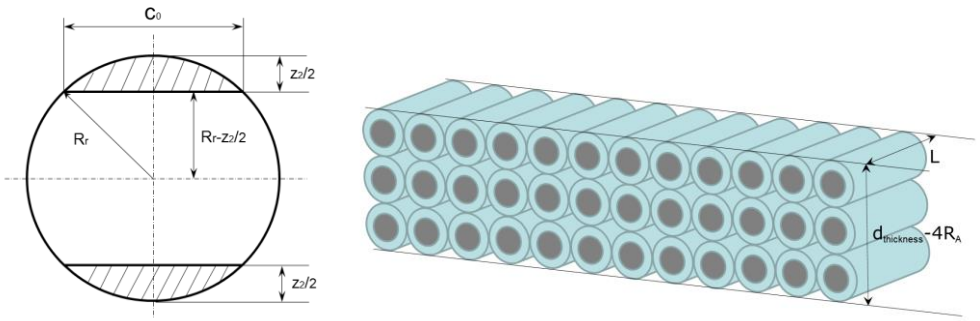

Figure 4.3: Elementary units of the internal structure. The internal structure is described by using the tubular elements, z_2 is the deformation of the internal structure, c_0 is the width of the contact area which happened in the circle element, L is the length of the fiber and R_r is the radius of curvature at the point (line) where the fibers contact each other (Schaffrath and Gottsching, 1991, Schaffrath, 1993, Schaffrath and Göttsching, 1992b).

For the elementary units of the internal structure, when the deformation of the internal structure is z_2, the relationship between the internal deformation z_2 and the contact area of the internal structure $A(z_2)$ can be described as:

$$A(z_2) = 2 \cdot L \sqrt{(R_r)^2 - \left(R_r - \frac{z_2}{2}\right)^2} \tag{4.2}$$

As mentioned in Figure 4.3, in Equation 4.2, L is the length of the fiber, R_r is the radius of curvature at the point (line) where the fibers contact each other.

4.1.1 Calculation of one sheet according to Hooke's law

According to the Hooke's law, which was introduced as Equations 3.1 and 3.2 in Section 3.3.4, the forces can be expressed as the product of the actual contact area A(z), actual modulus E(z), deformation z and the inverse of the thickness of the material $d_{thickness}$, which is shown here again:

$$F(z) = \frac{E(z) \cdot A(z)}{d_{thickness}} \cdot z \tag{4.3}$$

Based on Equations 4.1 to 4.3, the force-deformation relationship of the surface structure and the internal structure can be calculated, respectively. The schematic diagram of paper under compression is shown in Figure 4.4.

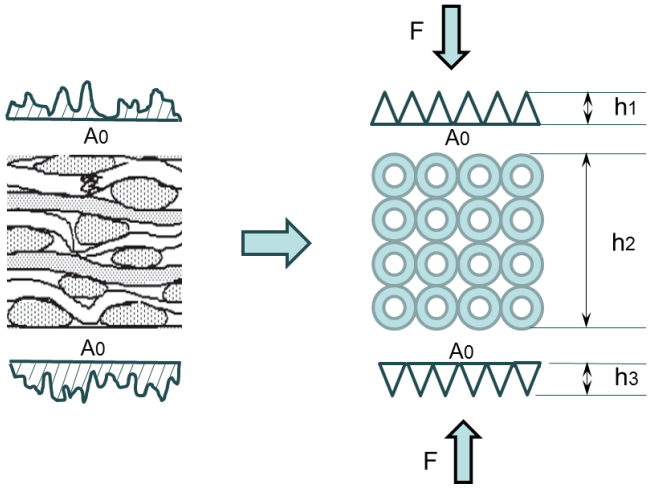

Figure 4.4: Paper structure and paper model under compression. A_0 is the nominal area of the surface, h_1, h_2, h_3 are the initial heights of the different parts (Schaffrath and Gottsching, 1991, Schaffrath and Göttsching, 1992b, Schaffrath and Göttsching, 1992a, Schaffrath, 1993).

As shown in Figure 4.4, the force imposed on the surface structure and internal structure is the same one (F). Besides, for both of the components, the nominal contact area is A_0. Then, the

force-deformation relationships of surface and internal structures can be obtained according to Equation 4.4.

$$\begin{cases} F = \dfrac{E \cdot A(z_1)}{h_1} \cdot z_1 = \dfrac{E(z_1) \cdot A_0 \cdot z_1^{\,3}}{8 \cdot (R_A)^3} \\ F = \dfrac{E \cdot A(z_2)}{h_2} \cdot z_2 = \dfrac{E(z_2) \cdot 2 \cdot \sqrt{(R_r)^2 - (R_r - \dfrac{z_2}{2 \cdot n_0})^2} \cdot L \cdot m_0}{d_{thickness} - 4 \cdot R_A} \cdot z_2 \\ F = \dfrac{E \cdot A(z_3)}{h_3} \cdot z_3 = \dfrac{E(z_3) \cdot A_0 \cdot z_3^{\,3}}{8 \cdot (R_A)^3} \end{cases} \tag{4.4}$$

Where $E(z_1)$ and $E(z_3)$ are the moduli of the surface structure, $E(z_2)$ is the modulus of the internal structure, A_0 is the nominal area of the contact surface, h_1, h_2, h_3 are the initial heights of the different parts. In this dissertation, $h_1 = h_3 = 2 \cdot R_A$, $h_2 = d_{thickness} - 4 \cdot R_A$, m_0 and n_0 are the parameters used to determine the amount of internal units and $R_A = R_a + s$.

In addition, the following equation has to be taken into account:

$$z_1 + z_2 + z_3 = z \tag{4.5}$$

In the equations above, z is the total deformation.

In this method, the differences between the upper and the lower surfaces were ignored. When the force imposed on the paper body is the same, the deformations of the two surfaces are equal to each other, so $z_1 = z_3$. The paper is regarded as an elastic material, $E(z_1) = E(z_2) = E(z_3)$:

$$\begin{cases} E(z_1) = E(z_2) = E(z_3) \\ z_1 = z_3 \end{cases} \tag{4.6}$$

The force applied on the paper body is the same, Equation 4.4 can be simplified as:

$$\frac{E(z_1) \cdot A_0 \cdot z_1^{\,3}}{8 \cdot (R_A)^3} = \frac{E(z_2) \cdot 2 \cdot \sqrt{(R_r)^2 - (R_r - \dfrac{z_2}{2 \cdot n_0})^2} \cdot L \cdot m_0}{d_{thickness} - 4 \cdot R_A} \cdot z_2 \tag{4.7}$$

The deformation of the surface structure z_1 can be written as:

$$z_1 = \sqrt[3]{\frac{16 \cdot (R_A)^3 \cdot z_2 \cdot \sqrt{(R_r)^2 - (R_r - \dfrac{z_2}{2 \cdot n_0})^2} \cdot L \cdot m_0}{A_0 \cdot (d_{thickness} - 4 \cdot R_A)}} \tag{4.8}$$

By combining Equation 4.5 with 4.6, and substituting Equation 4.8 into Equation 4.5, it can be obviously deduced that:

$$z = z_1 + z_2 + z_3 = 2 \cdot z_1 + z_2$$
$$= 2 \cdot \sqrt[3]{\frac{16 \cdot (R_A)^3 \cdot \sqrt{\frac{m_0^{\,2} \cdot L^2 \cdot R_r \cdot z_2}{n_0} - \frac{m_0^{\,2} \cdot L^2 \cdot (z_2)^2}{4 \cdot n_0^{\,2}}} \cdot z_2}{A_0 \cdot (d_{thickness} - 4 \cdot R_A)}} + z_2 \tag{4.9}$$

There is one equation (Equation 4.9) but two unknown variables (z_2 and z). The relationship between z_1 (or z_2) and z can be calculated by using the Newton-Raphson method (Shodor, 1997). In numerical analysis, Newton's method (also known as the Newton-Raphson method, as shown in Figure 4.5), which was named after Isaac Newton and Joseph Raphson, is a method for finding successively better approximations to the roots (or zeroes) of a real-valued function.

$$\begin{cases} F(z_2) = 2 \cdot \sqrt[3]{\frac{16 \cdot (R_A)^3 \cdot \sqrt{B_0 + B_1 \cdot z_2 - B_2 \cdot (z_2)^2} \cdot z_2}{A_0 \cdot (d_{thickness} - 4 \cdot R_A)}} + z_2 - z = 0 \\ z_2(i+1) = z_2(i) - \frac{F(z_2(i))}{F'(z_2(i))} \end{cases} \tag{4.10}$$

Where:

$$B_1 = \frac{m_0^{\,2} \cdot L^2 \cdot R_r}{n_0} \quad \text{and} \quad B_2 = \frac{m_0^{\,2} \cdot L^2}{4 \cdot n_0^{\,2}} \tag{4.11}$$

In Equation 4.10, B_0 is calculated according to the initial area in the internal paper structure for withstanding the load (Schaffrath and Göttsching, 1992b). It is calculated based on the assumption that at the beginning of the contact, $B_1 = B_2 = 0$, the initial area in the internal paper structure to withstand the force is 56% of the nominal area of the indenter (Schaffrath and Göttsching, 1992b), then calculating according to Equation 4.2.

$$A(z_2) = 56\% \cdot A_0 = 2 \cdot \sqrt{B_0} \tag{4.12}$$

For copy paper, $B_0 = 62.68\ mm^4$.

The Newton-Raphson method starts with a function $F(z_2)$ defined over the real number z_2, the deviative of the function $F'(z_2)$ and an initial guess value $z_2(0)$ for a root of the function.

In Equation 4.10 and Figure 4.5, $z_2(i)$ is the current known z_2-value, $F(z_2(i))$ represents the value of the function at $z_2(i)$, and $F'(z_2(i))$ is the derivative (slope) at $z_2(i)$. $z_2(i+1)$ represents the next z_2-value that you are trying to find. In addition, e_{all} is the allowed error for calculating the root. i_{max} is the desired maximum iteration times.

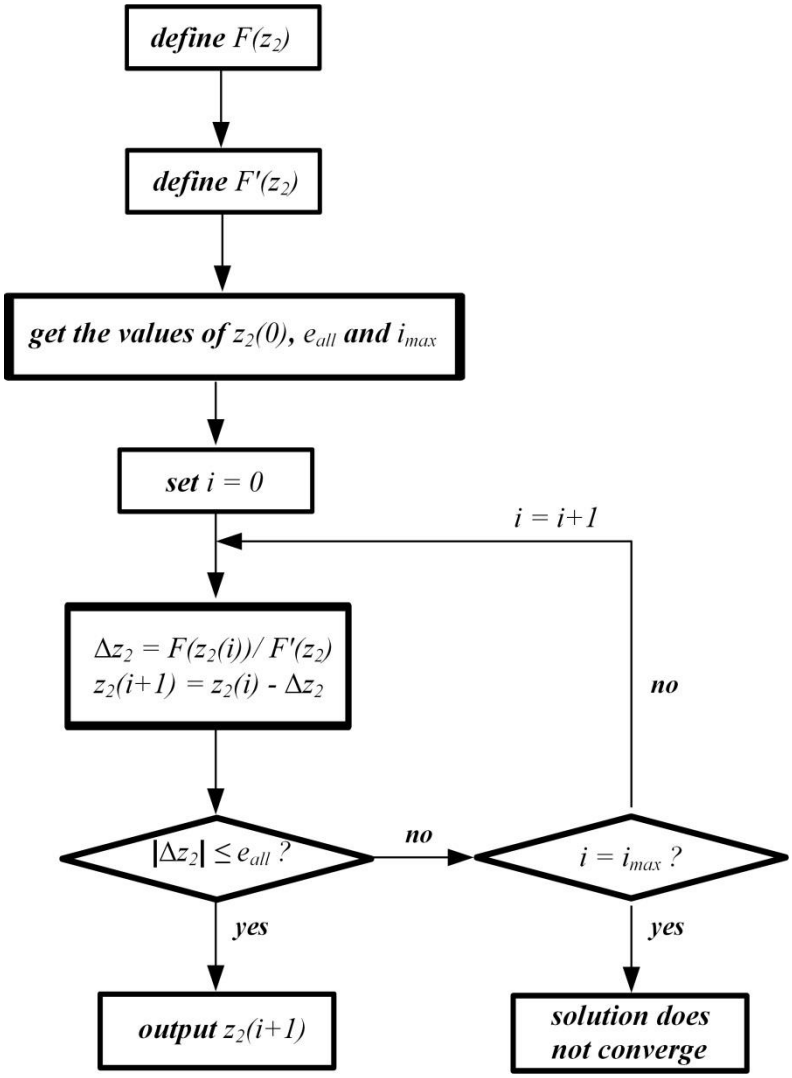

Figure 4.5: Flowchart of the Newton-Raphson method. This method was invented by Isaac Newton and Joseph Raphson (Shodor, 1997). e_{all} is the allowed error for calculating the root. i_{max} is the desired maximum iteration times.

Essentially, $F'(z_2)$, the derivative represents $F(z_2)/dz_2$ ($dz_2 = \Delta z_2$). Therefore, the term $F(z_2)/F'(z_2)$ represents a value of Δz_2.

$$\frac{F(z_2)}{F'(z_2)} = \frac{F(z_2)}{F(z_2)/\Delta z_2} = \Delta z_2 \tag{4.13}$$

When $\Delta z_2 \le e_{all}$, the value of $z_2(i+1)$ can be regarded as one root of the function.

By using the Newton-Raphson method, for a given value of the total deformation z, the deformation of the internal structure z_2 can be calculated.

In the above equations, most of the parameters ($d_{thickness}$, R_A, m_0, n_0, A_0, L, R_r, B_0, B_1, B_2, s) can be defined easily and all the values will be provided in Section 4.2.

4.1.2 Calculation of one sheet according to Paetow's method

Another method is according to the out-of-plane tensile stress-strain relation of paper materials that was proposed by Paetow and Göttsching (Paetow and Göttsching, 1990):

$$\sigma = E^{ini} \cdot \frac{1}{1+\varepsilon \cdot \frac{E^{ini}}{S}} \cdot \varepsilon \tag{4.14}$$

Where, E^{ini} is the initial E-modulus, S is the limiting stress (Paetow and Göttsching, 1990), which is calculated according to the relationship between the strain divide stress (ε/σ) and strain (ε). For the surface structure and the internal structure, the relationship between contact area and nominal area are provided in Equations 4.1 and 4.2, respectively. Combining with Equation 4.14, the relationship between force and deformation of each structure can be obtained as follows (Schaffrath and Göttsching, 1992b):

$$\begin{cases} F = \sigma_1 \cdot A(z_1) = \dfrac{E^{ini} \cdot A(z_1) \cdot \varepsilon_1}{1+\varepsilon_1 \cdot \dfrac{E^{ini}}{S}} = \dfrac{E^{ini} \cdot A(z_1) \cdot z_1}{2 \cdot R_A \left(1+\dfrac{z_1 \cdot E^{ini}}{2 \cdot R_A \cdot S}\right)} = \dfrac{E^{ini} \cdot A_0 \cdot (z_1)^3}{\left(z_1 \cdot \dfrac{E^{ini}}{S} + 2 \cdot R_A\right) \cdot 4 \cdot (R_A)^2} \\ F = = \sigma_2 \cdot A(z_2) = \dfrac{E^{ini} \cdot A(z_2) \cdot z_2}{\left(1+\dfrac{z_2 \cdot E^{ini}}{(d_{thickness} - 4 \cdot R_A) \cdot S}\right)(d_{thickness} - 4 \cdot R_A)} = \dfrac{2 \cdot E^{ini} \cdot z_2 \cdot \sqrt{B_0 + B_1 \cdot z^2 - B_3 \cdot (z_2)^2}}{d_{thickness} - 4 \cdot R_A + \dfrac{z_2 \cdot E^{ini}}{S}} \end{cases} \tag{4.15}$$

Where σ_1 and σ_2 are the stress values of the surface and internal structures, ε_1 and ε_2 are the corresponding strain values. All other parameters in the above equation have been described in Equations 4.1 to 4.14. The force imposed on the surface structure and internal structure is the same one. So, according to Equation 4.15, it can be obtained that:

$$\frac{(z_1)^3}{z_1 \cdot \dfrac{E^{ini}}{S} + 2 \cdot R_A} = \frac{8 \cdot (R_A)^2 \cdot z_2 \cdot \sqrt{B_0 + B_1 \cdot z^2 - B_3 \cdot (z_2)^2}}{\left(d_{thickness} - 4 \cdot R_A + \dfrac{z_2 \cdot E^{ini}}{S}\right) \cdot A_0} \tag{4.16}$$

By using the Newton-Raphson method again, we can construct the following function:

$$\begin{cases} F(z_2) = \dfrac{(z_1)^3}{z_1 \cdot \dfrac{E^{ini}}{S} + 2 \cdot R_A} - \dfrac{8 \cdot (R_A)^2 \cdot z_2 \cdot \sqrt{B_0 + B_1 \cdot z_2 - B_3 \cdot (z_2)^2}}{\left(d_{thickness} - 4 \cdot R_A + \dfrac{z_2 \cdot E^{ini}}{S}\right) \cdot A_0} = 0 \\ z_2(i+1) = z_2(i) - \dfrac{F(z_2(i))}{F'(z_2(i))} \end{cases} \tag{4.17}$$

For a given z_1 value, the value of z_2 can also be calculated according to the Newton-Raphson method as shown in Figure 4.5.

4.2 Determining the parameters

The fiber information was measured by using the FiberLab equipment which is produced by the Metso company. For the copy paper used in this dissertation, the fiber length L is 0.885 mm, the width of the fiber w is 0.018 mm. The diameter of the indenter is 6 mm, so the nominal area of the indenter A_0 is 28.27 mm^2.

According to the values provided above and in Table 4.1, the values of m_0 and n_0 can be calculated by using the following equations:

$$m_0 = \frac{A_0}{L \cdot w} \approx 1778 \quad \text{and} \quad n_0 = \frac{d_{thickness} - 4 \cdot R_A}{w} \approx 4 \tag{4.18}$$

Then, according to Equation 4.11, the values of B_1 and B_2 can be calculated, the value of B_0 provided in Schaffrath's model is 950.0 mm^4, which is calculated according to his own paper material and equipments. For the copy paper used in this dissertation, the value of B_0 = 62.68 mm^4.

As mentioned in Section 3.4, the modulus of paper material in the out-of-plane is not a constant value, which cannot be simply described by using the E-modulus. In this chapter, the paper material is considered as an elastic material. Both the E-modulus and the initial modulus in this chapter are set as 27.0 N/mm^2.

All of the parameters used in this chapter are listed in Table 4.1.

Table 4.1: Parameters set in the proposed model. In the model proposed by Schaffrath, some values were not provided, for example: the fiber width w, the E-modulus E, and so on. Some other values, such as: R_a, R_r and s are selected according to Schaffrath's model (Schaffrath and Gottsching, 1991, Schaffrath, 1993, Schaffrath and Göttsching, 1992b).

Parameters	Values provided in Schaffrath's model	Model based on Hooke's law	Model based on Paetow's method
Fiber length L	1.00 mm	0.89 mm	0.89 mm
Fiber width w	-	1.80×10^{-2} mm	1.80×10^{-2} mm
Thickness of the paper $d_{thickness}$	0.1 mm	8.47×10^{-2} mm	8.47×10^{-2} mm
Nominal area of the indenter A_0	110 mm^2	28.27 mm^2	28.27 mm^2
Average surface roughness R_a	2.50×10^{-3} mm	2.50×10^{-3} mm	2.50×10^{-3} mm
Standard deviation of the caliper s	2.50×10^{-3} mm	2.50×10^{-3} mm	2.50×10^{-3} mm

Radius of curvature at the point (line) where the fibers contact each other R_r	30 mm	30 mm	30 mm
E	-	27 N/mm^2	-
E^{ini}	5000 N/mm^2	-	27 N/mm^2
m_0	700	1778	1778
n_0	10	4	4
B_0	950 mm^4	62.68 mm^4	62.68 mm^4
B_1	1.50×10^6 mm^3	1.86×10^7 mm^3	1.86×10^7 mm^3
B_2	1.25×10^3 mm^2	3.87×10^4 mm^2	3.87×10^4 mm^2
S	80 N/mm^2	-	80 N/mm^2

Based on the parameters obtained above, by using the Newton-Raphson method, for a given deformation value (for example, total deformation z), the values of other deformations (surface deformation z_1 and internal deformation z_2) can be calculated (Equation 4.10). Then, according to the curve fitting method, the relational expression between z_1 and z can be obtained.

4.3 Calculation results of a single sheet

In Section 4.1, two different methods were introduced for calculating the relationship between the total deformation z and the deformation of the surface z_1 (or the internal deformation z_2). In both of them, the Newton-Raphson method was proposed to find the roots of the functions. The paper used for doing the research is the normal copy paper, all the parameters needed in these methods are listed in Table 4.1. According to the parameters obtained above, the relationship between the total deformation z and the surface deformation z_1 can be calculated. Then, the models for calculating the force-deformation curves can be derived. In the following sections, the steps of calculating the force-deformation curve of a single copy paper will be introduced in detail.

4.3.1 Results based on Hooke's law

According to Equation 4.10, for a given z value, the values of z_1 and z_2 can be calculated. The value of the total deformation z changed from 0 mm to 0.06 mm with a substep length of 0.005 mm. The calculation results are shown in Table 4.2.

Table 4.2: Calculated results by using the Hooke's law (see Equation 4.10). All the results of surface deformation z_1 and internal structure deformation z_2 under some given total deformation values z were calculated by using the Newton-Raphson method (see Appendix A3). $2 \cdot z_1/z$ is the percentage of the surface deformation occupied in the total deformation.

Total deformation z (mm)	Deformation of the surface structure z_1 (mm)	Deformation of the internal structure z_2 (mm)	$2 \cdot z_1/z$ (%)
0.00×10^{-2}	0.00×10^{-2}	0.00×10^{-2}	0.00
0.50×10^{-2}	0.24×10^{-2}	0.02×10^{-2}	97.05
1.00×10^{-2}	0.46×10^{-2}	0.08×10^{-2}	92.64
1.50×10^{-2}	0.67×10^{-2}	0.16×10^{-2}	89.42
2.00×10^{-2}	0.87×10^{-2}	0.26×10^{-2}	86.89
2.50×10^{-2}	1.05×10^{-2}	0.39×10^{-2}	84.23
3.00×10^{-2}	1.23×10^{-2}	0.54×10^{-2}	82.04
3.50×10^{-2}	1.40×10^{-2}	0.70×10^{-2}	80.06
4.00×10^{-2}	1.56×10^{-2}	0.87×10^{-2}	78.24
4.50×10^{-2}	1.72×10^{-2}	1.05×10^{-2}	76.57
5.00×10^{-2}	1.88×10^{-2}	1.25×10^{-2}	75.01
5.50×10^{-2}	2.02×10^{-2}	1.45×10^{-2}	73.57
6.00×10^{-2}	2.17×10^{-2}	1.67×10^{-2}	72.22

On the basis of the data above, the values of z and z_1 were plotted in a same coordinate system. Then, the relationship between the total deformation and the deformation of the surface structure can be described by using different curve fitting methods (Equations 4.19 and 4.20).

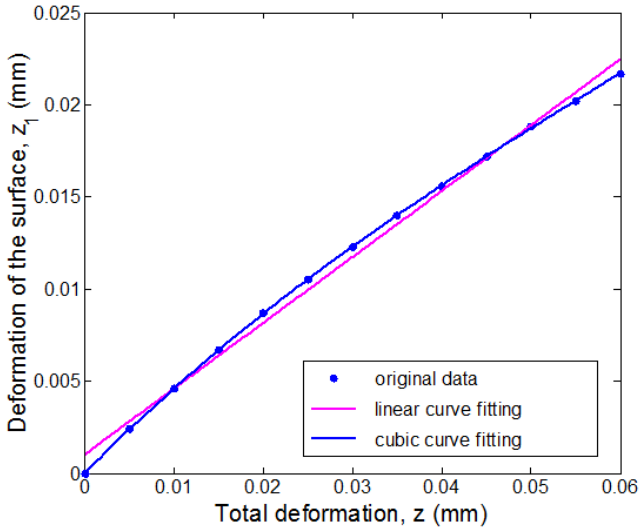

Figure 4.6: Relationship between the total deformation z and the deformation of the surface structure z_1. These blue points are the original calculated data, the pink line is the linear fitting curve (Equation 4.19, the coefficient of determination: $R^2 = 0.994$) and the blue line is the cubic fitting curve (Equation 4.20, the coefficient of determination: $R^2 = 1.0$) (see Appendix A6).

Figure 4.6 shows that the relationship between the total deformation and the surface deformation can be described by using linear curve fitting or cubic curve fitting method. The functions of these two different curve fitting methods are provided below, by using the linear curve fitting method:

$$z_1 = 0.36 \cdot z + 0.001 \tag{4.19}$$

By using the cubic curve fitting method:

$$z_1 = 17 \cdot z^3 - 3.1 \cdot z^2 + 0.49 \cdot z + 0.000016 \tag{4.20}$$

For linear curve fitting, the coefficient of determination: $R^2 = 0.994$. For cubic curve fitting, the coefficient of determination: $R^2 = 1.0$. Then, by substituting Equations 4.19 into Equation 4.4, the following force-deformation equations can be obtained.

$$F = \frac{E(z_1) \cdot A_0 \cdot z_1^{\,3}}{8 \cdot (R_A)^3} = \frac{E \cdot A_0 \cdot (0.36 \cdot z + 0.001)^3}{8 \cdot (R_A)^3} \tag{4.21}$$

And by substituting Equation 4.20 into Equation 4.4:

$$F = \frac{E(z_1) \cdot A_0 \cdot z_1^{\,3}}{8 \cdot (R_A)^3} = \frac{E \cdot A_0 \cdot (17 \cdot z^3 - 3.1 \cdot z^2 + 0.49 \cdot z + 0.00001)^3}{8 \cdot (R_A)^3} \tag{4.22}$$

The force-deformation curves can be drawn, which are shown in Figure 4.7.

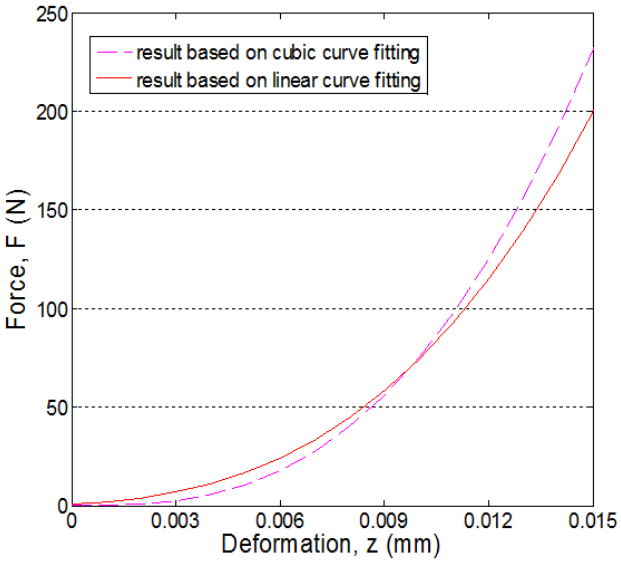

Figure 4.7: Calculated force-deformation curve based on different curve fitting methods. The red line is the result (Equation 4.21) based on linear curve fitting equation (Equation 4.19) and the pink dashed line is the result (Equation 4.22) based on cubic curve fitting equation (Equation 4.20) (see Appendix A9).

In Figure 4.7, the force-deformation curves of paper were calculated according to the Hooke's law. Both of the linear and cubic curve fitting methods were used for calculating the force-deformation relationship of paper material. The Hooke's law can be well used, especially, when the force is very small. The deviations between the two different methods will increase with the increasing of the force.

4.3.2 Results based on Paetow's method

According to Equation 4.17, by using the Newton-Raphson method, for a given z_1 value, the values of z and z_2 can be calculated. The values of the surface deformation z_1 are set according to Table 4.2. The calculated results of total deformation z and internal deformation z_2 are shown in Table 4.3.

Table 4.3: Calculated results by using the Paetow's method (see Equation 4.17). The values of the surface deformation z_1 are set according to Table 4.2 and $2 \cdot z_1/z$ is the percentage of the surface deformation occupied in the total deformation (program code see Appendix A4).

Total deformation z (mm)	Deformation of the surface structure z_1 (mm)	Deformation of the internal structure z_2 (mm)	$2 \cdot z_1/z$ (%)
0.00×10^{-2}	0.00×10^{-2}	0.00×10^{-2}	0.00
0.50×10^{-2}	0.24×10^{-2}	0.02×10^{-2}	96.07

0.99×10^{-2}	0.46×10^{-2}	0.07×10^{-2}	92.96
1.48×10^{-2}	0.67×10^{-2}	0.14×10^{-2}	90.34
1.97×10^{-2}	0.87×10^{-2}	0.23×10^{-2}	88.10
2.43×10^{-2}	1.05×10^{-2}	0.33×10^{-2}	86.26
2.91×10^{-2}	1.23×10^{-2}	0.45×10^{-2}	84.57
3.37×10^{-2}	1.40×10^{-2}	0.57×10^{-2}	83.08
3.82×10^{-2}	1.56×10^{-2}	0.70×10^{-2}	81.76
4.27×10^{-2}	1.72×10^{-2}	0.83×10^{-2}	80.52
4.74×10^{-2}	1.88×10^{-2}	0.98×10^{-2}	79.34
5.16×10^{-2}	2.02×10^{-2}	1.12×10^{-2}	78.36
5.61×10^{-2}	2.17×10^{-2}	1.27×10^{-2}	77.36

Based on Table 4.3, the relationship between the total deformation and the deformation of the surface structure can be calculated by using different curve fitting methods (Equations 4.23 and 4.24), as shown in the following figure.

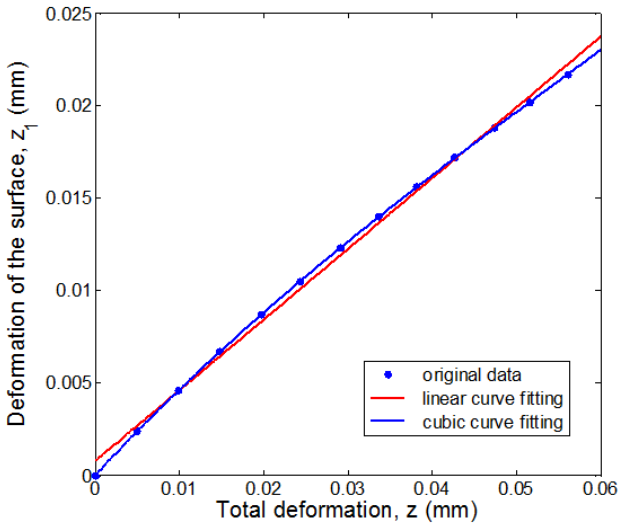

Figure 4.8: Relationship between the total deformation z and the deformation of the surface structure z_1. The blue points are the original calculated data, the pink line is the result of linear curve fitting method (Equation 4.23, the coefficient of determination: $R^2 = 0.997$) and the blue line is the result based on the cubic curve fitting method (Equation 4.24, the coefficient of determination: $R^2 = 1.000$) (see Appendix A7).

We can see from Figure 4.8 that, the relationship between total deformation and surface deformation can also be described by using both linear and cubic curve fitting methods. The function of linear curve fitting is provided below:

$$z_1 = 0.38 \cdot z + 0.00078 \tag{4.23}$$

And the cubic curve fitting function:

$$z_1 = 15 \cdot z^3 - 2.6 \cdot z^2 + 0.49 \cdot z + 0.000015 \tag{4.24}$$

The coefficient of determination for the linear curve fitting is $R^2 = 0.997$, the coefficient of determination for the cubic curve fitting is $R^2 = 1.000$. Then, by substituting the above equations (Equations 4.23 and 4.24) into Equation 4.14, the following equations can be obtained. Then, according to Equations 4.25 and 4.26, the force-deformation curves can be drawn. Based on linear curve fitting function (Equation 4.23):

$$F = \frac{E^{ini} \cdot A(z_1) \cdot z_1}{2 \cdot R_A \cdot \left(1 + \frac{z_1 \cdot E^{ini}}{2 \cdot R_A \cdot S}\right)} = \frac{E^{ini} \cdot A_0 \cdot (0.38 \cdot z + 0.00078)^3}{\left[(0.38 \cdot z + 0.00078) \cdot \frac{E^{ini}}{S} + 2 \cdot R_A\right] \cdot 4 \cdot (R_A)^2} \tag{4.25}$$

According to the cubic curve fitting function (Equation 4.24):

$$F = \frac{E^{ini} \cdot A(z_1) \cdot z_1}{2 \cdot R_A \left(1 + \frac{z_1 \cdot E^{ini}}{2 \cdot R_A \cdot S}\right)} = \frac{E^{ini} \cdot A_0 \cdot (15 \cdot z^3 - 2.6 \cdot z^2 + 0.49 \cdot z + 0.000015)^3}{\left[(15 \cdot z^3 - 2.6 \cdot z^2 + 0.49 \cdot z + 0.000015) \cdot \frac{E^{ini}}{S} + 2 \cdot R_A\right] \cdot 4 \cdot (R_A)^2} \tag{4.26}$$

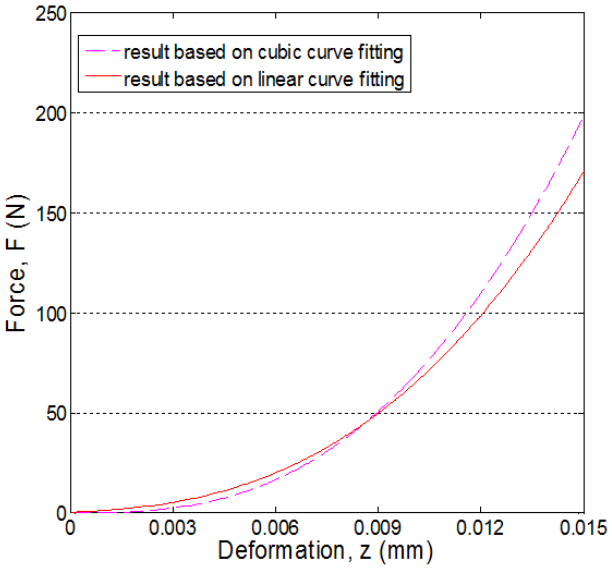

Figure 4.9: Calculated force-deformation curve according to different curve fitting methods. The red line is the result (Equation 4.25) based on linear curve fitting equation (Equation 4.23), and the pink dashed line is the result (Equation 4.26) based on cubic curve fitting equation (Equation 4.24) (program code see Appendix A10).

In Figure 4.9, the force-deformation curves of paper were calculated based on the Paetow's method. It's obvious that both of the linear and cubic curve fitting methods can be used for calculating the force-deformation relationship of paper material. But the deviations between the two different methods will increase with the increasing of the force, which is very similar to the results shown in Figure 4.7.

If comparing Figure 4.9 with Figure 4.7, it can be seen that the calculated result based on the cubic curve fitting in Figure 4.9 is much closer to the result based on the linear curve fitting in Figure 4.7. When the force is 200 N, both of the deformations of which are around 0.015 mm.

4.3.3 Comparisons between the two different methods

For the results (the relationship between surface deformation z_1 and total deformation z) based on the linear curve fitting, the force-deformation curves of different models (Equations 4.21 and 4.25) were put together in a same coordinate system and compared with the experimental result, as shown in Figure 4.10.

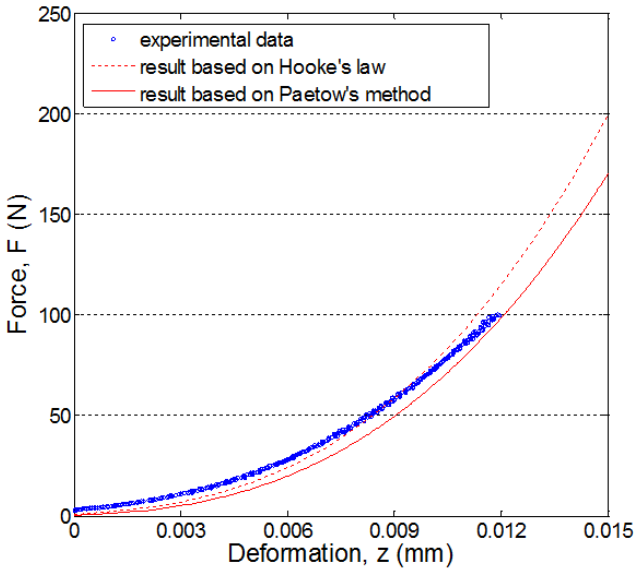

Figure 4.10: Calculated force-deformation curves compared with the experimental result. The blue line is the experimental data of a random test (test1 in Figure 2.10). The red dashed curve is the result based on Hooke's law (Equation 4.21), the red curve below is the result based on Paetow's method (Equation 4.25). The relationship between total deformation z and the surface deformation z_1 is calculated based on the linear curve fitting.

As shown in Figure 4.10, two totally different methods were used for calculating the force-deformation relationship of paper. A set of experimental data was also plotted in the same figure. On one hand, the calculation results are based on the assumption that the force is changing from 0 N. Because of a preload is set in the experimental process, so the force in the experiment is not starting from 0 N. On the other hand, for one sheet, the force-deformation results are quite different in different positions because of the heterogeneous densities of the

copy paper. Both of which lead to the deviation between the calculation and experimental results.

4.4 New theoretical models of multiple sheets

The models for a single sheet were described in the previous sections. For multiple sheets, the total deformation can also be divided into two parts: the deformation of the surface structures and the deformation of the internal structures. The relationship between the total deformation z and the surface deformation z_1 can also be built according to the Hooke's law and calculated by using the Newton-Raphson method.

4.4.1 Modelling of multiple sheets

As shown in Figure 4.11, each sheet consists of two surfaces and one internal structure. Supposing that the number of papers is n, the number of surfaces is 2n and the number of internal structure is n. Based on the model of one sheet, the mathematical model for multiple sheets can also be derived:

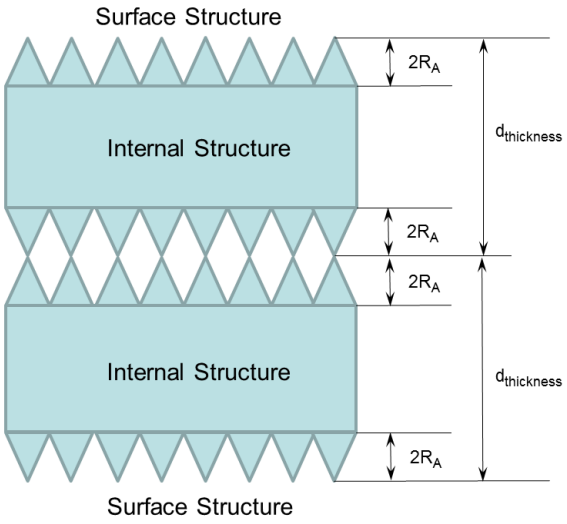

Figure 4.11: Schematic diagram of contact between papers. In this picture, $d_{thickness}$ is the thickness of paper. The elementary units of the surface structure and the internal structure are shown in Figures 4.2 and 4.3.

According to Equation 4.5, we can draw the relationship between total deformation z and surface deformation z_1 of multiple sheets as follows:

$$(2 \cdot n) \cdot z_1 + n \cdot z_2 = z \tag{4.27}$$

Then, according to the Newton-Raphson method (Figure 4.5) again, the following equation can be obtained:

$$\begin{cases} F(z_2) = 2 \cdot n \cdot \sqrt[3]{\dfrac{16 \cdot (R_A)^3 \cdot \sqrt{B_0 + B_1 \cdot z_2 - B_2 \cdot (z_2)^2} \cdot z_2}{A_0 \cdot (d_{thickness} - 4 \cdot R_A)}} + n \cdot z_2 - z = 0 \\ z_2(i+1) = z_2(i) - \dfrac{F(z_2(i))}{F'(z_2(i))} \end{cases} \tag{4.28}$$

The calculation method for multiple sheets is the same as one sheet. For a given total deformation value z, the surface deformation value z_1 can be calculated.

4.4.2 Calculation results of multiple sheets

The relationship between z_1 and z of multiple sheets can be calculated (see Appendix A5) according to different curve fitting methods (Equations 4.29 and 4.30):

$$z_1 = c_1 \cdot z + c_2 \tag{4.29}$$

On one hand, if the relationship between surface deformation z_1 and total deformation z is described by using the linear curve fitting method (Equation 4.29), their coefficients (c_1 and c_2) can be calculated and listed in Table 4.4.

Table 4.4: Coefficients for showing the relationship between the surface deformation z_1 and the total deformation z, which are calculated by using the linear curve fitting method (see Appendix A8). The coefficient of determination (R^2) of each fitting curve is also provided.

Number of sheets	c_1	c_2	Coefficient of determination (R^2)
1	3.6×10^{-1}	1.0×10^{-3}	0.994
4	1.0×10^{-1}	3.7×10^{-4}	0.997
8	5.1×10^{-2}	3.7×10^{-4}	0.997
12	3.5×10^{-2}	2.7×10^{-4}	0.998
16	2.7×10^{-2}	2.2×10^{-4}	0.998
20	2.2×10^{-2}	1.7×10^{-4}	0.998
24	1.8×10^{-2}	2.1×10^{-4}	0.998
32	1.4×10^{-2}	1.5×10^{-4}	0.998
48	9.3×10^{-3}	1.4×10^{-4}	0.998

72	6.1×10^{-3}	1.6×10^{-4}	0.998
80	5.3×10^{-3}	2.3×10^{-4}	0.998
90	4.8×10^{-3}	1.9×10^{-4}	0.998
100	4.4×10^{-3}	1.8×10^{-4}	0.998
110	4.0×10^{-3}	1.2×10^{-4}	0.999
120	3.7×10^{-3}	1.2×10^{-4}	0.999
130	3.4×10^{-3}	1.4×10^{-4}	0.999
140	3.2×10^{-3}	1.5×10^{-4}	0.998
150	2.9×10^{-3}	1.8×10^{-4}	0.998
160	2.7×10^{-3}	1.7×10^{-4}	0.998

According to the results obtained above, by substituting Equation 4.29 into Equation 4.4, the force-deformation relationship of multiple sheets can be calculated (Equation 4.30).

$$F = \frac{E(z_1)\cdot A_0 \cdot z_1^{\,3}}{8\cdot(R_A)^3} = \frac{E\cdot A_0 \cdot (c_1 \cdot z + c_2)^3}{8\cdot(R_A)^3} \tag{4.30}$$

The calculation results of the force-formation behavior of multiple sheets (sheet numbers are between 1 and 160) are shown in the following pictures (program code see Appendix A11):

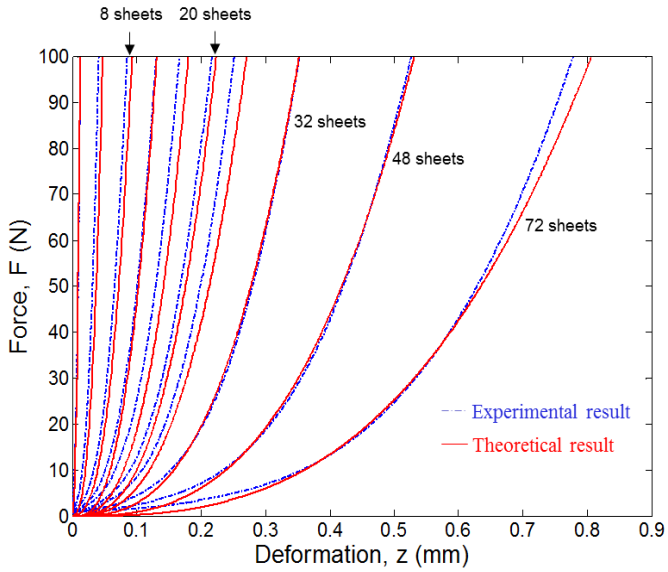

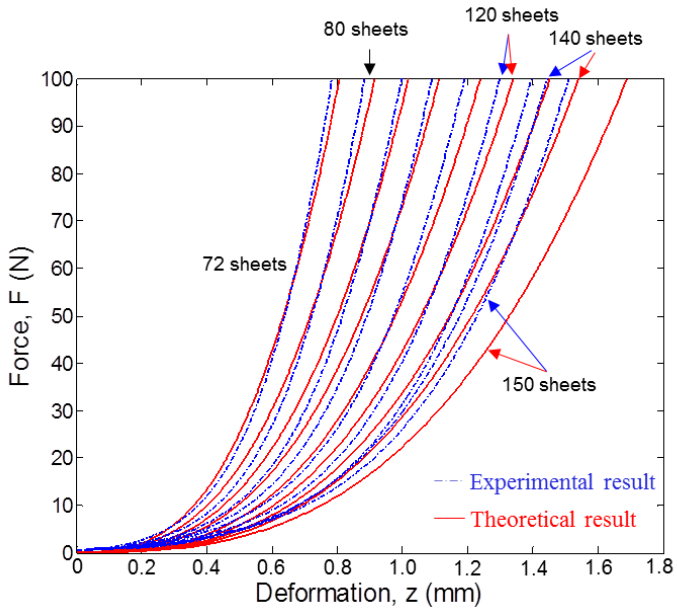

Figure 4.12: Comparisons between the experimental and theoretical force-deformation curves of multiple sheets. The picture above shows the comparisons under 72 sheets, the picture below shows the comparisons of 72 to 150 sheets. The blue curves are the experimental force-deformation data (see Figure 2.5 (b)). The red curves are calculated by using the theoretical model, in which the relationship between z_1 and z is calculated by using the linear curve fitting method (program code see Appendix A11).

In Figure 4.12, the results of the force-deformation behavior of multiple sheets show that when the sheet number are 32 and 48, the experimental results fit the theoretical results very well. When the sheet number is bigger than 130, the deviation increases dramatically.

On the other hand, the relationships between z_1 and z of multiple sheets can also be described by using the 3th degree polynomial functions (cubic curve fitting):

$$z_1 = b_1 \cdot z^3 + b_2 \cdot z^2 + b_3 \cdot z + b_4 \tag{4.31}$$

The coefficients b_i (i=1,…4) for different sheets can be calculated, the calculation results of these coefficients are listed in Table 4.5.

Table 4.5: Coefficients for showing the relationship between the surface deformation z_1 and the total deformation z by using the cubic curve fitting (see Appendix A8). The coefficient of determination (R^2) of each cubic fitting curve is also provided. When R^2 = 1.000 means the fitting curve goes through all the original data.

Number of sheets	b_1	b_2	b_3	b_4	Coefficient of determination (R^2)
1	$1.7\times10^{+1}$	-3.1×10^{-1}	4.9×10^{-1}	1.6×10^{-5}	1.000

4	5.5×10^{-1}	-2.6×10^{-1}	1.3×10^{-1}	-1.3×10^{-5}	1.000
8	6.9×10^{-2}	-6.4×10^{-2}	6.3×10^{-2}	-1.3×10^{-5}	1.000
12	1.0×10^{-2}	-2.5×10^{-2}	4.2×10^{-2}	-9.8×10^{-6}	1.000
16	4.6×10^{-3}	-1.4×10^{-2}	3.1×10^{-2}	-1.0×10^{-5}	1.000
20	4.0×10^{-3}	-9.9×10^{-3}	2.5×10^{-2}	-1.2×10^{-5}	1.000
24	7.0×10^{-3}	-1.0×10^{-2}	2.1×10^{-2}	-4.9×10^{-6}	1.000
32	6.8×10^{-4}	-4.1×10^{-3}	1.6×10^{-2}	-9.9×10^{-6}	1.000
48	4.9×10^{-4}	-2.2×10^{-3}	1.1×10^{-2}	-9.4×10^{-6}	1.000
72	4.7×10^{-4}	-1.5×10^{-3}	7.3×10^{-3}	-7.6×10^{-6}	1.000
80	3.5×10^{-5}	-5.5×10^{-4}	6.2×10^{-3}	-8.8×10^{-6}	1.000
90	1.1×10^{-4}	6.7×10^{-4}	5.7×10^{-3}	-2.1×10^{-5}	1.000
100	-6.0×10^{-5}	-5.0×10^{-4}	5.1×10^{-3}	-2.6×10^{-6}	1.000
110	-2.3×10^{-18}	-2.7×10^{-4}	4.5×10^{-3}	-9.0×10^{-6}	1.000
120	-1.7×10^{-5}	-2.2×10^{-4}	4.2×10^{-3}	-4.9×10^{-6}	1.000
130	6.7×10^{-5}	-4.3×10^{-4}	4.0×10^{-3}	-2.7×10^{-5}	1.000
140	6.0×10^{-5}	-3.9×10^{-4}	3.8×10^{-3}	-1.9×10^{-5}	1.000
150	2.6×10^{-5}	-2.7×10^{-4}	3.5×10^{-3}	-1.9×10^{-5}	1.000
160	3.9×10^{-5}	-1.5×10^{-4}	3.1×10^{-3}	-1.7×10^{-5}	1.000

The same as the method of linear curve fitting, the equations (Equation 4.31) derived above can be substituted into Equation 4.4. After that, the force-deformation curves of multiple sheets can be derived as Equation 4.32 (see Appendix A11).

$$F=\frac{E(z_1)\cdot A_0\cdot z_1^{\,3}}{8\cdot(R_A)^3}=\frac{E\cdot A_0\cdot\left(b_1\cdot z^3+b_2\cdot z^2+b_3\cdot z+b_4\right)^3}{8\cdot(R_A)^3} \tag{4.32}$$

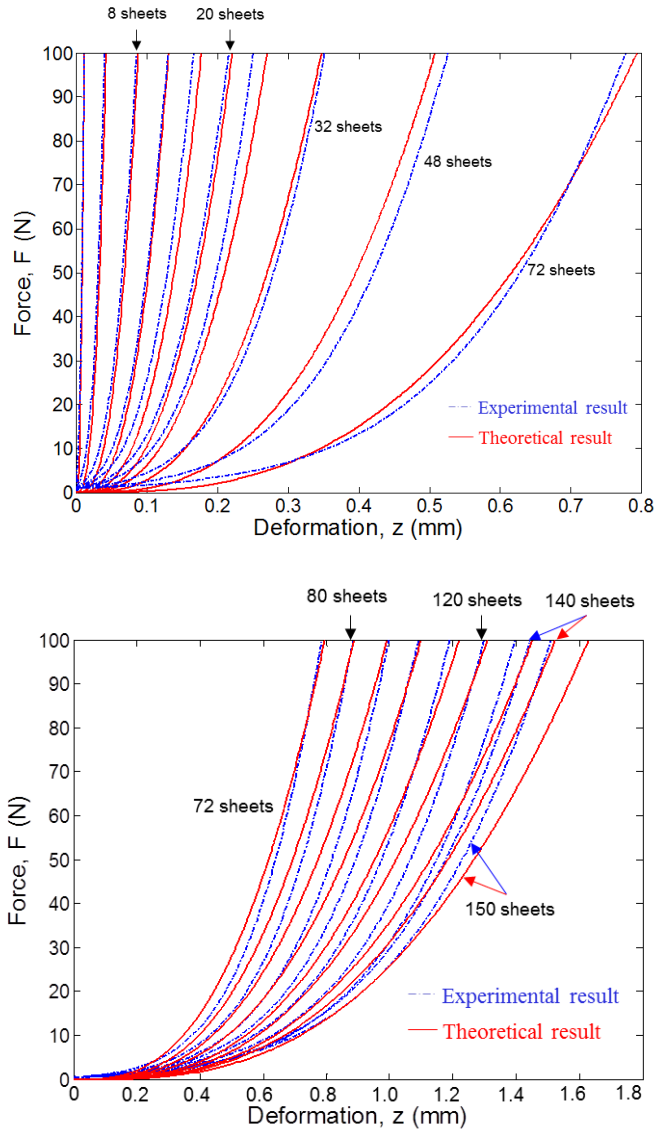

Figure 4.13: Comparisons between the experimental and theoretical force-deformation curves of multiple sheets. The picture above shows the comparisons under 72 sheets, the picture below shows the comparisons of 72 to 150 sheets. The blue curves are the experimental force-deformation data (see Figure 2.5 (b)). The red curves are calculated by using the theoretical model, in which the relationship between z_1 and z is calculated by using the cubic curve fitting method (program code see Appendix A11).

It can be seen from Figure 4.13 that the theoretical curves of multiple sheets are very close to the experimental curves. In order to show the feasibility of the proposed model, the deformations of paper stacks under some different forces (25 N, 50 N, 75 N and 100 N) were calculated and compared with the experimental results. The deviation between the theoretical and experimental results under the maximum force (100 N) was taken as an example and shown in Table 4.6.

Table 4.6: Deviations of the total deformation z between experimental results and theoretical results under the force of 100 N. Two different curve fitting methods (linear and cubic) are used for calculating the relationship between z_1 and z.

Number of sheets	Experimental result (mm)	Theoretical result			
		Linear (mm)	Deviation (%)	Cubic (mm)	Deviation (%)
1	0.012	0.011	8.300	0.011	8.300
4	0.042	0.047	11.900	0.043	2.380
8	0.085	0.092	8.240	0.088	3.530
12	0.130	0.137	5.380	0.131	0.770
16	0.167	0.180	7.780	0.178	6.590
20	0.216	0.223	3.240	0.221	2.310
24	0.251	0.271	7.970	0.270	7.570
32	0.352	0.352	0.000	0.347	1.420
48	0.527	0.531	0.760	0.508	3.610
72	0.784	0.806	2.810	0.794	1.280
80	0.884	0.915	3.510	0.886	0.230
90	0.998	1.019	2.100	0.992	0.600
100	1.090	1.113	2.110	1.099	0.830
110	1.190	1.240	4.200	1.220	2.520
120	1.299	1.340	3.160	1.309	0.770
130	1.397	1.453	4.010	1.452	3.940
140	1.444	1.540	6.650	1.524	5.540
150	1.510	1.689	11.850	1.629	7.880
160	1.582	1.818	14.920	1.723	8.910

According to the results listed in Table 4.6, the distribution of the deviations under 100 N is shown in Figure 4.14 (d). For other forces (25 N, 50 N and 75 N), the distributions of the deviations were also provided in Figure 4.14 as figures (a), (b) and (c).

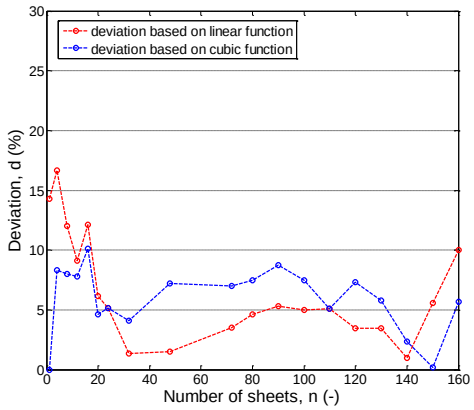

(a) Deviations when the force is 25 N.

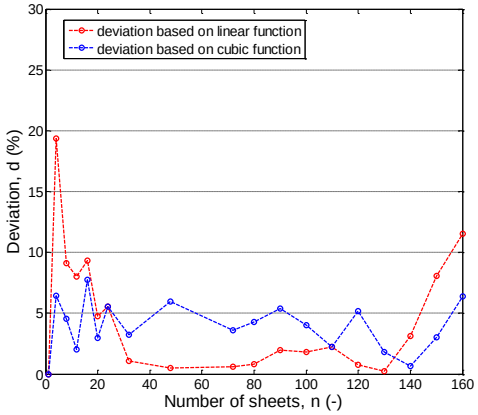

(b) Deviations when the force is 50 N.

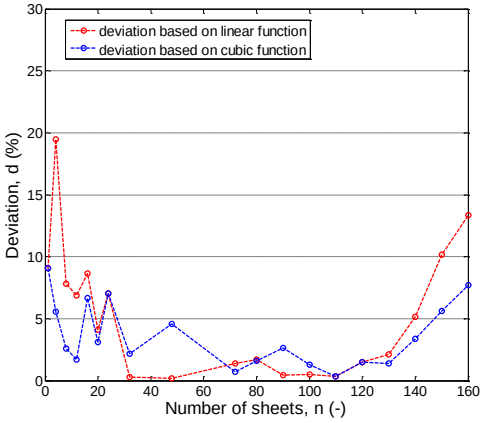

(c) Deviations when the force is 75 N.

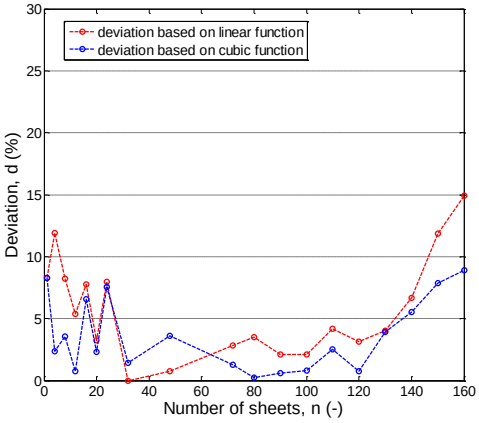

(d) Deviations when the force is 100 N.

Figure 4.14: Deviations between the theoretical and experimental results. The pictures (a), (b), (c) and (d) show the deviations under different forces (25 N, 50 N, 75 N and 100 N), respectively. The red dashed curves in these pictures are the deviations calculated based on the results in Figure 4.12, the blue dashed curves in these pictures are the deviations calculated according to Figure 4.13.

According to Figure 4.14, the red dashed curves show the distribution of the deviations based on the linear functions (Equation 4.29), the big deviations mainly exists in a small number of sheets (when the number is smaller than 20 sheets) and a big number of sheets (when the number is bigger than 140 sheets).

The deviation results based on cubic functions (Figure 4.13) are similar to the deviations based on linear functions (Figure 4.12). Big deviations mainly exists in small and big number of sheets. From Figure 14 (a), (b) and (c), it is clear that when the sheet number is between 20

and 140, the deviations based on cubic functions are bigger than the deviation based on linear functions. Otherwise (when the sheet number is smaller than 20 or bigger than 140), the deviations based on cubic functions are smaller than the deviations based on linear functions.

Figure 14 (a) also shows that when the force is 25 N, the deviations based on cubic functions (blue dashed line between 20 to 140 sheets) are bigger than the deviations under other forces (50 N, 75 N and 100 N).

To sum up, the equations (Equations 4.30 and 4.32) drived according to the new theoretical model can be well used for calculating the force-deformation behavior of paper stacks. Especially, when the number is between 20 and 140 sheets, the results based on linear functions are much more precise. When the sheet numbers are smaller than 20 or bigger than 140, the results based on cubic functions are much more precise.

As described in Section 2.1.5, when the sheet number is less than 20 sheets, the deviations are main because of the heterogeneous density of paper generated in the papermaking process. These deviations can be decreased by doing much more tests and using the average force-deformation curves.

4.4.3 Some further discussion about multiple sheets

For multiple sheets, the total deformation can be seperated into three parts (Schaffrath, 1993, Schaffrath and Göttsching, 1992a): the deformation of the paper surfaces in contact with a stiff material (indenter or platform), the deformation of the internal paper structure and the deformation of the paper surfaces in contact with each other. According to the model proposed in this paper, the difference between the paper-paper contact and indenter-paper contact was ignored. If the difference is taken into account, the different components of the total deformation can be calculated. When the number of sheets is n, the number of the indenter-paper contact pair is 2 (indenter-papercontact and platform-paper contact), the number of the internal structure is n and the number of the paper-paper contact pair is n-1. The values of each part are listed in Table 4.7.

Table 4.7: Percentages of different parts of deformation under the force of 100 N, in which the deformation of the paper is divided into three parts: the deformation of the indenter-paper contact, the internal deformation and the deformation of the paper-paper contact. z_4 is the average paper-paper contact deformation. z^n (n=1, …, n) is the total deformation of n sheets under 100 N.

Total deformation	Indenter-paper contact deformation	Internal deformation	Paper-paper contact deformation
1 sheet z^1	$2 \cdot z_1$	z_2	0

2 sheets z^2	$2 \cdot z_1$	$2 \cdot z_2$	z_4
3 sheets z^3	$2 \cdot z_1$	$3 \cdot z_2$	$2 \cdot z_4$
4 sheets z^4	$2 \cdot z_1$	$4 \cdot z_2$	$3 \cdot z_4$
…	…	…	…
n sheets z^n	$2 \cdot z_1$	$n \cdot z_2$	$(n-1) \cdot z_4$

For one sheet, when the force is 100 N, the total deformation is z = 0.0125 mm, the deformation of the surface is z_1 = 0.0057 mm and the deformation of the internal structure is z_2 = 0.0011 mm. For multiple sheets, when the imposed force is 100 N, the values of z_1 and z_2 are the same as for one sheet.

So, according to Table 4.7, the following equations can be developed:

$$z^n = 2 \cdot z_1 + n \cdot z_2 + (n-1) \cdot z_4 \tag{4.33}$$

$$z_4 = \frac{z^n - 2 \cdot z_1 - n \cdot z_2}{n-1} \tag{4.34}$$

When the sheet numbers change from 1 to 160, the calculated deformation results of each part are listed in Table 4.8.

Table 4.8: Calculation results of the different deformations (the indenter-paper contact deformation, the internal deformation, the total paper-paper contact deformation and the average paper-paper contact deformation) under the force of 100 N. z_4 is the average paper-paper contact deformation.

Number of sheets n	Total deformation of n sheets z^n (mm)	Indenter-paper contact deformation $2 \cdot z_1$ (mm)	Internal deformation $n \cdot z_2$ (mm)	Total paper-paper contact deformation $(n-1) \cdot z_4$ (mm)	Average paper-paper contact deformation z_4 (mm)
1	0.0125	0.0114	0.0011	0.0000	0.0000
2	0.0195	0.0114	0.0022	0.0059	0.0059
4	0.0406	0.0114	0.0044	0.0248	0.0083
8	0.0855	0.0114	0.0088	0.0653	0.0093

12	0.1299	0.0114	0.0132	0.1053	0.0096
16	0.1666	0.0114	0.0176	0.1376	0.0092
20	0.2164	0.0114	0.0220	0.1830	0.0096
24	0.2512	0.0114	0.0264	0.2133	0.0093
32	0.3523	0.0114	0.0352	0.3057	0.0099
48	0.5267	0.0114	0.0528	0.4624	0.0098
72	0.7780	0.0114	0.0792	0.6874	0.0097
80	0.8840	0.0114	0.0880	0.7846	0.0099
100	1.0905	0.0114	0.1100	0.9690	0.0098
120	1.2990	0.0114	0.1320	1.1555	0.0097
140	1.4442	0.0114	0.1540	1.2788	0.0092
160	1.5823	0.0114	0.1760	1.3948	0.0088

According to the table above, the percentage of each contact part occupied in the total deformation is plotted in Figure 4.15.

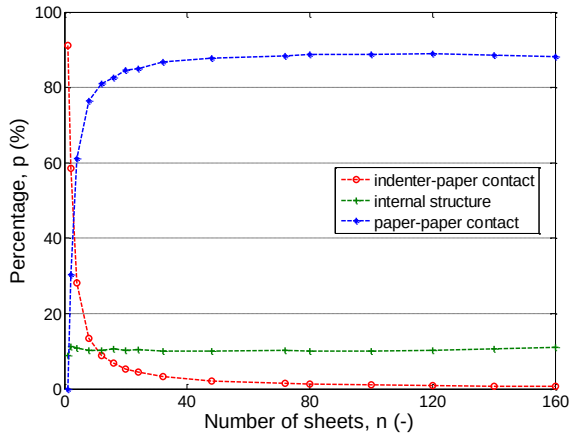

Figure 4.15: Percentages of indenter-paper contact deformation, internal deformation and paper-paper contact deformation, which are changing with the number of sheets. The red dashed curve shows the changing of the indenter-paper contact, the blue dashed curve shows the changing of the paper-paper contact and the green dashed curve shows the changing of the internal structure (see Appendix A12).

The average deformation of each paper-paper contact pair can also be calculated, the result is shown in the following figure.

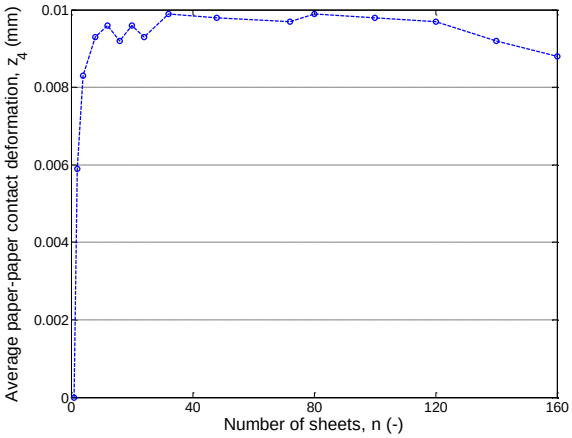

Figure 4.16: Average deformation of each paper-paper contact pair when the number sheets increasing from 1 sheet to 160 sheets.

It can be seen that, the average deformation of each paper-paper contact pair is changing with the increasing of sheets number, especially when the number is smaller than 20 sheets or bigger than 140 sheets, which is in accordance with the deviation of the force-deformation relationship obtained before.

4.5 Summary

The force-deformation behavior of paper and paper stacks in the out-of-plane direction was investigated. Two main aspects of mechanical behavior of paper and paper stacks were completed, which can be summarized as follows:

Firstly, the relationship between surface deformation and total deformation was calculated and compared by using linear and cubic curve fitting methods. The comparisons between the experimental results and the calculation results show that both linear and cubic curve fitting methods can be used for the proposed theoretical model.

Secondly, the force-deformation model of one sheet can be extended to calculate the force-deformation behavior of paper stacks. The verification results show that this model can be well used, especially, when the number is between 20 and 140 sheets.

For this theoretical model, the parameters (as shown in Table 4.1) needed for calculating the force-deformation behavior of paper or paper stacks are less than ten, compared with the constitutive models, all of these parameters are much easier to be measured. But in the following chapter, a much easier way for building the model for multiple sheets will be proposed.

5 Descriptive model for paper and paper stacks

The main purpose of this chapter is to establish a suitable mathematical model for actualizing the description of the compression curve for paper and paper stacks. Without considering the paper structure, the loading and unloading nonlinearities of J-shaped stress-strain relations can be approximated by using different equations. The first section (Section 5.1) of this chapter makes a summary of some of the relevant researches about building the models for describing the J-shaped curves. In Section 5.2, based on the model proposed by Takaki (Takaki and Fukuoka, 2000), both of the descriptive models for one sheet and multiple sheets will be established. According to the model built in Section 5.2, all the coefficients used for determining the functions are expressed as the functions of the stress at the start point of unloading. After that, the normal copy paper will be taken as an example to show the methods of calculating these coefficients in Section 5.3. Section 5.4 compares the results between calculation and experiments, the comparative analysis of the results demonstrates the effectiveness of the descriptive model. Finally, a concluding discussion of these models is given in Section 5.5.

5.1 Studies of the descriptive model of J-shaped curve

The stress-strain curve of paper consists of two parts: the curve under loading condition and the curve under unloading condition. Because of the plasticity of the paper material, the analysis of the unloading curve is much more complicated than the loading curve, but anyway, both of the loading and unloading curves can be described by using curve fitting methods. Generally, the descriptive models for J-shaped materials can be divided into linear and nonlinear models.

For the compression behavior of gasket material, Nagata et al. (Nagata et al., 2002) proposed a simplified linear model, in which the nonlinearity of the gasket stress-strain relation was approximated by two elastic moduli in loading and unloading stages, respectively. The comparison of computing results between the simplified linear model and the nonlinear model was also provided. For the analysis of gasket stress distribution in bolted flange joints, the result of this simplified model gives a good agreement with the result of nonlinear model.

The material behavior of paper in the out-of-plane direction can also be modeled with two linear springs (as shown in Figure 5.1), which provides convenient analysis of processes such as paper delivery and paper calendering (Eckstein, 2014, Eckstein and Hagedorn, 2014).

As it has been introduced before, a characteristic equation in exponential form for paper stack was proposed by Pfeiffer (Pfeiffer, 1981), in this paper, both of the stress-strain curves in

loading and unloading stages were expressed by using exponential functions with coefficients of K_1 and K_2.

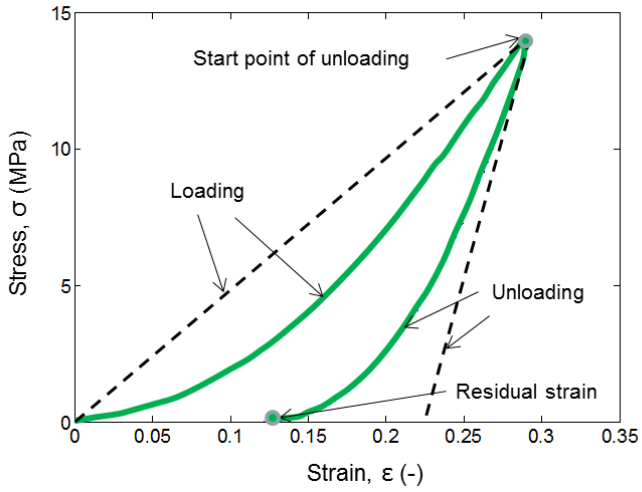

Figure 5.1: Typical stress-strain curve of paper. The black dotted line is the simplified linear stress-strain curve of paper modelled with two elastic springs, the green line is the original stress-strain curve.

In the presented work of Katta (Katta and Rasmuson, 2008), the average loading J-shaped stress-strain curve of the product particles was fitted to an exponential nonlinear equation, which contains P_1, P_2, P_3 and P_4, four parameters.

When measuring vicker hardness of metal, the indenter is designed as a standard pyramid shape, the load–depth curve of the material is J-shaped. In the paper of Gubiza (Gubicza, 1997), the load-depth functions in the loading and unloading periods were described by using two different quadratic equations.

As mentioned in the previous sections, the compressive curve of paper material is a typical example of materials with J-shaped stress-strain curves. A mathematical descriptive model for spiral wound gasket was proposed by Takaki (Takaki and Fukuoka, 2000), then the stress-strain relation for asbestos sheet gasket was proposed (Takaki and Fkuoka, 2001) in the same way. After that, these models were widely used for calculating the stress-strain curve of gasket materials (Fukuoka et al., 2007, Fukuoka et al., 2012, Fukuoka and Takaki, 2003, Nagata et al., 2002, Takaki and Fukuoka, 2002a, Takaki and Fukuoka, 2002b, Takaki and Fukuoka, 2003), especially, for the FEM calculation of gasket materials.

5.2 Numerical analysis

Takaki's model of a single sheet was used in the following sections for establishing the descriptive model for paper stacks. The loading curve of paper will be calculated by using the

sextic polynomial equation and the unloading curve will be described by using the modified exponential function. Then, based on the assumption that when the force is the same, the deformation of the paper stack is directly proportional to the number of sheets, the descriptive model of multiple sheets will also be established.

5.2.1 Takaki's model of a single sheet

According to the model proposed by Takaki (Takaki and Fukuoka, 2000), the stress-strain curve of spiral wound gasket in the loading stage can be described by using the sextic polynomial function:

$$\sigma = a_0 + a_1\varepsilon + a_2\varepsilon^2 + a_3\varepsilon^3 + a_4\varepsilon^4 + a_5\varepsilon^5 + a_6\varepsilon^6 = \sum_{i=0}^{6}\left[a_i \cdot \varepsilon^i\right] \tag{5.1}$$

Where σ and ε are the paper stress and strain. a_i (i=0, …, 6) are the constant values for identifying the polynomial function. Before the loading stage, a preload is put on the specimen. So, the corresponding value of a_0 is not 0. The above equation provides a good approximation for the stress-strain relationship in the loading condition.

For the unloading curve, the stress-strain relationship can be described by using the modified exponential function, the idea of constructing the model is to ensure that the established equation goes through the residual point (ε_r, 0):

$$\sigma = \alpha \cdot \exp\left(\beta \cdot \varepsilon\right) - \alpha \cdot \exp\left(\beta \cdot \varepsilon_r\right) \tag{5.2}$$

Where:

$$\begin{cases} \beta = f_1\left(\varepsilon_y\right) = p_1 + q_1 \cdot \varepsilon_y + r_1 \cdot \left(\varepsilon_y\right)^{1/3} \\ \varepsilon_r = f_2\left(\varepsilon_y\right) = p_2 \cdot \varepsilon_y + q_2 \\ \alpha = f_3\left(\varepsilon_y\right) = \dfrac{\sigma_y}{\exp\left(\beta \cdot \varepsilon_y\right) - \exp\left(\beta \cdot \varepsilon_r\right)} \end{cases} \tag{5.3}$$

In Equations 5.2 and 5.3 σ is the dependent variable and ε is the independent variable. The unloading curve is determined by the coefficients α and β. σ_y and ε_y are the values of stress and strain at the start point of unloading. The value of σ_y can be calculated according to Equation 5.1. p_1, q_1 and r_1 are the constants for identifying the relationship between β and ε_y. p_2 and q_2 are the components of the equation between ε_r and ε_y. All of the coefficients α, β and ε_r can be expressed as a function of the independent variable ε_y.

5.2.2 New descriptive model of multiple sheets

Furthermore, the relationship between force and deformation can be converted from the stress-strain relation by using the following equations:

$$\begin{cases} F = \sigma \cdot \pi \cdot \left(\frac{d_{diameter}}{2} \right)^2 \\ z = \varepsilon \cdot d_{thickness} \end{cases} \tag{5.4}$$

Where F is the force imposed on the paper specimen, z is the deformation of paper under the corresponding force F. $d_{diameter}$ is the diameter of the cylindrical indenter. $d_{thickness}$ is the average thickness of the paper. The functions of stress σ are shown in Equation 5.1 and 5.2, the strain $\varepsilon = z / d_{thickness}$.

The force-deformation relation of one sheet can be divided into two parts: the loading force-deformation relation ($F^1_{loading}$-$z^1_{loading}$) and the unloading force-deformation relation ($F^1_{unloading}$-$z^1_{unloading}$). According to Equations 5.1, 5.2 and 5.4, the force-deformation relations of paper in the loading and unloading stages can be expressed as:

$$\begin{cases} F^1_{loading} = \left\{ \sum_{i=0}^{6} \left[a_i \cdot \left(\frac{z^1_{loading}}{d_{thickness}} \right)^i \right] \right\} \cdot \pi \cdot \left(\frac{d_{diameter}}{2} \right)^2 \\ F^1_{unloading} = \left\{ \alpha \cdot \exp\left[\beta \cdot \left(\frac{z^1_{unloading}}{d_{thickness}} \right) \right] - \alpha \cdot \exp\left(\beta \cdot \varepsilon_r \right) \right\} \cdot \pi \cdot \left(\frac{d_{diameter}}{2} \right)^2 \end{cases} \tag{5.5}$$

in which, $F^1_{loading}$ and $F^1_{unloading}$ are the forces in the loading and unloading stages, respectively. $z^1_{loading}$ and $z^1_{unloading}$ are the corresponding deformations. The superscript 1 in variables $F^1_{loading}$, $F^1_{unloading}$, $z^1_{loading}$ and $z^1_{unloading}$ means the number of sheets is 1.

For multiple sheets, it is assumed that when the force is the same, the deformations of the paper stacks ($z^n_{loading}$ and $z^n_{unloading}$) are directly proportional to the number of sheets (n). On the basis of this assumption, the force-deformation relation can be expressed as:

$$\begin{cases} z^n_{loading} = k_{loading} \cdot n \\ z^n_{unloading} = k_{unloading} \cdot n \end{cases} \tag{5.6}$$

In Equation 5.6, $k_{loading}$ and $k_{unloading}$ are the slopes in the loading and unloading conditions, respectively, which are used for showing the relationship between deformation and number of paper sheets.

The values of $k_{loading}$ and $k_{unloading}$ depend on the independent variable forces. When force changes, the values of $k_{loading}$ and $k_{unloading}$ will also change. The relationship between the slope and force can be expressed as the following equations:

$$\begin{cases} k_{loading} = f\left(F^1_{loading}\right) \\ k_{unloading} = f\left(F^1_{unloading}\right) \end{cases} \tag{5.7}$$

According to Equations 5.6 and 5.7, the force-deformation relation model of one sheet derived in Equation 5.5 can be extended to multiple sheets:

$$\begin{cases} loading: \\ \quad \begin{cases} z^n_{loading} = f\left(F^1_{loading}\right)\cdot n \\ F^n_{loading} = F^1_{loading} \end{cases} \\ unloading: \\ \quad \begin{cases} z^n_{unloading} = f\left(F^1_{unloading}\right)\cdot n \\ F^n_{unloading} = F^1_{unloading} \end{cases} \end{cases} \tag{5.8}$$

Where, $F^n_{loading}$ and $F^n_{unloading}$ are the forces applied to paper stack in the loading and unloading condition, respectively. $z^n_{loading}$ and $z^n_{unloading}$ are the corresponding deformations. For a better understanding, the force-deformation relation of multiple sheets can also be expressed as the converse equation of Equation 5.9:

$$\begin{cases} loading: \\ \quad F^n_{loading} = f^{-1}\left(\dfrac{z^n_{loading}}{n}\right) \\ unloading: \\ \quad F^n_{unloading} = f^{-1}\left(\dfrac{z^n_{unloading}}{n}\right) \end{cases} \tag{5.9}$$

In the following sections, the normal copy paper (copy paper, DIN A4, 210×297 mm, 80 g/m^2), produced by the Steinbeis Paper GmbH will be taken as an example for showing the practicability of the proposed model. All the relationships between different coefficients mentioned in the above equations will be derived. After that, the final descriptive model of the normal copy paper will be proposed. The results between the calculation and experiment will also be compared.

5.3 Coefficients relationship

For the loading stage of one sheet, the stress-strain curve can be described by using the curve fitting method, by which, a set of experimental force-deformation data (the setup is shown in Figure 2.3, an example of the experimental data is shown in Figure 2.11) is needed. With the aid of Matlab (MATLAB, 2013), the constants a_i (i = 0, …, 6) which are used for identifying the loading curve of paper can be calculated automatically according to Equation 5.1. The function and all coefficients of constants a_i (i = 0, …, 6) are shown in Figure 5.2.

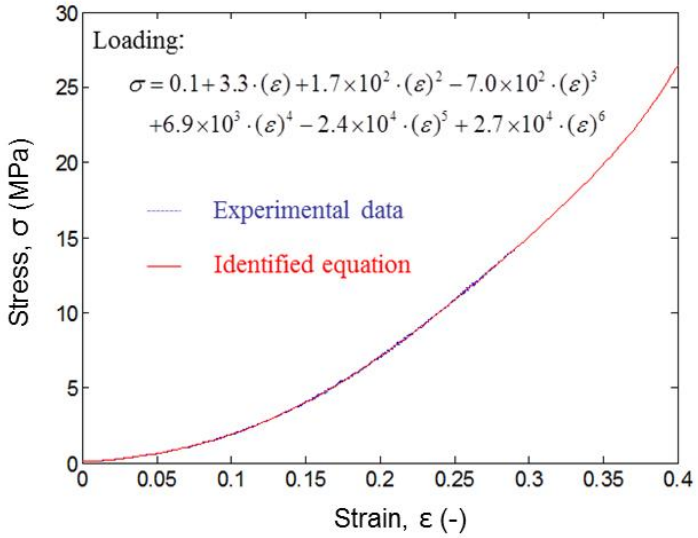

Figure 5.2: Stress-strain curve of paper on the loading condition. The blue curve is the experimental curve, the red one is the fitting curve by using the polynomial function (Equation 5.1). The coefficient of determination: R^2 = 1.0.

As shown in Figure 5.2, the stress-strain curve under any desired strain can be obtained by the following identified equation.

$$\sigma = 0.1 + 3.3\cdot(\varepsilon) + 1.7\times10^{2}\cdot(\varepsilon)^{2} - 7.0\times10^{2}\cdot(\varepsilon)^{3} + 6.9\times10^{3}\cdot(\varepsilon)^{4} - 2.4\times10^{4}\cdot(\varepsilon)^{5} + 2.7\times10^{4}\cdot(\varepsilon)^{6} \qquad (5.10)$$

From Figure 5.2, it can be seen that the stress-strain curve of paper in the loading stage can be perfectly described by using the polynomial function (Equation 5.1).

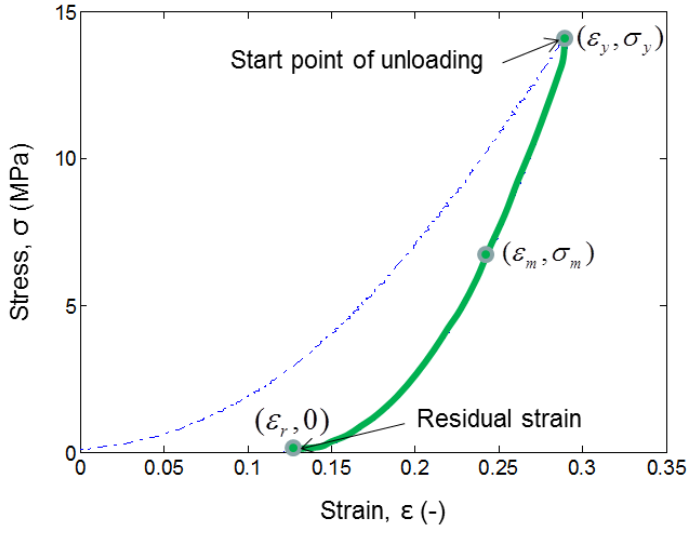

Figure 5.3: Selected points in the unloading stress-strain curve for calculating the components of the unloading function.

For the unloading stage, the model is built according to Equations 5.2 and 5.3. There are three unknown variables, α, β and ε_r. Different values of ε_r under different forces can be directly obtained from the experimental data. Two more groups of points, (ε_y, σ_y) and (ε_m, σ_m), are selected for calculating the coefficients α and β.

As shown in Figure 5.3, ε_y and σ_y are the strain, stress values at the start point of unloading. (ε_r, 0) represents the residual strain point. (ε_m, σ_m) is a random point selected in the unloading curve. With the help of these points, the values of α and β can be calculated.

5.3.1 Relationship between β and ε_y

In Equation 5.2, there are 3 unknown variables (α, β and ε_r), three groups of points are needed for calculating the values of α and β. For instance, when the maximum force applied on the paper is 80 N, the value of ε_r can be obtained from the experiments (part of the experimental data can be collected from Figure 2.12). Then, the value of β can be calculated by combining the values at the start point of unloading (ε_y, σ_y) and the random point (ε_m, σ_m). The final calculation result of β under 80 N is 35.73. Other values of β can be calculated as the same way and the results are listed in Table 5.1.

Table 5.1: Values of ε_y and β under different forces. Part of the experimental data are collected according to Figure 2.12.

Force (N)	ε_y (-)	β (-)
20	0.0502	64.52
40	0.0880	43.03
80	0.1222	35.73
120	0.1547	25.97
200	0.2019	22.04
400	0.2904	14.36

According to the data obtained in Table 5.1, it can be observed that the values of β are decreasing with the increasing of ε_y values, these discrete points have been plotted in the following coordinates. The value of ε_y is regarded as the abscissa. The value of β is regarded as the ordinate.

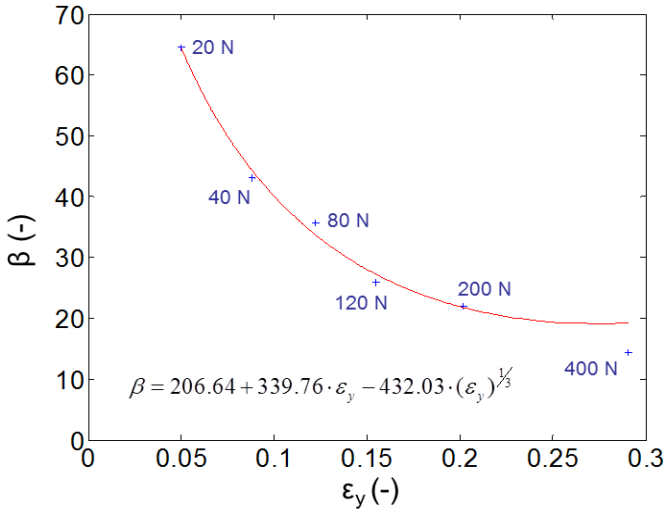

Fig 5.4: Relationship between the coefficients β and ε_y. The discrete points are the points listed in Table 5.1. The red curve is calculated by using the curve fitting method, on the basis of Equation 5.3 (see $f_1(\varepsilon_y)$). The coefficient of determination: $R^2 = 0.994$.

As shown in Figure 5.4, the coefficient β is regarded as a dependent variable, which changes with the independent variable ε_y, the relation between them (see Equation 5.3) can be expressed by the following function:

$$\beta = f_1(\varepsilon_y) = 206.64 + 339.76 \cdot \varepsilon_y - 432.03 \cdot (\varepsilon_y)^{1/3} \tag{5.11}$$

The function above consists of two parts: a linear polynomial function and a radical function. Here, the coefficients provided in Equation 5.3 are: $p_1 = 206.64$, $q_1 = 339.76$ and $r_1 = 432.03$. The coefficient of determination: $R^2 = 0.994$. This function can also be expressed by using other functions, for example, the exponential function. The comparison between them will be implemented in the discussion chapter.

5.3.2 Relationship between ε_r and ε_y

As mentioned previously, (ε_y, σ_y) represents the start point of unloading. (ε_r, 0) is the residual strain point. The values of ε_y and ε_r can be directly obtained according to the experimental data (Part of the experimental data are collected according to Figure 2.12.). The values of them under different forces are listed in Table 5.2.

Table 5.2: Values of ε_y and ε_r under different forces, which have been obtained according to the experimental results. Part of the experimental data are collected according to Figure 2.12.

Force (N)	ε_y (-)	ε_r (-)
20	0.0502	0.0024

40	0.0880	0.0159
80	0.1222	0.0272
120	0.1547	0.0460
200	0.2019	0.0756
400	0.2904	0.1216

On the basis of the data listed in Table 5.2, it can be seen that the values of ε_r are increasing with the increasing of ε_y values, these discrete points were plotted in Figure 5.5. The value of ε_y and ε_r are regarded as the abscissa and ordinate, respectively.

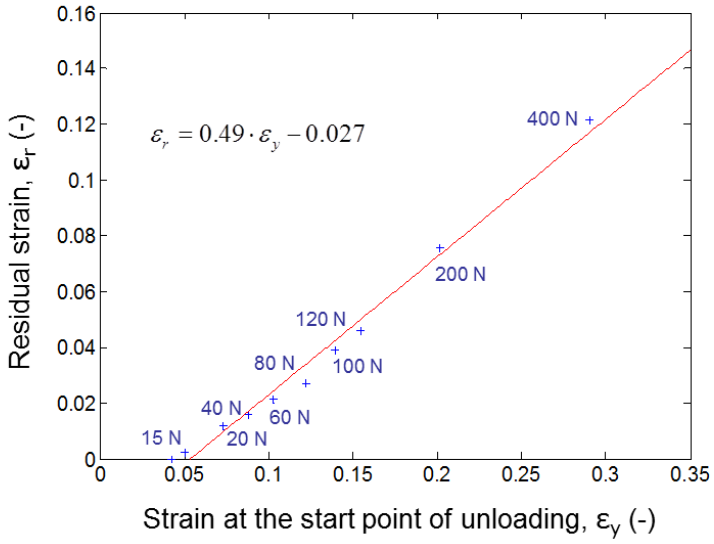

Figure 5.5: Relationship between the maximum strain and the residual strain. The red curve is calculated by using the linear curve fitting method, on the basis of Equation 5.3 (see $f_2(\varepsilon_y)$). The coefficient of determination: $R^2 = 0.990$.

From Figure 5.5, it can be seen that the relationship between ε_r and ε_y is linear. By using the linear curve fitting method, the relationship between residual strain ε_r and the corresponding unloading strain ε_y can be expressed as:

$$\varepsilon_r = f_2\left(\varepsilon_y\right) = 0.49 \cdot \varepsilon_y - 0.027 \tag{5.12}$$

The coefficients of linear relation proposed in Equation 5.3 are: $p_2 = 0.49$, $q_2 = -0.027$. The coefficient of determination: $R^2 = 0.990$.

5.3.3 Relationship between α and ε_y

According to Equation 5.3 ($f_3(\varepsilon_y)$), the value of α is determined by the values of β and ε_r, the value of β can be calculated by using Equation 5.11, the value of ε_r is expressed as Equation 5.12. The final function of α can be expressed as follows:

$$\alpha = f_3(\varepsilon_y) = \frac{\sigma_y}{\exp(\beta \cdot \varepsilon_y) - \exp(\beta \cdot \varepsilon_r)} \tag{5.13}$$

Where,

$$\begin{cases} \varepsilon_r = f_2(\varepsilon_y) = 0.49 \cdot \varepsilon_y - 0.027 \\ \beta = f_1(\varepsilon_y) = 206.64 + 339.76 \cdot \varepsilon_y - 432.03 \cdot (\varepsilon_y)^{1/3} \end{cases} \tag{5.14}$$

5.3.4 Relationship between $k_{loading}$ and $F_{loading}$

For multiple sheets, the descriptive model was constructed on the assumption that when the force is the same, the deformations of paper stacks ($z^n_{loading}$ and $z^n_{unloading}$) are proportional to the number of sheets n. This hypothesis was verified by the experimental data.

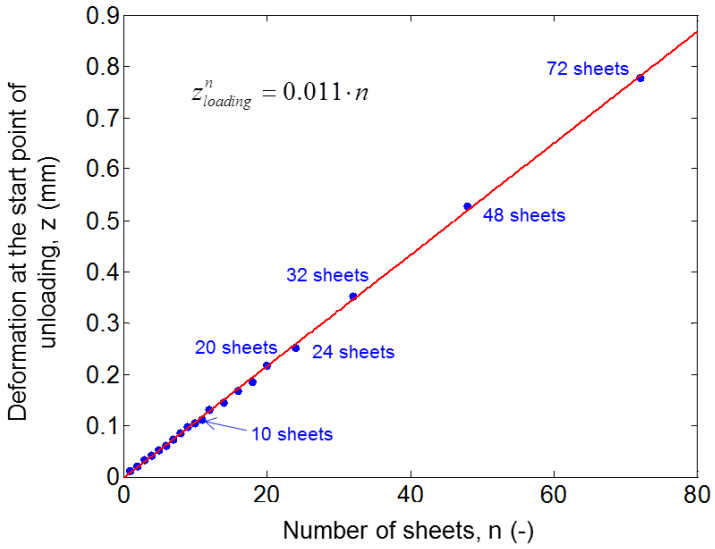

Figure 5.6: Deformations of different paper stacks under the same force. The red curve is the linear curve fitting result, on the basis of Equation 5.6. The force applied here is 100 N.

It can be seen from Figure 5.6 that, when the force is 100 N, the deformations (strains) of paper stacks at the start points of unloading (see Figure 5.3 (ε_y, σ_y)) show a perfectly linear relationship with the sheet numbers. For other forces, the experimental results are shown in Figure 5.7, these curves indicate linear relationship between deformation and sheet number.

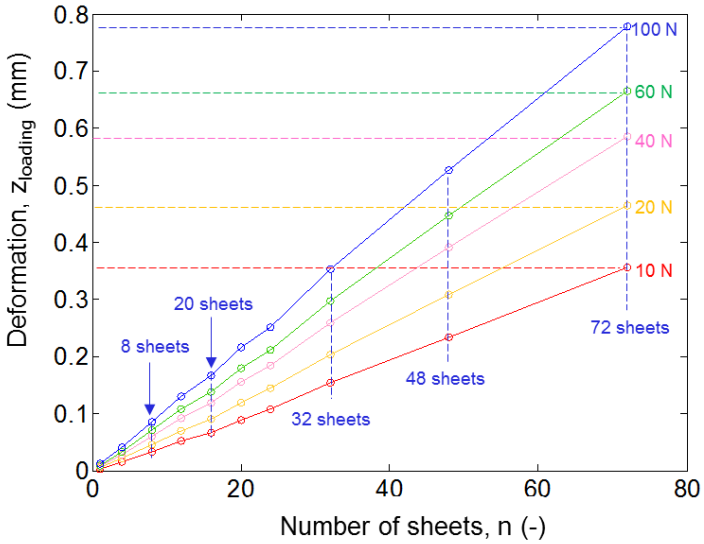

Figure 5.7: Experimental deformation of paper stacks under different loading forces. The red curve shows the deformation of paper stacks when the force is 10 N, the blue curve shows the deformations of the paper stacks under 100 N. The deformation data are collected from Figure 2.5 (b).

For different numbers of sheets, the statistical deformation value under different forces has been plotted in Figure 5.7, from which we can see the linear relationship between deformation and sheet number under different forces. The values of the slopes $k_{loading}$ can be calculated by using the linear curve fitting method (the same method as shown in Figure 5.6) and the values of forces $F_{loading}$ and slopes $k_{loading}$ are listed in Table 5.3.

Table 5.3: Values of $k_{loading}$ under different loading forces, calculated by using the linear curve fitting method according to Figure 5.7.

$F_{loading}$ (N)	$k_{loading}$ (-)
5	0.0036
10	0.0050
20	0.0065
40	0.0082
60	0.0093
80	0.0100
100	0.0110

According to the listed slope values ($k_{loading}$) in Table 5.3, the values of slopes and forces were plotted in the same coordinate system, the value of $F_{loading}$ is regarded as the abscissa. The value of $k_{loading}$ is regarded as the ordinate. Then the values of the slopes can be expressed as the function of forces.

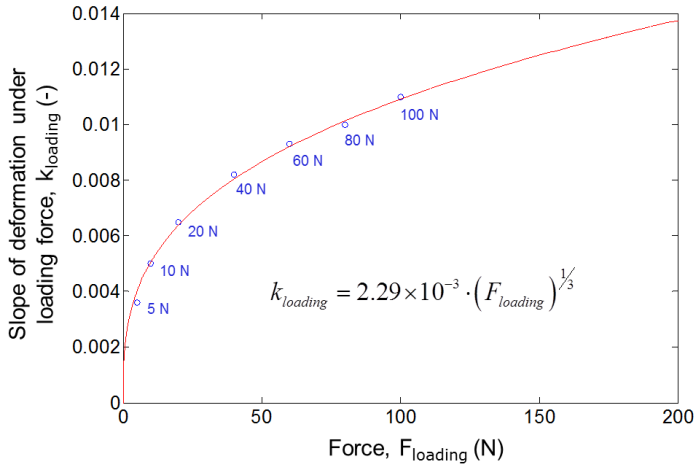

Figure 5.8: Relationship between the slopes and the forces in the loading condition. The discrete blue points are the experimental values of $k_{loading}$ under different forces, which are provided in Table 5.3. The red curve is the approximation curve, on the basis of Equation 5.8. The coefficient of determination: $R^2 = 0.997$.

Figure 5.8 displays that the value of $k_{loading}$ is changing with the force. The relationship between them can be approximated by using different functions. A radical function was used here for describing the relationship between slope and force. The coefficient of the function can be calculated by using the curve fitting method.

$$z^n_{loading} = f\left(F^n_{loading}\right)\cdot n = \left[2.29\times10^{-3}\cdot\left(F^n_{loading}\right)^{1/3}\right]\cdot n \qquad (5.15)$$

The coefficient of determination: $R^2 = 0.997$.

5.3.5 Relationship between $k_{unloading}$ and $F_{unloading}$

The same as the loading stage, for different forces, the slopes in the unloading stage are also constant values, which can be seen in Figure 5.9. However, because of the plasticity of the paper materials, a part of the deformation of paper in the unloading stage cannot be recovered to the original shape, which is a non-reversible change of shape in response to applied force. The non-recoverable part shown in the force-deformation curve is called the residual deformation. The corresponding strain shown in the stress-strain curve is called the residual strain, which is shown in Figure 5.1 and Figure 5.3. Thus, in the unloading stage, when the force is decreasing to 0 N, the deformation of paper stacks cannot recover to 0 mm. But for simplifying the model, the influence from the residual deformation is ignored.

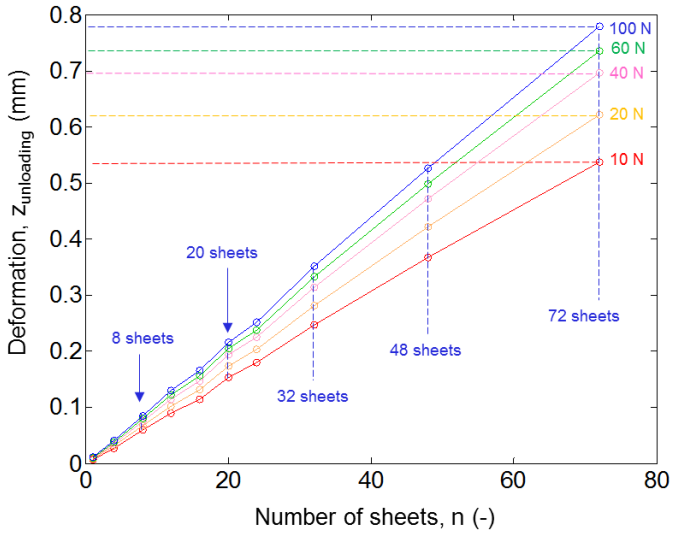

Figure 5.9: Experimental deformation of paper stacks under different unloading forces. The red curve shows the deformation of paper stacks when the force is 10 N, the blue curve shows the deformation of paper stacks when the force is 100N. The deformation data are collected from Figure 2.5 (b).

And the same, for different sheets, when the force is the same, the total deformation is directly proportional to the number of sheets. The values of the slopes $k_{unloading}$ under different forces $F_{unloading}$ are calculated by using the linear curve fitting method and the results are shown in Table 5.4.

Table 5.4: Values of $k_{unloading}$ under different unloading forces, calculated by using the linear curve fitting method according to Figure 5.9.

$F_{unloading}$ (N)	$k_{unloading}$ (-)
5	0.0063
10	0.0076
20	0.0087
40	0.0098
60	0.0010
80	0.0110
100	0.0110

According to the listed slope values ($k_{unloading}$) in Table 5.4, the values of slopes and forces are plotted in the same coordinate system, the values of $F_{unloading}$ and $k_{unloading}$ are regarded as the horizontal and ordinate axis, respectively. By using the curve fitting method, the values of the slopes can be expressed as the function of forces.

The relation between $k_{unloading}$ and $F_{unloading}$ can be approximated according to the obtained function in Figure 5.10. The coefficients of the function are calculated by using the curve fitting method. Two radical functions are used for describing the relationship between slope and force. As mentioned above, the influence of the residual deformation is ignored, the values of the slopes are regarded as changing from 0.

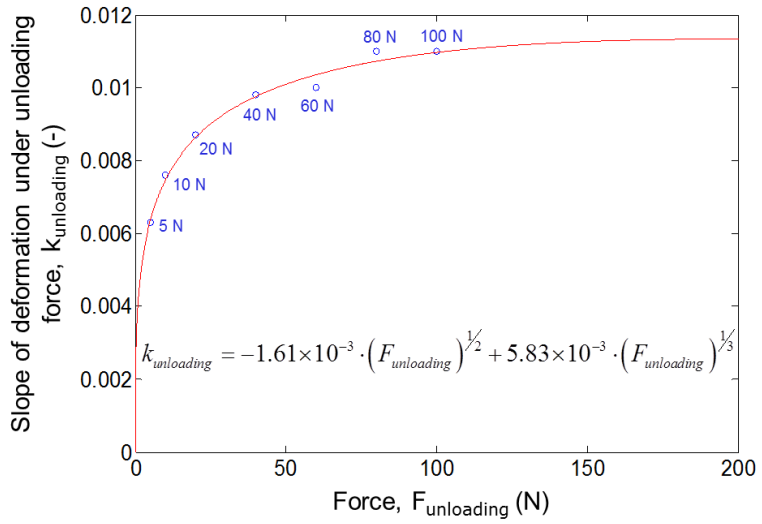

Figure 5.10 Relationship between the slopes and the forces in the unloading condition. The discrete blue points are the values of $k_{unloading}$ under $F_{unloading}$ provided in Table 5.4. The red curve is the fitting curve, on the basis of Equation 5.8. The coefficient of determination: $R^2 = 0.988$.

The function of the unloading deformation can be expressed as:

$$z^n_{unloading} = f\left(F^n_{unloading}\right)\cdot n = \left[-1.61\times10^{-3}\cdot\left(F^n_{unloading}\right)^{1/2} + 5.83\times10^{-3}\cdot\left(F^n_{unloading}\right)^{1/3}\right]\cdot n \qquad (5.16)$$

The coefficient of determination: $R^2 = 0.988$.

Then, on the basis of the relationships between different coefficients calculated in Section 5.3, the descriptive model of the normal copy paper can be derived.

5.4 Calculation results

According to the descriptive models proposed in Section 5.2 and the relationships between different coefficients calculated in Section 5.3, the final descriptive models of a single sheet as

well as paper stacks can be derived. In this section, the stress-strain curve of a single sheet and the force-deformation curves of multiple sheets will also be calculated and compared with the experimental results.

5.4.1 Final descriptive model of the normal copy paper

According to Equations 5.1-5.3 and 5.10-5.14, the descriptive model of normal copy paper for calculating the stress-strain relation of one sheet can be expressed as follows:

$$\begin{cases} loading: \\ \quad \sigma = a_0 + a_1\varepsilon + a_2\varepsilon^2 + a_3\varepsilon^3 + a_4\varepsilon^4 + a_5\varepsilon^5 + a_6\varepsilon^6 \\ unloading: \\ \quad \sigma = \alpha \cdot \exp(\beta \cdot \varepsilon) - \alpha \cdot \exp(\beta \cdot \varepsilon_r) \end{cases} \tag{5.17}$$

Where:

$$\begin{cases} \sigma_y = 0.1 + 3.3 \cdot (\varepsilon_y) + 1.7\times10^2 \cdot (\varepsilon_y)^2 - 7.0\times10^2 \cdot (\varepsilon_y)^3 \\ \quad +6.9\times10^3 \cdot (\varepsilon_y)^4 - 2.4\times10^4 \cdot (\varepsilon_y)^5 + 2.7\times10^4 \cdot (\varepsilon_y)^6 \\ \varepsilon_r = 0.49 \cdot \varepsilon_y - 0.027 \\ \beta = 206.64 + 339.76 \cdot \varepsilon_y - 432.03 \cdot (\varepsilon_y)^{1/3} \\ \alpha = \dfrac{\sigma_y}{\exp(\beta \cdot \varepsilon_y) - \exp(\beta \cdot \varepsilon_r)} \end{cases} \tag{5.18}$$

According to Equations 5.4-5.9 and 5.15, 5.16, the force-deformation relation of paper stacks can be expressed as the following descriptive model:

$$\begin{cases} loading: \\ \quad F^n_{loading} = f^{-1}\left(\dfrac{z^n_{loading}}{n}\right) \\ unloading: \\ \quad F^n_{unloading} = f^{-1}\left(\dfrac{z^n_{unloading}}{n}\right) \end{cases} \tag{5.19}$$

Where:

$$\begin{cases} f\left(F^n_{loading}\right) = 2.29\times10^{-3} \cdot \left(F^n_{loading}\right)^{1/3} \\ f\left(F^n_{unloading}\right) = -1.61\times10^{-3} \cdot \left(F^n_{unloading}\right)^{1/2} + 5.83\times10^{-3} \cdot \left(F^n_{unloading}\right)^{1/3} \end{cases} \tag{5.20}$$

Based on the models proposed above, the stress-strain curve of a single sheet and the force-deformation curves of multiple sheets will also be calculated and compared with the experimental results.

5.4.2 Comparisons between the experimental and calculated results

In order to verify the applicability of the proposed model, some experiments of a single sheet by using different maximum compression forces were performed, their results are shown in Figure 5.11. In the experimental process, the provided maximum forces are 20 N, 60 N, 80 N and 120 N. Part of the experimental data are shown in Figure 2.12.

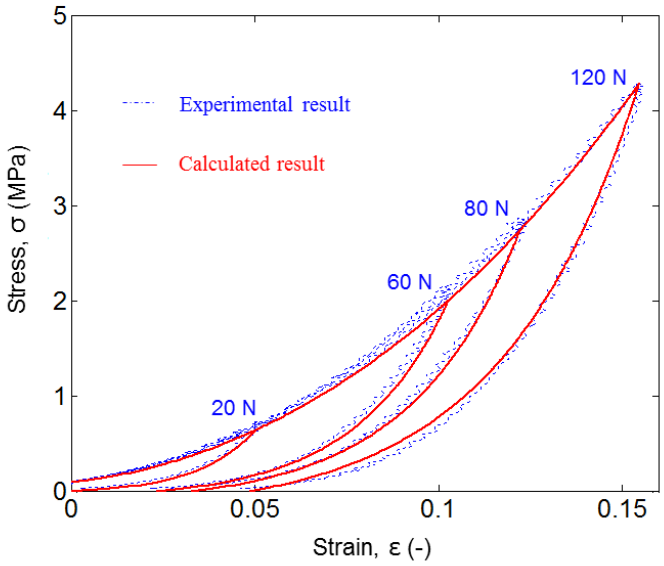

Figure 5.11: Comparisons between the experimental and calculated stress-strain curves of one sheet. The blue curves are the experimental results, part of which are shown in Figure 2.12. The red curves are calculated by using the descriptive model. According to the size of the indenter, the corresponding values of forces at the start point of unloading are also provided in this figure. A pressure of 3.5 MPa corresponds to about 100 N.

Figure 5.11 shows the stress-strain curves of paper stacks calculated by using the descriptive model. The experimental results and the calculated results based on the descriptive model fit fairly well. The results show that the proposed descriptive model (Equation 5.17) is capable of capturing the stress-strain behavior of paper at any desired strains.

For multiple sheets, the force-deformation curves can be calculated according to Equations 5.19 and 5.20. The experimental data of the force-deformation curves are plotted in Figure 2.5 (b). Figure 5.12 shows the calculated force-deformation curves of multiple sheets (1, 4, 8, 12, 16, 20, 24, 32, 48 and 72 sheets) with a maximum force of 100 N.

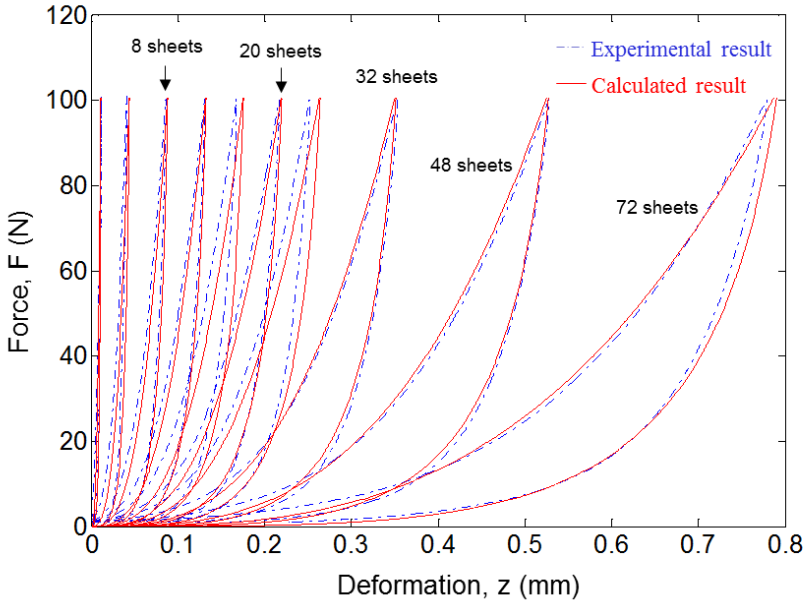

Figure 5.12: Comparisons between the experimental and calculated force-deformation curves of multiple sheets. The blue curves are the experimental force-deformation data (see Figure 2.5). The red curves were calculated by using the descriptive model (see Appendix A13).

The comparisons between the experimental results and the calculated results are shown in Figure 5.12. The deformations of the paper stacks under the maximum force (100 N) were selected for calculating the deviations.

The deviations between the experimental and calculated results are defined as: the absolute value of the experimental result minus the calculated results and then divided by the experimental result.

The results of the deformations and the deviations at the start points of unloading (the points under the maximum force) are listed in Table 5.5.

Table 5.5: Comparisons of the force-deformation curves of paper stacks between the experimental results (see Figure 2.5 (b)) and calculated results (based on the descriptive model), which are the deformations at the start point of unloading.

Number of sheets	Deformation at the start point of unloading (mm)		Deviation (%)
	Experimental result	Calculated result	
1	0.012	0.014	16.67
4	0.042	0.044	5.00

8	0.085	0.087	2.35
12	0.130	0.131	0.76
16	0.167	0.175	4.79
20	0.216	0.219	1.39
24	0.251	0.262	4.38
32	0.352	0.350	0.57
48	0.527	0.525	0.38
72	0.778	0.787	1.16

The deviations between the experimental results and the calculated results based on the descriptive model (calculated result) are shown in Table 5.5. It can be seen that the deviation of one sheet is very big (16.67%). For other sheets, the deviations are smaller than 5.00%, the results of the descriptive model give good fits to the experimental results. The deviations of multiple sheets between the experimental and calculated results will be further discussed in Section 5.5.3.

5.5 Discussion

For one sheet, the loading stage can be described by using not only the polynomial function, but also the exponential function. The comparisons between them will be discussed in Section 5.5.1. For multiple sheets, the force-deformation curves of more sheets (72 sheets to 160 sheets) will be calculated and compared with the experimental results.

5.5.1 Influence of the different loading functions

In the previous section, the stress-strain curve of paper in the loading stage was described by using the sextic polynomial function (see Equation 5.1). But the stress-strain relation of a single sheet can also be described by using some other functions, such as the modified exponential function shown below (see Equation 5.21).

$$\sigma = p_3 \cdot \{\exp(q_3 \cdot \varepsilon) - 1\} \tag{5.21}$$

Where, p_3 and q_3 are the coefficients for determining the loading exponential function, which can be calculated by using the curve fitting method.

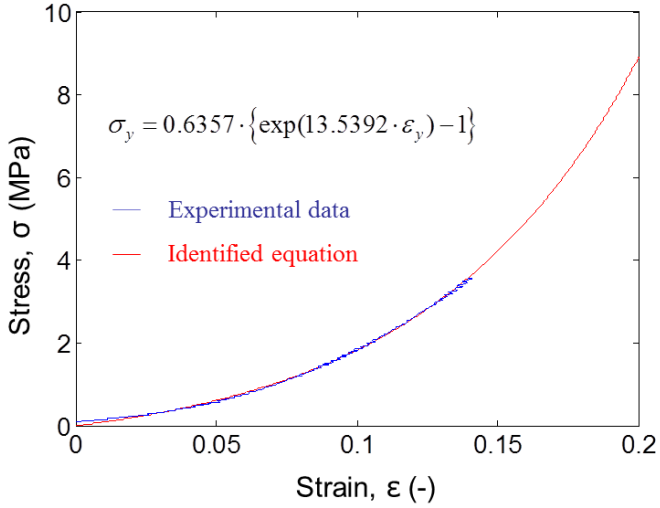

Figure 5.13: Stress - strain curve of paper in the loading stage. The blue curve is the stress-strain calculated based on the experimental result (see Figure 2.5 (a)). The red curve is calculated by using the exponential function. The coefficient of determination: $R^2 = 0.998$.

The fitting result of copy paper is shown below. The coefficient of determination: $R^2 = 0.998$.

$$\sigma_y = 0.6357 \cdot \{\exp(13.5392 \cdot \varepsilon_y) - 1\} \tag{5.22}$$

In additional, the relationship between the coefficient β and unloading strain ε_y (Equation 5.11) in the descriptive model of copy paper (Equation 5.18) can also be replaced by the exponential function (Equation 5.23).

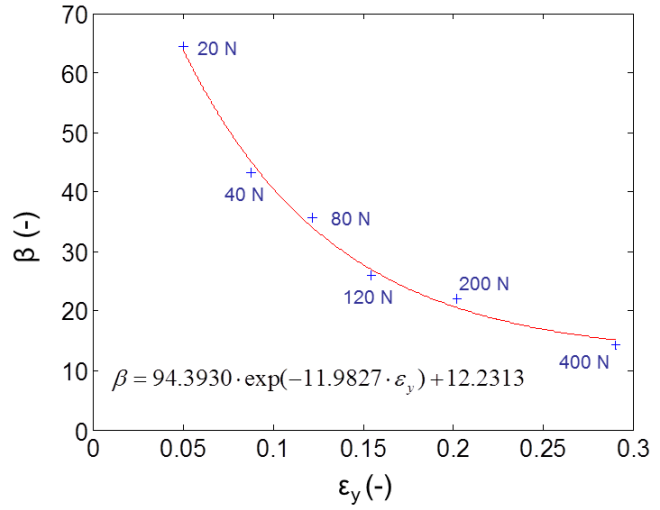

Figure 5.14: Relationship between the coefficients β and ε_y. The discrete points are the points listed in Table 5.1, the red curve is calculated by using the curve fitting method.

The new function for β can be expressed as:

$$\beta = p_4 \cdot \exp\left(q_4 \cdot \varepsilon_y\right) + r_4 \tag{5.23}$$

Where p_4, q_4 and r_4 are the coefficients for determining the unloading exponential function, the result is shown in Equation 5.24.

$$\beta = 94.3930 \cdot \exp\left(-11.9827 \cdot \varepsilon_y\right) + 12.2313 \tag{5.24}$$

According to the new descriptive models of the coefficients (Equations 5.22 and 5.24), the stress-strain relation of a single sheet can also be expressed as Equations 5.25 and 5.26. Both of the loading curve and the coefficient β were described by using exponential functions.

$$\begin{cases} loading: \\ \quad \sigma = p_1 \cdot \{\exp(q_1 \cdot \varepsilon) - 1\} \\ unloading: \\ \quad \sigma = \alpha \cdot \exp(\beta \cdot \varepsilon) - \alpha \cdot \exp(\beta \cdot \varepsilon_r) \end{cases} \tag{5.25}$$

Where:

$$\begin{cases} \sigma_y = 0.6357 \cdot \{\exp(13.5392 \cdot \varepsilon_y) - 1\} \\ \varepsilon_r = 0.49 \cdot \varepsilon_y - 0.027 \\ \beta = 94.3930 \cdot \exp(-11.9827 \cdot \varepsilon_y) + 12.2313 \\ \alpha = \dfrac{\sigma_y}{\exp(\beta \cdot \varepsilon_y) - \exp(\beta \cdot \varepsilon_r)} \end{cases} \tag{5.26}$$

The results calculated based on the descriptive model were validated again by comparing with the experimental results.

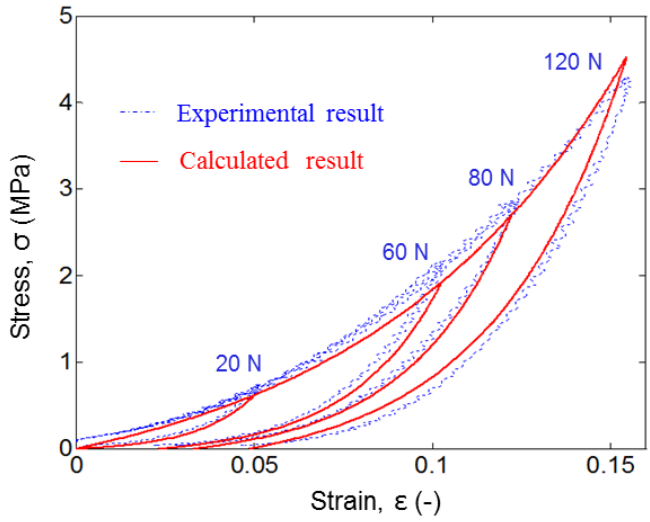

Figure 5.15: Comparisons of the stress-strain curves of paper. The blue dashed curves are the experimental results, which are measured as shown in Figure 2.12. The red curves are calculated

based on the modified descriptive model. The nominal area of the indenter is about 28.27 mm^2. A pressure of 3.5 MPa corresponds to about 100 N.

As shown in Figure 5.15, the comparison result shows that both of these two methods can be used for calculating the out-of-plane stress-strain relationship of paper materials. The calculated results based on polynomial function (Equation 5.10) and exponential functions (Equations 5.22 and 5.24) are plotted in the same figure, as shown in Figure 5.16.

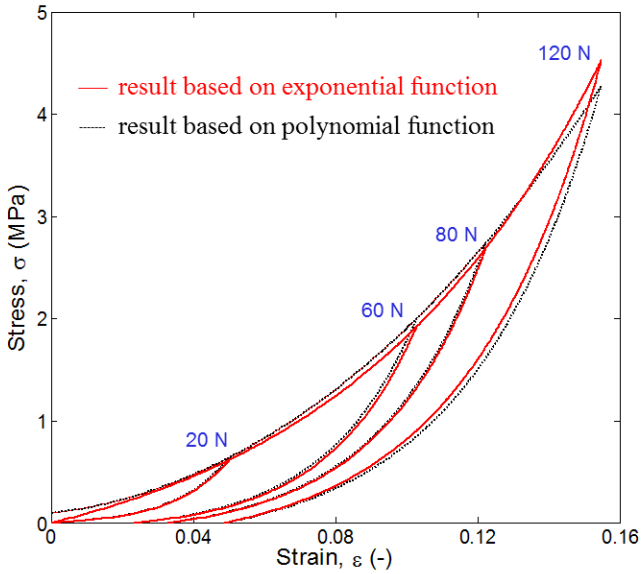

Figure 5.16: Comparisons of the results calculated based on polynomial function and exponential functions. The red curves are the results based on the exponential function (see Figure 5.15). The dashed black curves are the results based on the polynomial function, which are the red lines in Figure 5.11. The nominal area of the indenter is about 28.27 mm^2. A pressure of 3.5 MPa corresponds to about 100 N.

It can be seen from Figure 5.16 that the difference between the results calculated based on the polynomial function and the exponential function is relatively small. Both of them can be used for calculating the stress-strain curve of a single sheet. Only when the stress is bigger than 4 MPa, the difference between the two curves begins to become bigger.

5.5.2 Maximum number of sheets

The descriptive model (see Equation 5.19) can be used for calculating the force-deformation curve of multiple sheets. But the maximum number of sheets which can be calculated based on this model should be further investigated. In the following, the upper limit value of this model will be discussed. More experiments were carried out by using the ZWICK machine (see Figure 2.3) to compare with the calculated results (based on Equations 5.17 to 5.20, program code see Appendix A13). The experimental data are shown in Figure 2.5. The

numbers of sheets selected are 72, 80, 90, 100, 110, 120, 130, 140 and 150. The comparative results between the experiments and calculations are shown in Figure 5.17.

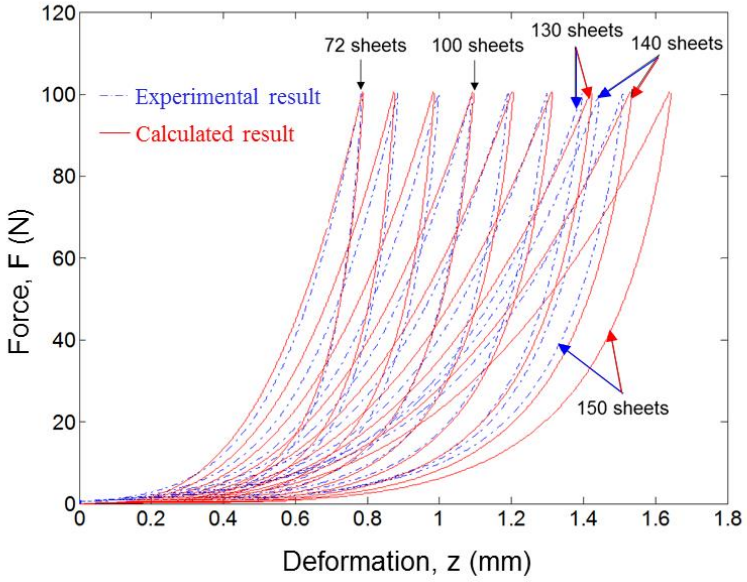

Figure 5.17: Comparisons of the experimental and calculated force-deformation curves of paper stacks. The blue curves are the experimental data (see Figure 2.5 (b)). The red curves are the force-deformation curves calculated by using the descriptive model (see Appendix A13).

Form Figure 5.17 and Table 5.6, it can be seen that when the imposed force on the paper stacks is 100 N, the maximum number of sheets which can be calculated by using this model is about 140 sheets. For more sheets, with increasing the number of sheets, the deviations are increasing. To show the difference between the calculated results and the experimental results, the deviations of the deformations at the start point of unloading were calculated. The results are listed in Table 5.6.

Table 5.6: Comparisons of the force-deformation curves of paper stacks between the experimental results and the results calculated according to the descriptive model, which are the deformations at the start point of unloading.

Number of sheets	Deformation at the start point of unloading (mm)		Deviation (%)
	Experimental result	Calculated result	
72	0.78	0.79	1.28
80	0.88	0.87	1.14
90	1.00	0.98	2.00

100	1.09	1.09	0.00
110	1.19	1.20	0.84
120	1.30	1.31	0.77
130	1.40	1.42	1.43
140	1.44	1.52	5.56
150	1.51	1.64	8.60
160	1.58	1.75	10.76

In Table 5.6, the deviations of the deformations at the start point of unloading have been calculated. According to Table 5.6, for paper stacks with amounts of less than 130, the deviations between the experimental results and the results calculated based on the descriptive model are smaller than 2.00%. But when the number of sheets is 140, the deviation is increased to about 5.56%.

5.5.3 Influence of different maximum loading forces

In Tables 5.5 and 5.6, the deviations between the calculated and experimental results under the 100 N were listed and compared, which was also plotted as the figure (d) shown in Figure 5.18.

In the loading stage, for some other maximum forces (25 N, 50 N and 75 N), the deviations between the experimental results and the results calculated based on the descriptive model were also calculated and shown in Figure 5.18 (figures (a), (b) and (c) in Figure 5.18).

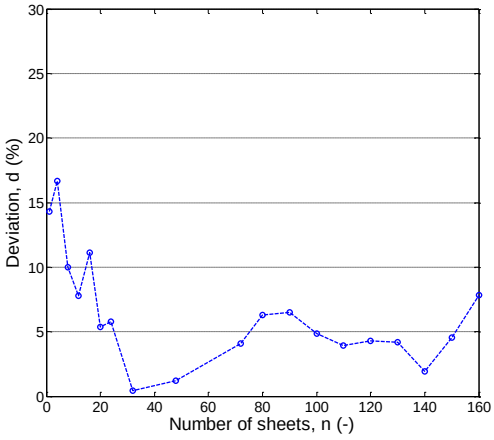

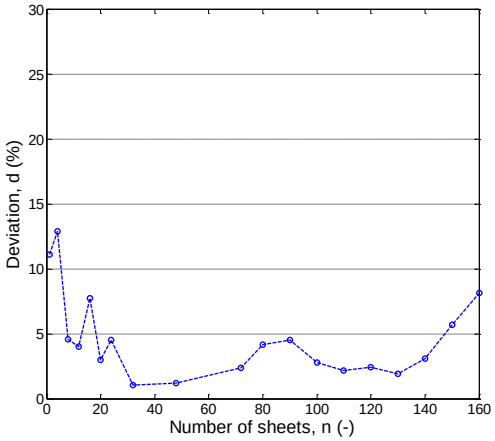

(a) Deviations when the force is 25 N.

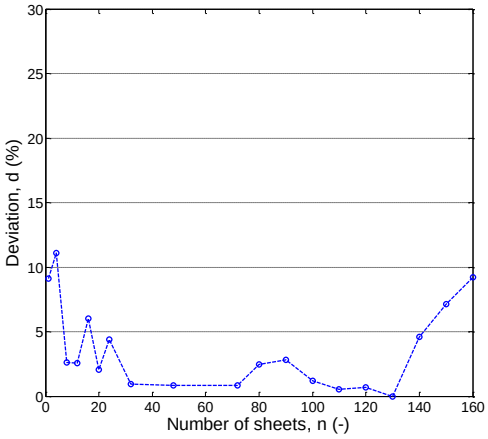

(b) Deviations when the force is 50 N.

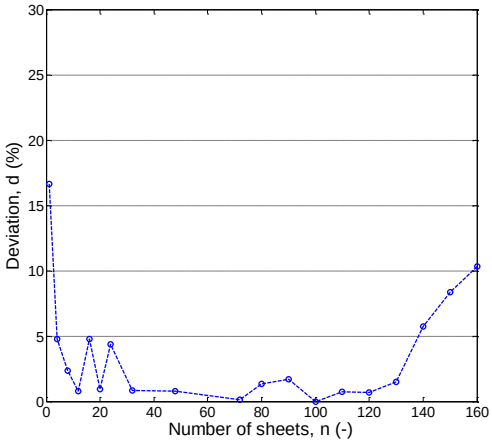

(c) Deviations when the force is 75 N.

(d) Deviations when the force is 100 N.

Figure 5.18: Deviations between the experimental results and the results calculated based on the descriptive model in the loading stage. Four pictures (a), (b), (c) and (d) are provided, which show the deviations under different forces (25 N, 50 N, 75 N and 100 N), respectively.

The distributions of the deviation between the calculated and experimental results are similar to the deviations obtained in Figure 4.14. When the sheet numbers are between 20 and 140, most of the deviations under different forces are smaller than 5.00%. Big deviations mainly exist when the numbers are smaller than 20 or bigger than 140.

In addition, Figure 5.18 clearly shows that most of the deviations under 25 N are bigger than the deviations under 50 N, the deviations under 50 N are bigger than the deviations under 75 N and also most of the deviations under 75 N are bigger than the deviations under 100 N. So, for this descriptive model, the closer the maximum force to 100 N, the smaller the deviation. Because of most of the data used in this chapter is the experiments under 100 N, so the results under the force closer to 100 N is much more precise than other situations.

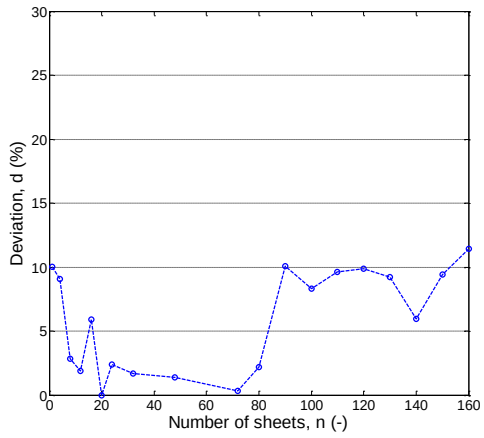

(a) Deviations when the force is 25 N.

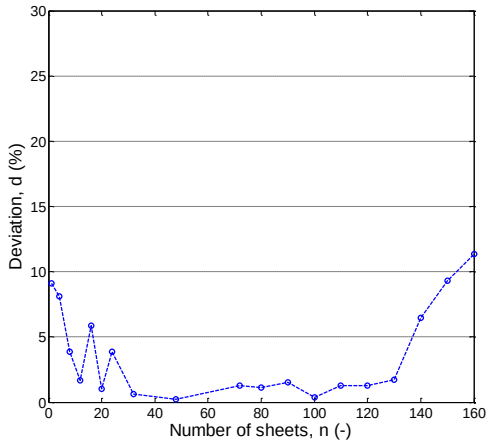

(b) Deviations when the force is 50 N.

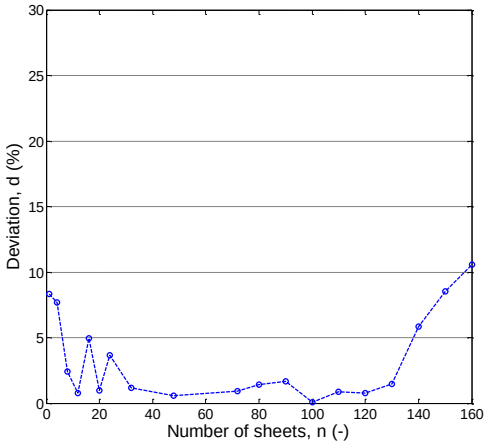

(c) Deviations when the force is 75 N.

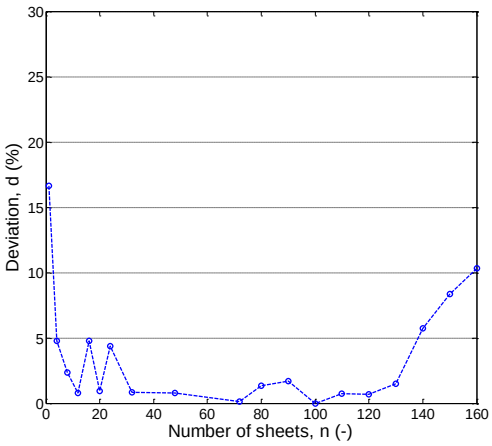

(d) Deviations when the force is 100 N.

Figure 5.19: Deviations between the experimental results and the results calculated based on the descriptive model in the unloading stage. Four pictures (a), (b), (c) and (d) are provided, which show the deviations under different maximum forces (25 N, 50 N, 75 N and 100 N), respectively.

For the unloading stage, the deviations between the calculated and experimental results under 25 N, 50 N and 75 N were also calculated, as shown in Figure 5.19.

In Figure 5.19, four pictures are provided, which show the deviations under different forces (25 N, 50 N, 75 N and 100 N), respectively. The deviations under 25 N in the unloading stage are very big, especially, when the number of sheets are 1, 4 and bigger than 90 sheets. Figures (b), (c) and (d) show that most of the deviations are smaller than 5.00%, especially, when the numbers of sheets are between 8 and 140.

The same as discussed in Sections 2.3.5 and 4.4.1, when the sheet number is less than 20 sheets, the deviation mainly comes from the density unevenness of paper generated in the papermaking process. These deviations can be decreased by doing much more tests and using the average force-deformation curves.

The surface roughness of paper was not taken into account in the proposed descriptive model, but it can be seen from the results that the hypothesis “the deformations of the paper stacks are directly proportional to the number of sheets” is correct when the number of sheets is smaller than 140.

5.6 Summary

The mechanical behavior of paper and paper stacks in the out-of-plane direction was investigated in this chapter. By using the normal copy paper, two main aspects of mechanical behavior of paper and paper stacks were completed, which can be summarized as follows:

Firstly, the stress-strain descriptive model of one sheet was established and the stress-strain curves of paper under some desired strains were obtained. The comparison results between the experimental results and the results based on the descriptive model show the practicability of this model.

Secondly, the stress-strain model of one sheet can be extended to calculate the force-deformation behavior of paper stacks. This aspect is based on the assumption of the direct relationship between the sheets number and deformation of paper stacks at same force. The verification results under different forces show that the descriptive model proposed in this chapter can be used for calculating the force-deformation behavior of paper stacks, especially, when the sheet number are between 20 and 140 sheets.

6 FEM simulation of paper by using a gasket model

In this chapter, a new simulation method for evaluating the stress-strain relationship of paper materials will be introduced. Section 6.1 summarizes the previous literatures of the paper simulation. Then, the simulation process in ANSYS and ABAQUS will be briefly introduced in Section 6.2, in which some fundamental theory about building the model in ANSYS will be introduced. In addition, some basic knowledges of defining the loading and unloading material properties will be also described. After that, the simulation of paper under different forces will be implemented.

Part of the work described in this chapter was published in (Chen et al., 2015):

Jian Chen, Jann Neumann, Hans Martin Sauer, Edgar Dörsam: *A new FEM simulation method of paper materials by using a gasket model*. 42st International Research Conference of IARIGAI, Helsinki, Finnland; 09/2015

6.1 Studies of paper simulation

Because of the complexity of the paper materials, there is still no material model provided in FEM software which can be used directly for paper simulation. Only very few references attempt to establish the simulation model in finite element (FEM) software, but even in those which did, the results remained inconclusive in some respects.

In one study, the simulations applied an orthotropic elastic-plastic constitutive model for describing the material behavior of paper. The commercial FE-code ABAQUS/Standard was adapted in the numerical analysis and the quadratic isoparametric eight-node planar stress elements used for defining the paper material (Mäkelä, 2003). In another study, a computational micromechanical material model for the unloading behavior of paper and other non-woven materials was presented (Ramasubramanian, 2007), and four-node bilinear planar stress elements were used in the ABAQUS/Standard model for simulating the uniaxial tensile test.

In 2002, a theoretical framework to account for damage in paperboard was proposed, which consists of two parts: an in-plane continuum model, and an interface model (Xia, 2002). The two models were implemented, respectively, into ABAQUS/Standard as a user-defined material (UMAT) and a user-defined interface (UINTER) for modelling the creasing and folding of paperboard (Nygards, 2005). In addition, under the supervision of Nygards, the simulation of paperboard creasing was completed and improved in a master thesis based on the model proposed by Xia (Andersson, 2006).

As mentioned in Chapter1, compared to the in-plane dimensions, the thickness of paper material is very thin. The paper is highly anisotropic with the stiffness in the in-plane direction being around 100 times larger than in the through-thickness direction (Andersson, 2006, Monica et al., 2009, Stenberg, 2002). So the in-plane stiffness and transverse shear can be negligible when compared to the stiffness in the out-of-plane direction. But unfortunately, all simulation models mentioned above are based on constitutive models, and trying to combine the in-plane and out-of-plane behavior together, which need a considerable number of free parameters to be determined through experiments. Most of these parameters are very difficult to measure.

In this Chapter, a new method of paper simulation without considering the in-plane behavior will be introduced, only the out-of-plane behavior will be taken into account. A gasket model is introduced to do the simulation of paper material.

6.2 Fundamental theory of gasket simulation

Gaskets are usually designed as very thin sheetlike structures, acting as sealing components between structural components. They are designed to provide appropriate stress-deformation behavior by virtue of their ability to adapt their thickness according to contact with a given rigid surface, so the primary deformation behavior of gasket joints is the one perpendicular to the sheet plane. As mentioned in Chapter 2, the typical force-deformation curves of most gasket materials are J-shaped, which are similar to paper materials.

There is no available model provided in ANSYS or ABAQUS which can be directly used for paper simulation, but both FEM environments offer a variety of gasket elements that generate out-of-plane behavior specifically designed for the study of gaskets. The main purpose of this chapter is to actualize the simulation of paper materials by using the gasket elements provided in the FEM software.

The principle of computer simulation of gasket material is basically the same. For gasket materials, most of the simulation processes are very similar to the simulation of other materials. Generally, the process flow of the simulation in FEM software consists of pre-processor, solution control, solve and postprocessor. The different simulation processes between ANSYS and ABAQUS are listed and compared in Figure 6.1. Both of the simulation processes in ANSYS and ABAQUS can be divided into nine steps. The principle of computer simulation of gasket material is basically the same. The simulation based on ANSYS was chosen here as an example of introducing the simulation process. For gasket materials, most of the simulation processes are very similar to the simulation of other materials. The main differences exist in the process of choosing the elements, defining the material properties and meshing.

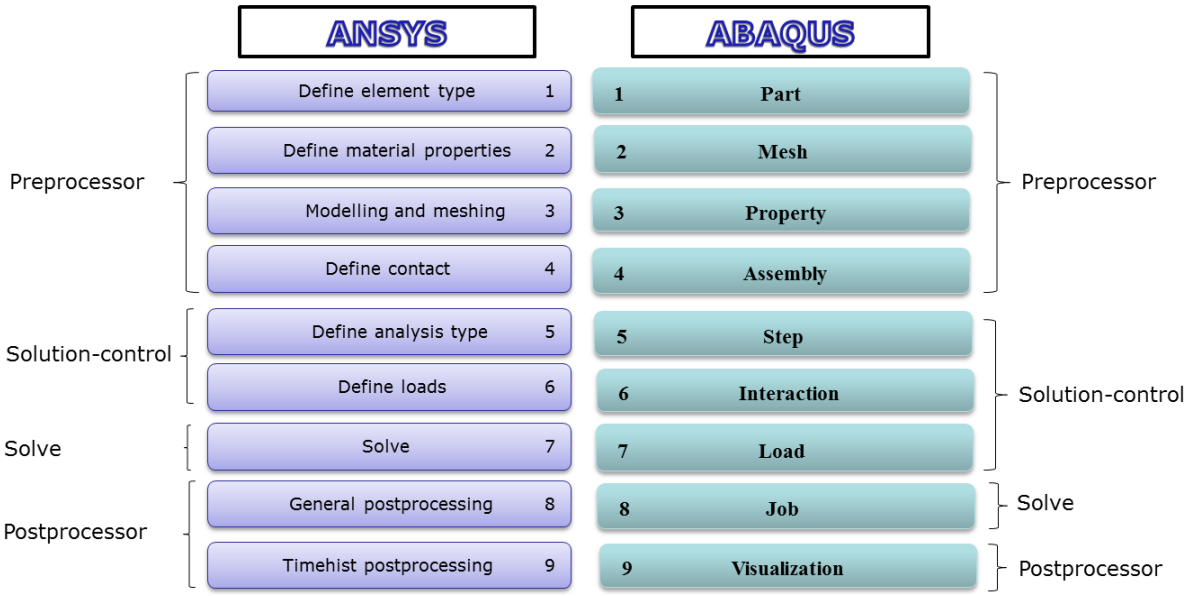

Figure 6.1: Comparison between the simulation processes of ANSYS (ANSYS, 2012) and ABAQUS (ABAQUS/CAE, 2012).

The material data needed as input for the FEM software consists of two parts: general parameters and stress-deformation behavior. The general parameters define initial gap, stable stiffness, etc. The stress-deformation behavior includes loading and unloading data. The element SOLID185 (ANSYS, 2012) was chosen in this chapter for defining the material of stiff platform and press head. Element INTER 195 (ANSYS, 2012) was used for defining the gasket material.

SOLID185 is used for the three-dimensional modeling of solid structures. The element is defined by eight nodes having three degrees of freedom at each node: translations in the nodal CD, MD, and ZD directions. INTER195 is a 3-D 8-node linear interface element. When used with 3-D linear structural elements (SOLID185 etc.), INTER195 simulates gasket joints. It is defined by eight nodes having three degrees of freedom at each node: translations in the nodal CD, MD, and ZD directions (ANSYS, 2012).

Figure 6.2 is a simple finite element model created to demonstrate the gasket material simulation. Two block elements of type SOLID 185 (ANSYS, 2012) were generated for the sample supporter (the indenter and the platform) and a gasket element INTER 195 (ANSYS, 2012) was created for the sample itself.

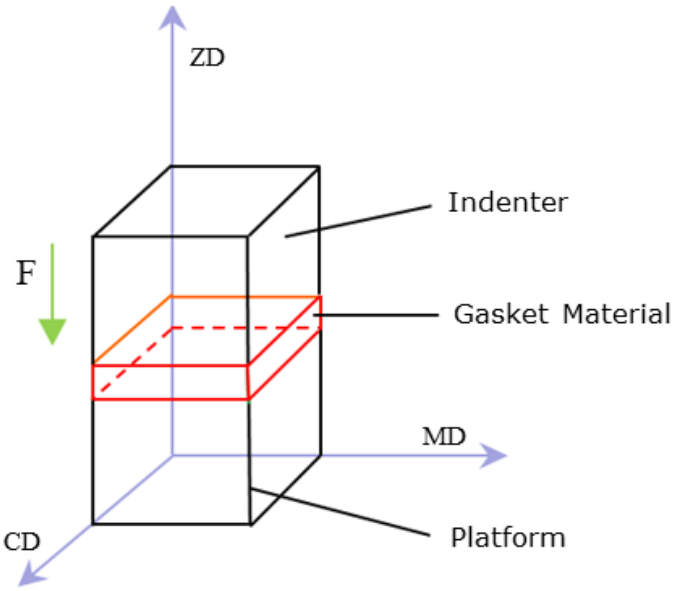

Figure 6.2: Schematic representation of the simulation model. The in-plane stiffness and transverse shear is negligible. The ZD direction is the out-of-plane direction.

The definition of the material properties can be divided into two parts: the loading stage and the unloading stage, the behavior of each has to be defined, respectively. The in-plane stiffness and transverse shear was negligible when compared to the stiffness in the out-of-plane direction. The loading and unloading curve of gasket material can be obtained from the following compression curve function (Jorwekar et al., 2006).

The compressibility model for synthetic gasket material is:

$$\varepsilon = a \cdot \left(1 - e^{-(\sigma/b)}\right) + c \cdot \left(1 - e^{-(\sigma/d)}\right) + u \tag{6.1}$$

The derivative of the above equation:

$$\frac{d\varepsilon}{d\sigma} = \left(a/b\right) \cdot e^{-(\sigma/b)} + \left(c/d\right) \cdot e^{-(\sigma/d)} \tag{6.2}$$

The instantaneous modulus can be expressed as the inverse of Equation 6.2:

$$E = \frac{d\sigma}{d\varepsilon} \tag{6.3}$$

Unloading curve function (due to the unrecoverable strain):

$$u(\sigma_y) = a \cdot \left(1 - e^{-\left(\sigma_y/b\right)}\right) + c \cdot \left(1 - e^{-\left(\sigma_y/d\right)}\right) - \left[a' \cdot \left(1 - e^{-\left(\sigma_y/b'\right)}\right) + c' \cdot \left(1 - e^{-\left(\sigma_y/d'\right)}\right)\right] \tag{6.4}$$

where ε is the strain or the percentage of the compression; σ is the stress; a and c are the scale factors; b and d are the time variables; σ_y is the maximum stress achieved and u is the loading offset, when u=0, which is used for the loading curve.

According to the equations provided above, the loading and unloading behavior of gasket material can be calculated. Equation 6.1 gives the loading curve function of gasket material, equation 6.4 gives the unloading curve function of gasket material under the unrecoverable strain.

6.3 Adapting the gasket model to paper material

The stress-deformation curves of paper material and gasket material are J-shaped, both of which can be described by using the model described in Equations 6.1 to 6.4. In this section, the gasket model described above will be used to do the simulation of paper materials.

For the loading stage, the stress and deformation (reduced thickness in mm) data are needed for defining the paper property. Some discrete data points $A_i(x_i, y_i)$ (i=1, … , n) that obtained by the experiment were selected as shown in Figure 6.3. x_i is the value of deformation, y_i is the corresponding stress value (MPa).

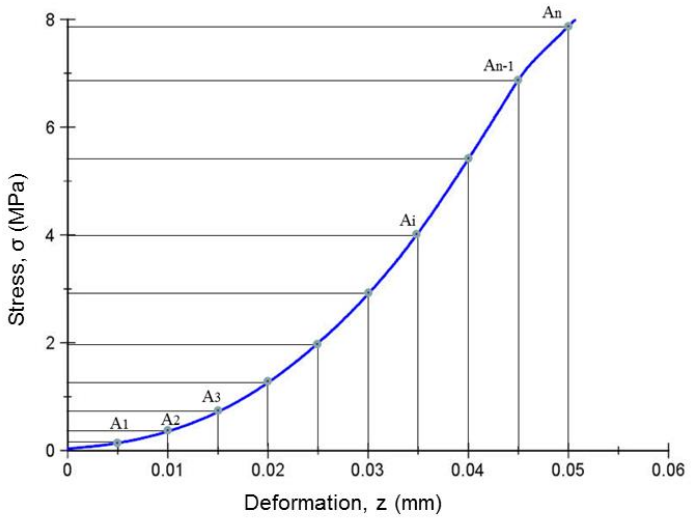

Figure 6.3: The data $A_i(x_i, y_i)$ (i=1, … , n) selected in the loading stage for defining the loading property of paper (the blue curve).

For the unloading stage, two different unloading simulation methods are provided: linear unloading simulation and nonlinear unloading simulation. The linear unloading material definition option is a simple way to define the paper unloading behavior, in which several unloading slopes (Equation 6.2) can be defined to accommodate the unloading behavior. The

nonlinear unloading gasket material definition option provides a more comprehensive way of defining gasket material unloading behavior (Equation 6.4).

Some discrete data points $B_j(x_j, y_j)$ (j=1, … , m) in the unloading stage were selected as shown in Figure 6.4. All the longitudinal coordinate values of these selected points should be the same as the loading points. The main difference between the linear unloading simulation and nonlinear unloading simulation lies in the definition of the employed material parameters. For linear unloading simulation, x_j is the value of deformation (mm), y_j is the corresponding unloading slope (-) (Equation 6.2). For nonlinear unloading simulation, x_j is the value of deformation (mm), y_j is the corresponding unloading stress value (MPa). The point A_n of maximal loading should be the same as B_m, the starting point of the unloading stage.

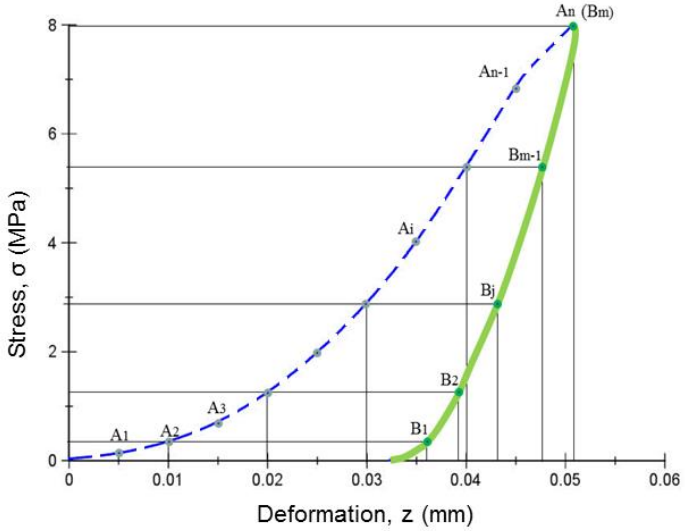

Figure 6.4: The data $B_j(x_j, y_j)$ (j=1, … , m) selected in the unloading stage for defining the unloading property of paper (the lime curve).

After that, building the simulation model as shown in Figure 6.2. Then meshing, defining the constraint condition and imposing the load are undertaken.

6.4 Results and discussion

The simulation results were then derived in the post-processing step. The force-deformation curve could be obtained directly and the data could also be stored as text documents.

6.4.1 Paper simulation under a defined force

For comparison between the simulation and the experimental results, a maximum force of 100 N was applied in the loading stage, and implemented in both the simulation of linear

unloading and nonlinear unloading stages. The simulation results are shown in Figure 6.5 and Figure 6.6. Figure 6.5 shows the simulation result under linear unloading (program code see Appendix A14), Figure 6.6 shows the simulation result under nonlinear unloading.

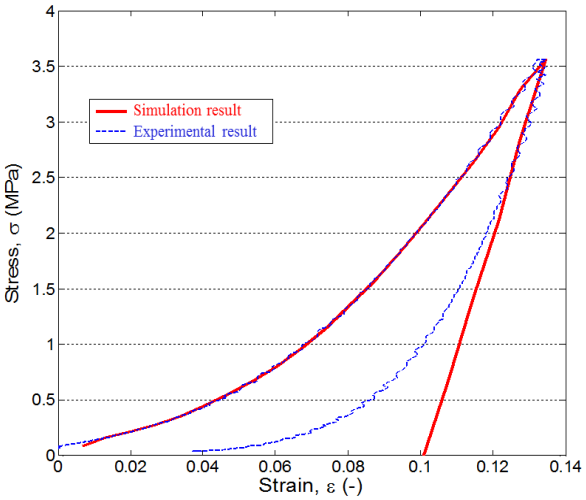

Figure 6.5: Linear unloading simulation result compared with the experimental result. The nominal area of the indenter is about 28.27 mm^2. A pressure of 3.5 MPa corresponds to about 100 N. The experimental result is drawn based on the data shown in Figure 2.5 (a).

Figure 6.5 shows the comparison of the experimental and the simulated stress-deformation curves of compression in the out-of-plane direction. The simulation result of the loading stage is in agreement with the experimental result. To a certain extent, the linear unloading simulation can qualitatively describe the trend of the actual process, but is still lacking full predictive accuracy.

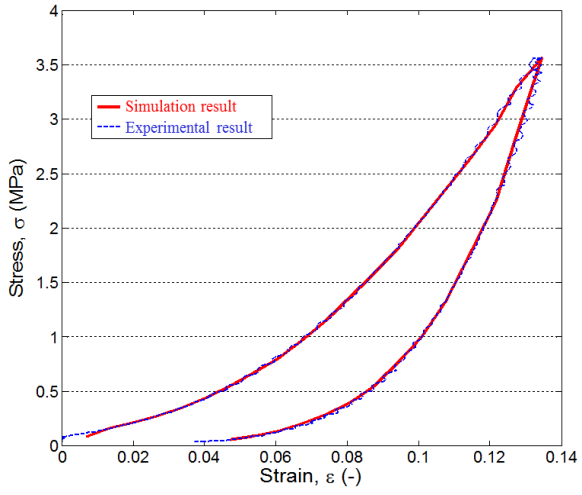

Figure 6.6: Nonlinear unloading simulation result compared with the experimental result. The nominal area of the indenter is about 28.27 mm^2. A stress of 3.5 MPa corresponds to about 100 N. The experimental result is drawn based on the data shown in Figure 2.5 (a).

Figure 6.6 displays the comparison of the experimental and the nonlinear unloading simulated curve (program code see Appendix A15). As shown previously, the simulation result is much more precise, and this simulation model can be used with high confidence in doing further simulations of paper compression.

6.4.2 Paper simulation with variable maximum forces

According to the simulation model of paper material established above, the compression simulation of paper under different forces were conducted, the results are shown in Figure 6.7 with red curves. Three groups of simulations were implemented here, in which the respective maximum forces applied are 20 N, 40 N and 60 N.

In order to verify the applicability of the simulation model, some experiments on paper were performed by using different maximum compression forces and their results are shown in Figure 6.7 (the dotted blue curves). In the experimental process, the maximum forces provided were also 20 N, 40 N and 60 N. The experiments were made at different points of the paper surface. For each load and unload cycle, the moving speed of the pressure head was set as 0.05 mm/min.

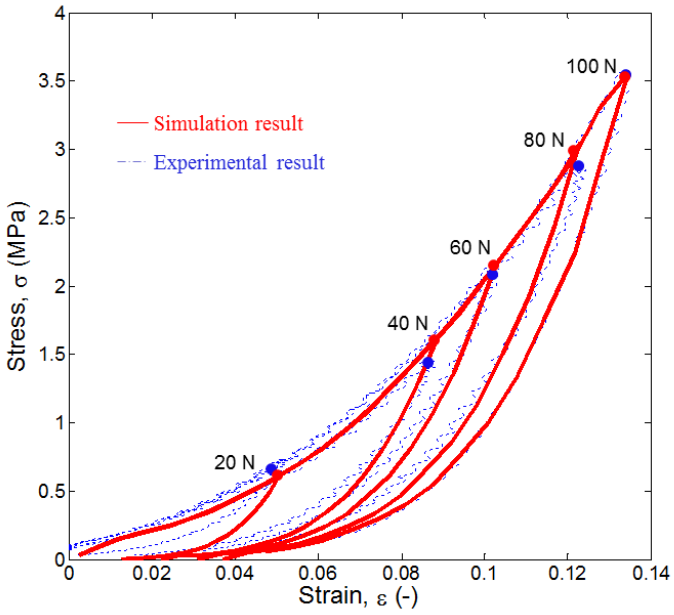

Figure 6.7: Experimental results and simulation results under different strains (forces). The red curves are the simulation results. The blue dashed curves are the experimental results, which are measured as shown in Figure 2.12. The nominal area of the indenter is about 28.27 mm^2. The corresponding values of forces at the start point of unloading are also provided in this figure. A stress of 3.5 MPa corresponds to about 100 N.

The material properties were defined according to the experimental stress-deformation data under 100 N, and all the simulation results for 20 N, 40 N, 60 N and 80 N were based on this model. From Figure 6.7, it can be seen that the agreement between FEM simulation and the experimental result is very good. The gasket model can be perfectly used for paper simulation. The method can be used with high confidence for the simulation of paper under other different forces.

To compare the results between simulations and experiments, we take the deviation of the maximum stress and the residual strain as examples, the comparison results are shown in Table 6.1.

Table 6.1: Comparisons of the force-deformation curves of paper stacks between the experimental and theoretical result, which is based on the deformation at the start point of unloading.

Force	20 N	40 N	60 N	80 N	100 N
Maximum stress (MPa)					
Simulation results	0.62	1.62	2.16	3.04	3.56
Experimental results	0.73	1.45	2.16	2.87	3.56
Deviation	15.10%	11.70%	0.00%	5.90%	0.00%
Residual strain (-)					
Simulation results	0.24×10^{-1}	0.17×10^{-1}	0.21×10^{-1}	0.27×10^{-1}	0.38×10^{-1}
Experimental results	0.13×10^{-1}	0.22×10^{-1}	0.31×10^{-1}	0.37×10^{-1}	0.47×10^{-1}
Deviation	84.60%	22.70%	32.20%	27.00%	19.10%

In Table 6.1, the deviations of the maximum stress and the residual strain are listed, from which it can be seen that the deviation of the residual strain is bigger than the deviation of the maximum stress. The material properties were defined according to the experimental stress-deformation data under 100 N. For the simulation results, the closer the force is approaching 100 N, the smaller the deviation of the maximum stress and residual strain. The deviation is generated not only because of the simulation method, but also because of the unevenness of the paper density.

6.5 Summary

In this chapter, a much easier way than previously reported techniques was proposed to simulate the z-direction compression of paper, avoiding many difficult measurements (Andersson, 2006) that would normally be needed for defining the parameters. The method is

based on finite element modelling using the gasket approximation. This result will also provide a basis for the simulation of multiple sheets or paper stacks. Intrinsically, the simulation method presented here implies some type of nonlinear curve fitting, especially the simulation under a defined force, but it provides a way of doing the simulation of paper under any different forces to a high level of predictive confidence.

But in this chapter, the paper material was modelled here as a smooth, solid material, where the influence of surface roughness has not been taken into account. Some simulation works should be supplemented by considering the surface topography.

7 Conclusions and outlook

This chapter reflects the main outcome of my work. First, the presented work is summarized and the results are discussed, then, an outlook on future work is described.

7.1 Conclusions

The main objectives of this dissertation have been mentioned in the first chapter, the mechanical behavior of paper and paper stacks in the out-of-plane direction was discussed from three different research perspectives: the actual stress-strain curve of paper was calculated and compared with the nominal stress-strain curve, two different methods were proposed for calculating the force-deformation curves of multiple sheets, the paper material was simulated by using a gasket model.

Firstly, the big differences between the nominal contact area and the actual contact area were introduced. A new method was proposed for showing the actual contact area. With the aid of image processing technology, the actual contact area of paper under different forces were calculated. According to the obtained results, the actual stress-strain curve was drawn and compared with the nominal stress-strain curve, from which it can be apparently seen that there's a big difference between the actual stress-strain curve and the nominal stress-strain curve. Different carbon papers have different force sensitivities. To improve the calculation accuracy, the sensitivities of some different carbon papers were compared. A much more precise experimental program was designed and carried out. The result based on the new scheme further proof the feasibility and the correctness of the proposed method.

Secondly, according to the knowledge of the author, until now, there's still no model proposed before, which can be used for calculating the force-deformation behavior of paper stacks. In this dissertation, the author tried to build the mathematical models for multiple sheets by using two different methods:

On the basis of the model proposed by Schaffrath, the pyramid element and the tubular element were introduced to describe the surface structure and the internal structure, respectively. Then, according to Hooke's law or the Paetow's method, the relationship between the total deformation and the surface deformation was calculated by using the Newton-Raphson method. Based on the results obtained above, the force-deformation relation of a single sheet was derived. According to the model of a single sheet, the theoretical models of multiple sheets were established by using different curve fitting functions. By comparing the calculated results with the experimental results, it is proved that the proposed theoretical

model can be used for calculating the force-deformation curve of multiple sheets, especially, when the number of sheets is between 20 and 140.

According to the model proposed by Takaki, the loading and unloading stages of gasket materials were described by using two different functions. Based on the assumption that when the force is the same, the deformations of paper stacks are proportional to the number of sheets, a new model for describing the force-deformation curves of multiple sheets can be derived. As can be seen from the calculation results that the proposed descriptive model can be used for calculating the force-deformation curves of multiple sheets, especially, when the number of sheets is between 20 and 140.

Thirdly, a much easier way to simulate the paper material by using a gasket model was proposed. The material property was defined based on the experimental data under a certain force. Then, some simulations under other forces were implemented. As indicated, this method can be used with high confidence for the simulation of paper under different forces.

7.2 Outlook

Based on the works finished above, this section presents some suggestions for further investigations and applications of the presented work.

Firstly, because of the thickness of paper is very small and the platform is not an ideal stiff material, the force-deformation of the paper is affected by the platform. How big influences are from the platform should be further discussed.

Secondly, the viscosity of paper material is not taken into account, which is also a very important behavior of paper materials. Some questions about the viscosity of paper such as: how to measure or describe the viscosity of paper, how to separate the viscosity behavior of paper from the elastic-plastic curve of paper, etc., should be investigated in the future studies.

Thirdly, with the aid of the carbon papers, some experiments under the forces changing from 2 N to 100 N were implemented. But in this thesis, the author didn’t discuss the situation with forces bigger than 100 N. More tests with forces bigger than 100 N should be implemented.

Fourthly, the theoretical model of multiple sheets is based on the Schaffrath’s model, the values of some parameters in the model are not provided. For some of the parameters, the author only provided the values. The sensitivity of these parameters on the final calculation results should be compared and discussed. This theoretical model can only be used for calculating the loading stage of paper or paper stack. So if it is possible to extend the model with considering the unloading stage is also a very interesting question.

Fifthly, the calculation results show that both of the theoretical model and the descriptive model proposed in this dissertation can be used for calculating the force-deformation curves

of multiple sheets, especially, when the number of sheets is between 20 and 140. The reason why these models cannot be used when the number is bigger than 140 should be further investigated.

Lastly, some simulation work of a single sheet was carried out, but the simulation of multiple sheets was not discussed. Besides, the surface structure of paper was not taken into consideration, how to build the simulation model of paper with considering the surface topography is also an interesting research subject.

8 References

ABAQUS/CAE 2012. ABAQUS/CAE 6.12-1 User's Manual. 6.12-1 ed.: ABAQUS, Inc.

ABORAIA, M., SHARKAWI, R. & DOHEIM, M. 2011. Production of aluminium foam and the effect of calcium carbonate as a foaming agent. *Journal of Engineering Sciences, Assiut University,* 39**,** 441-451.

ALAM, M. A. 2012. *Online surface topography characterization technique for paper and paperboard using line of light triangulation.* Dissertation, Mid Sweden University.

ALAM, M. A., THIM, J., MANUILSKIY, A., O'NILS, M., WESTERLIND, C., LINDGREN, J. & LIDÉN, J. 2011. Investigation of the surface topographical differences between the Cross Direction and the Machine Direction for newspaper and paperboard. *Nordic Pulp and Paper Research Journal,* 26**,** 468-475.

ALZOUBI, M., AL-HALLAJ, S. & ABU-AYYAD, M. 2014. Modeling of compression curves of flexible polyurethane foam with variable density, chemical formulations and strain rates. *Journal of Solid Mechanics,* 6**,** 82-97.

ANDERSSON, T. 2006. *A small deformation model for the elasto-plastic behaviour of paper and paperboard.* Master's Thesis, Lund University.

ANSYS 2012. ANSYS Help system–mechanical APDL-Element reference. 14.5 ed.: ANSYS, Inc.

BACHUS, K. N., DEMARCO, A. L., JUDD, K. T., HORWITZ, D. S. & BRODKE, D. S. 2006. Measuring contact area, force, and pressure for bioengineering applications: using Fuji Film and TekScan systems. *Medical Engineering and Physics,* 28**,** 483-488.

BAJPAI, P. 2011. *Biotechnology for pulp and paper processing*, Springer Science and Business Media.

BAKARICH, S. E., PIDCOCK, G. C., BALDING, P., STEVENS, L. & CALVERT, P. 2012. Recovery from applied strain in interpenetrating polymer network hydrogels with ionic and covalent cross-links. *Soft Matter,* 8**,** 9985-9988.

BEEX, L. & PEERLINGS, R. 2009. An experimental and computational study of laminated paperboard creasing and folding. *International Journal of Solids and Structures,* 46**,** 4192-4207.

BHAT, S., TRIPATHI, A. & KUMAR, A. 2011. Supermacroprous chitosan–agarose–gelatin cryogels: in vitro characterization and in vivo assessment for cartilage tissue engineering. *Journal of the Royal Society Interface,* 8**,** 540-554.

BRONKHORST, C. 2003. Modelling paper as a two-dimensional elastic–plastic stochastic network. *International Journal of Solids and Structures,* 40**,** 5441-5454.

BUCHNER, B., BUCHNER, M. & BUCHMAYR, B. 2009. Determination of the real contact area for numerical simulation. *Tribology International,* 42**,** 897-901.

BUCHNER, B. T. P. 2008. *Investigation of friction in closed-die warm forging of aluminium alloys.* Dissertation, University of Leoben.

CALIRI JÚNIOR, M. F., SOARES, G. P., ANGÉLICO, R. A., CANTO, R. B. & TITA, V. 2012. Study of an anisotropic polymeric cellular material under compression loading. *Materials Research,* 15**,** 359-364.

CARTRAUD, P. & WIELGOSZ, C. 1996. Numerical modelling of the elastoplastic behaviour of a gasket material. *Computational Materials Science,* 5**,** 75-81.

CHEN, J., NEUMANN, J. & DÖRSAM, E. Investigation on deformation behavior of paper in Z-direction. Proceeding of the Progress in Paper Physics Seminar, 2014a Raleigh, North Carolina, USA

CHEN, J., NEUMANN, J., SAUER, H. M. & DÖRSAM, E. A new FEM simulation method of paper materials by using a gasket model. Proceeding of the 42nd International Research Conference of IARIGAI, 2015 Helsinki, Finnland. 125-139.

CHEN, J., DÖRSAM, E., SPIEHL, D., HAKIMI TEHRANI, A. & DA, J. Stress-strain behavior of paper affected by the actual contact area. Proceeding of the Progress in Paper Physics Seminar, 2016 Darmstadt, Hessen, Germany. 47-53.

CHEN, L., AHADI, A., ZHOU, J. & STÅHL, J.-E. 2013. Modeling Effect of Surface Roughness on Nanoindentation Tests. *Procedia CIRP,* 8**,** 334-339.

CHEN, L., AHADI, A., ZHOU, J. & STÅHL, J.-E. 2014b. Numerical and Experimental Study of the Roughness Effects on Mechanical Properties of AISI316L by Nanoindentation. *Modeling and Numerical Simulation of Material Science,* 4**,** 153-162.

CHIRITA, M. & IONESCU, C. 2011. Models of biomimetic tissues for vascular grafts. *In:* PRAMATAROVA, L. (ed.) *On Biomimetics.* InTech.

CROOP, B., LOBO, H. & DATAPOINTLABS, N. Selecting material models for the simulation of foams in LS-DYNA. Proceedings of the 7th European LS-DYNA conference, 2009 Dynamore Gmbh, Salzburg, Germany.

DE VRIES, D. 2009. *Characterization of polymeric foams.* Master's Thesis, Eindhoven University of Technology.

DESCH, M., KAULITZ, T. & DÖRSAM, E. Industrial Use for the “nip-inducted effect” to separate sheets. Proceedings of the International Conference on Web Handling (IWEB), 2009 Oklahoma, USA

DIAZ, J. M. A., PFIRRMANN, J. & SCHMITT, N. 2009. Konzept zur blattgenauen Mengenbestimmung eines Stapels blattförmigen Materials mittels Druckstempel. Technische Universität Darmstadt.

DONG, W., HUANG, C., WANG, Y., SUN, Y., MA, P. & CHEN, M. 2013. Superior Mechanical Properties of Double-Network Hydrogels Reinforced by Carbon Nanotubes without Organic Modification. *International Journal of Molecular Sciences,* 14**,** 22380-22394.

DU BOIS, P. A. 2009. The Numerical Simulation of Foam–An Example of Inter-Industrial Synergy. *In:* HIERMALER, S. (ed.) *Predictive Modeling of Dynamic Processes.* Springer.

ECKSTEIN, M. 2014. *Instabilities and Wear Propagation in Calenders: Interactions with Structural Dynamics and Contact Kinematics.* Dissertation, Technische Universität Darmstadt.

ECKSTEIN, M. & HAGEDORN, P. 2014. On the effect of paper plasticity in calenders. *ZAMM-Journal of Applied Mathematics and Mechanics/Zeitschrift für Angewandte Mathematik und Mechanik,* 94**,** 923-932.

EGMASON. 2010. *Diagram showing the sections of the Fourdrinier machine* [Online]. Available: https://commons.wikimedia.org/wiki/File%3AFourdrinier.svg [Accessed 23.10 2015].

EKMAN, A., MIETTINEN, A., TURPEINEN, T., BACKFOLK, K. & TIMONEN, J. 2012. The number of contacts in random fibre networks. *Nordic Pulp and Paper Research Journal,* 27**,** 270-276.

ENDRES, I. 2006. *Compression uniformity measurements on coated and uncoated paper surfaces.* Ph.D. Thesis, University of Karlstad.

FUJIFILM. 2016. *Prescale Sheet Type* [Online]. Fujifilm Corporation. Available: http://www.fujifilm.com/products/prescale/prescale_sheettype/ [Accessed 23.10 2016].

FUKUOKA, T., NOMURA, M., HATA, Y. & NISHIKAWA, T. Development of Test Equipment for Measuring Compression Characteristics of Sheet Gaskets at Elevated Temperature. ASME 2007 Pressure Vessels and Piping Conference, 2007. American Society of Mechanical Engineers, 165-169.

FUKUOKA, T., NOMURA, M. & NISHIKAWA, T. 2012. Analysis of thermal and mechanical behavior of pipe flange connections by taking account of gasket

compression characteristics at elevated temperature. *Journal of Pressure Vessel Technology,* 134**,** 021202 1-021202 7.

FUKUOKA, T. & TAKAKI, T. 2003. Finite element simulation of bolt-up process of pipe flange connections with spiral wound gasket. *Journal of Pressure Vessel Technology,* 125**,** 371-378.

GAUTIERI, A., VESENTINI, S., REDAELLI, A. & BUEHLER, M. J. 2011. Hierarchical structure and nanomechanics of collagen microfibrils from the atomistic scale up. *Nano Letters,* 11**,** 757-766.

GAVELIN, G. 1949. The compressibility of newsprint. *Svensk Papperstidning,* 52**,** 413-419.

GUARINO, V., URCIUOLO, F., ALVAREZ-PEREZ, M. A., MELE, B., NETTI, P. A. & AMBROSIO, L. 2012. Osteogenic differentiation and mineralization in fibre-reinforced tubular scaffolds: theoretical study and experimental evidences. *Journal of the Royal Society Interface***,** 1-12.

GUBICZA, J. Determination of Young's modulus from depth sensing Vickers indentation tests. Solid State Phenomena, 1997 Switzerland. Trans Tech Publ, 195-200.

GUREVITCH, I. & SILVERSTEIN, M. S. 2012. Shape memory polymer foams from emulsion templating. *Soft Matter,* 8**,** 10378-10387.

HANSSON, P. & JOHANSSON, P.-Å. 2000. Topography and reflectance analysis of paper surfaces using a photometric stereo method. *Optical Engineering,* 39**,** 2555-2561.

HARRASS, K., KRÜGER, R., MÖLLER, M., ALBRECHT, K. & GROLL, J. 2013. Mechanically strong hydrogels with reversible behaviour under cyclic compression with MPa loading. *Soft Matter,* 9**,** 2869-2877.

HE, J. 2005. *Quantitative study of paper structure at the fibre level for development of a model for the tensile strength of paper.* Dissertation, Monash University.

HEYDEN, S. 2000. *Network modelling for the evaluation of mechanical properties of cellulose fibre fluff.* Dissertation, Lund University.

HOFFMANN, P. 2010. *Lagenverschiebungen und Spannungsaufbau in der Nipzone zwischen Walze und Papierlagen.* Dissertation, Technische Universität Darmstadt.

HOLZAPFEL, G. A. 2001. Biomechanics of soft tissue. *The handbook of materials behavior models,* 3**,** 1049-1063.

HU, X., FENG, L., WEI, W., XIE, A., WANG, S., ZHANG, J. & DONG, W. 2014a. Synthesis and characterization of a novel semi-IPN hydrogel based on Salecan and poly (N, N-dimethylacrylamide-co-2-hydroxyethyl methacrylate). *Carbohydrate Polymers,* 105**,** 135-144.

HU, X., FENG, L., XIE, A., WEI, W., WANG, S., ZHANG, J. & DONG, W. 2014b. Synthesis and characterization of a novel hydrogel: salecan/polyacrylamide semi-IPN hydrogel with a desirable pore structure. *Journal of Materials Chemistry B,* 2**,** 3646-3658.

HUANG, H., HAGMAN, A. & NYGÅRDS, M. 2014. Quasi static analysis of creasing and folding for three paperboards. *Mechanics of Materials,* 69**,** 11-34.

IMRAN, A. B., SEKI, T. & TAKEOKA, Y. 2010. Recent advances in hydrogels in terms of fast stimuli responsiveness and superior mechanical performance. *Polymer Journal,* 42**,** 839-851.

IVARSSON, B. 1956. Compression of cellulose fiber sheets. *Tappi,* 39**,** 97-104.

JANG, K.-I., CHUNG, H. U., XU, S., LEE, C. H., LUAN, H., JEONG, J., CHENG, H., KIM, G.-T., HAN, S. Y. & LEE, J. W. 2015. Soft network composite materials with deterministic and bio-inspired designs. *Nature Communications,* 6.

JORWEKAR, P. P., BIRARI, Y. V. & NADGOUDA, M. M. Cylinder head gasket contact pressure simulation for a hermetic compressor. International Compressor Engineering Conference, 2006 Purdue University, Indiana, USA. C071, 1-7.

KATO, K., MATSUI, D., MAYUMI, K. & ITO, K. 2015. Synthesis, structure, and mechanical properties of silica nanocomposite polyrotaxane gels. *Beilstein Journal of Organic Chemistry,* 11**,** 2194-2201.

KATTA, J. & RASMUSON, Å. C. 2008. Spherical crystallization of benzoic acid. *International Journal of Pharmaceutics,* 348**,** 61-69.

KAULITZ, T. 2009. *Bilden von Schneidlagen unter Ausnutzung des Nipinduzierten Effekts für die Druckweiterverarbeitung.* Dissertation, Technische Universität Darmstadt.

KAULITZ, T. & DÖRSAM, E. Highly accurate material characterization of paper for the simulation of printing process. Proceeding of the 42nd International Research Conference of IARIGAI, 2008 Valencia, Spain. 263-270.

KIM, B.-S. & MOONEY, D. J. 2000. Scaffolds for engineering smooth muscle under cyclic mechanical strain conditions. *Journal of Biomechanical Engineering,* 122**,** 210-215.

KOLLING, S., WERNER, A., ERHART, T. & DU BOIS, P. A. An elastic damage model for the simulation of recoverable polymetric foams. Proceedings of the 6th LS-DYNA Forum, 2007 Franken- thal, Germany. B-II 31-42.

LAMOUCHE, G., KENNEDY, B. F., KENNEDY, K. M., BISAILLON, C.-E., CURATOLO, A., CAMPBELL, G., PAZOS, V. & SAMPSON, D. D. 2012. Review of tissue simulating phantoms with controllable optical, mechanical and structural properties for use in optical coherence tomography. *Biomedical Optics Express,* 3**,** 1381-1398.

LAVRYKOV, S., LINDSTRÖM, S., SINGH, K. & RAMARAO, B. 2012. 3D network simulations of paper structure. *Nordic Pulp and Paper Research Journal,* 27**,** 256-263.

LI, S. & HU, S. S. Testing the compression property of EVA foam at high strain rate. 2003 SEM Annual Conference and Exposition on Experimental and Applied Mechanics, 2003 Charlotte , North Carolina, USA.

LIU, M., WU, C., JIAO, Y., XIONG, S. & ZHOU, C. 2013. Chitosan–halloysite nanotubes nanocomposite scaffolds for tissue engineering. *Journal of Materials Chemistry B,* 1**,** 2078-2089.

LIU, Y., THOMOPOULOS, S., CHEN, C., BIRMAN, V., BUEHLER, M. J. & GENIN, G. M. 2014. Modelling the mechanics of partially mineralized collagen fibrils, fibres and tissue. *Journal of the Royal Society Interface,* 11**,** 20130835 1-12.

LUONG, C. H. 2000. *Experimental and theoretical investigations of mechanical and thermal relations by calendering of paper.* Ph.D. Thesis, Norwegian University of Science and Technology.

MADRIGAL, F. J. F. 2013. *A study on the structure of paper: the links between paper and fibre properties.* Master's Thesis, The University of British Columbia.

MÄKELÄ, P. & ÖSTLUND, S. 2003. Orthotropic elastic–plastic material model for paper materials. *International Journal of Solids and Structures,* 40**,** 5599-5620.

MARK, R. E. & BORCH, J. 2001. *Handbook of physical testing of paper*, CRC Press.

MARULIER, C., DUMONT, P., ORGÉAS, L., CAILLERIE, D. & DU ROSCOAT, S. R. 2012. Towards 3D analysis of pulp fibre networks at the fibre and bond levels. *Nordic Pulp and Paper Research Journal,* 27**,** 245-255.

MATLAB 2013. Documentation Center / Image Processing Toolbox / Image Analysis / Region and Image Properties / Function. *MATLAB User's Help Manual.* R2013a ed.: MathWorks, Inc.

MONICA, E., GORAN, G. & GUNNAR, H. 2009. *Paper Products Physics and Technology*, Deutsche Nationalbibliografie.

MURALI KRISHNA, M., SHUNMUGAM, M. S. & SIVA PRASAD, N. 2007. A study on the sealing performance of bolted flange joints with gaskets using finite element analysis. *International Journal of Pressure Vessels and Piping,* 84**,** 349-357.

NAGASAWA, S., FUKUZAWA, Y., YAMAGUCHI, T., TSUKATANI, S. & KATAYAMA, I. 2003. Effect of crease depth and crease deviation on folding deformation characteristics of coated paperboard. *Journal of Materials Processing Technology,* 140**,** 157-162.

NAGATA, S., SHOJI, Y. & SAWA, T. A simplified modeling of gasket stress–strain curve for FEM analysis in bolted flange joint design. ASME 2002 Pressure Vessels and Piping Conference, 2002 Vancouver, BC, Canada.

NEEL, E. A. A., CHEEMA, U., KNOWLES, J. C., BROWN, R. A. & NAZHAT, S. N. 2006. Use of multiple unconfined compression for control of collagen gel scaffold density and mechanical properties. *Soft Matter,* 2**,** 986-992.

NEWBERRY, M., MANN, G., MORELL, M. & MORGENSTERN, M. 2005. Elongational rheology of wheat flour doughs. *Cereals 2005*.

NYGÅRDS, M., HALLBÄCK, N., JUST, M. & TRYDING, J. A finite element model for simulations of creasing and folding of paperboard. ABAQUS Users's Conference, 2005 Graz, Austria.

NYGÅRDS, M., JUST, M. & TRYDING, J. 2009. Experimental and numerical studies of creasing of paperboard. *International Journal of Solids and Structures,* 46**,** 2493-2505.

OTSU, N. 1979. A threshold selection method from gray-level histograms. *Automatica,* 11**,** 23-27.

PAETOW, R. & GÖTTSCHING, L. 1990. Spannungs-Dehnungs-Verhalten von Papier: ein neues Materialmodell. *Das Papier,* 44**,** V75-V83.

PAPERONLINE. 2015a. *History of paper* [Online]. Confederation of European Paper Industries (CEPI). Available: http://www.paperonline.org/history-of-paper [Accessed 23.10 2015].

PAPERONLINE. 2015b. *Papermaking* [Online]. Confederation of European Paper Industries (CEPI). Available: http://www.paperonline.org/paper-making/paper-production/papermaking [Accessed 23.10 2015].

PERSSON, K. 2000. *Micromechanical modelling of wood and fibre properties.* Dissertation, Lund University.

PFEIFFER, J. 1981. Measurement of the K2 factor for paper. *Tappi,* 64**,** 105-106.

PICU, R. 2011. Mechanics of random fiber networks-a review. *Soft Matter,* 7**,** 6768-6785.

PIETRYGA, M. 2003. FE-Modellierung des mechanischen Werkstoffverhaltens von Papier in Dickenrichtung. Ruhr Universität Bochum

PINO, A. & PLADELLORENS, J. Measure of roughness of paper using speckle. Proceeding of SPIE Optical Engineering Applications, 2009. International Society for Optics and Photonics, 74320E 1-9.

POOLTHONG, S. 1998. *Determination of the mechanical properties of enamel dentine and cementum by an ultra micro-indentation system.* Dissertation, The University of Sydney.

RAMASUBRAMANIAN, M. & WANG, Y. 2007. A computational micromechanics constitutive model for the unloading behavior of paper. *International Journal of Solids and Structures,* 44**,** 7615-7632.

RAMON, O., MIZRAHI, S. & MILTZ, J. 1990. Mechanical properties and behavior of open cell foams used as cushioning materials. *Polymer Engineering and Science,* 30**,** 197-201.

RÄTTÖ, P. 2005. The influence of surface roughness on the compressive behaviour of paper. *Nordic Pulp and Paper Research Journal,* 20**,** 304-307.

RIBEIRO, H. A. & COSTA, C. A. 2007. Modelling and simulation of the nonlinear behaviour of paper: A cellular materials approach. *Chemical Engineering Science,* 62**,** 6696-6708.

SANTI, P. M., HOLSCHEN, J. E. & STEPHENSON, R. W. 2000. Improving elastic modulus measurements for rock based on geology. *Environmental and Engineering Geoscience,* 6**,** 333-346.

SCHAFFRATH, H.-J. 1993. *Die Kompression in der Dickenrichtung des Papiers.* Dissertation, Technische Universität Darmstadt.

SCHAFFRATH, H.-J. & GÖTTSCHING, L. 1992a. Das Kompressionsverhalten von Papier in ZD. *Das Papier,* 46**,** 74-81.

SCHAFFRATH, H.-J. & GÖTTSCHING, L. 1992b. Modellierung der Kompression von Papier in z-Richtung bei niedriger Flächenpressung. *Das Papier,* 46**,** 350-355.

SCHAFFRATH, H. & GOTTSCHING, L. The Behavior of Paper under Compression in Z-direction. Proceedings of the 1991 Tappi International Paper Physics Conference, 1991 Hawaii, USA. 489-510.

SERIFI, E., HIRTH, A., MATTHAEI, S. & MULLERSCHON, H. Modeling of foams using Mat83–preparation and evaluation of experimental data. Proceedings of the 4th European LS-DYNA Users Conference, 2003 Ulm, Germany. D-II 59-72.

SHERGOLD, O. A., FLECK, N. A. & RADFORD, D. 2006. The uniaxial stress versus strain response of pig skin and silicone rubber at low and high strain rates. *International Journal of Impact Engineering,* 32**,** 1384-1402.

SHODOR. 1997. *Advanced Concepts in Chemistry-Newton-Raphson Method* [Online]. Shodor Education Foundation, Inc. and Department of Chemistry at the University of North Carolina at Chapel Hill. . Available: https://www.shodor.org/unchem/math/newton/ [Accessed 01.06 2016].

SIMON, J.-W., LI, Y. & REESE, S. Modeling the creasing of paperboard. Proceeding of the 11th World Congress on Computational Mechanics (WCCM XI), 2014 Barcelona, Spain.

SINGH, S. P. 2008. A comparison of different methods of paper surface evaluation. *BioResources,* 3**,** 503-516.

SLIK, G., VOGEL, G. & CHAWDA, V. Material model validation of a high efficient energy absorbing foam. Proceedings of the 5th LS-DYNA Forum, 2006 Ulm, Germany.

STENBERG, N. 1999. Mechanical properties in the thickness direction of paper and paperboard. *Licentiate thesis, KTH Stockholm*.

STENBERG, N. 2002. *On the out-of-plane mechanical behaviour of paper materials.* Dissertation, Royal Institute of Technology.

STENBERG, N. 2003. A model for the through-thickness elastic–plastic behaviour of paper. *International Journal of Solids and Structures,* 40**,** 7483-7498.

STENBERG, N. & FELLERS, C. 2002. Out-of-plane Poisson's ratios of paper and paperboard. *Nordic Pulp and Paper Research Journal,* 17**,** 387-394.

STENBERG, N., FELLERS, C. & OSTLUND, S. 2001. Plasticity in the thickness direction of paperboard under combined shear and normal loading. *Journal of Engineering Materials and Technology,* 123**,** 184-190.

STRÖMBRO, J. & GUDMUNDSON, P. 2008. An anisotropic fibre-network model for mechano-sorptive creep in paper. *International Journal of Solids and Structures,* 45**,** 5765-5787.

SZYNISZEWSKI, S., SMITH, B., HAJJAR, J., SCHAFER, B. & ARWADE, S. 2014. The mechanical properties and modeling of a sintered hollow sphere steel foam. *Materials and Design,* 54**,** 1083-1094.

TAKAKI, T. & FKUOKA, T. 2001. Finite element simulation of bolt-up process of pipe flange connections. *Journal of Pressure Vessel Technology, Transactions of the ASME,* 123**,** 282-287.

TAKAKI, T. & FUKUOKA, T. 2000. Bolt-up strategy for pipe Flange connections using finite element analysis. *Journal of Pressure Vessel Technology, Transactions of the ASME,* 405**,** 143-150.

TAKAKI, T. & FUKUOKA, T. Systematical FE analysis of bolt assembly process of pipe flange connections. ASME 2002 Pressure Vessels and Piping Conference, 2002a. American Society of Mechanical Engineers, 147-152.

TAKAKI, T. & FUKUOKA, T. Three-dimensional finite element analysis of pipe flange connections: the case of using compressed asbestos sheet gasket. ASME 2002

Pressure Vessels and Piping Conference, 2002b. American Society of Mechanical Engineers, 171-177.

TAKAKI, T. & FUKUOKA, T. Methodical Guideline for Bolt-Up Operation of Pipe Flange Connections: A Case Using Sheet Gasket and Spiral Wound Gasket. ASME 2003 Pressure Vessels and Piping Conference, 2003. American Society of Mechanical Engineers, 23-30.

TELEMAN, A., ÖSTLUND, C., NORDSTRÖM, J.-E., JOHANSSON, P.-A. & VOMHOFF, H. 2004. Analysis of paper surface topography under compression.

TITA, V. & CALIRI JÚNIOR, M. F. 2012. Numerical simulation of anisotropic polymeric foams. *Latin American Journal of Solids and Structures,* 9**,** 1-21.

TRONCI, G., DOYLE, A., RUSSELL, S. J. & WOOD, D. J. 2013. Triple-helical collagen hydrogels via covalent aromatic functionalisation with 1,3-phenylenediacetic acid. *Journal of Materials Chemistry B,* 1**,** 5478-5488.

VERNHES, P., BLOCH, J.-F., BLAYO, A. & PINEAUX, B. 2009. Effect of calendering on paper surface micro-structure: A multi-scale analysis. *Journal of Materials Processing Technology,* 209**,** 5204-5210.

VERNHES, P., BLOCH, J.-F., MERCIER, C., BLAYO, A. & PINEAUX, B. 2008. Statistical analysis of paper surface microstructure: A multi-scale approach. *Applied Surface Science,* 254**,** 7431-7437.

VERNHES, P., DUBÉ, M. & BLOCH, J.-F. 2010. Effect of calendering on paper surface properties. *Applied Surface Science,* 256**,** 6923-6927.

VINCENT, R., RUEFF, M. & VOILLOT, C. 3-D Simulation of handsheets made of different pulps. Proceedings of Model Validation Workshop, 2005 Espoo, Finland. 71-78.

XIA, Q. S., BOYCE, M. C. & PARKS, D. M. 2002. A constitutive model for the anisotropic elastic–plastic deformation of paper and paperboard. *International Journal of Solids and Structures,* 39**,** 4053-4071.

YU, C.-J. & BANHART, J. Mechanical properties of metallic foams. Proceedings of Fraunhofer USA Metal Foam Symposium, 1997 Stanton, Delaware, USA. 7-8.

9 Appendix

A1. Transferring the pictures to binary pictures

```
I=imread('D:\research results\experiments\experiments with mikroskop\Jian
Chen\100n\second\01.jpg'); %read the picture from the computer
bw=im2bw(I,0.5); % transfer the picture into 0-1 values picture
subplot(1,2,1);  % build two windows and choose the first one
imshow(I);       % plot the original picture in the first window
title('original picture');

subplot(1,2,2);  % choose the second window
imshow(bw);      % plot the new picture in the second window
title('new picture');

total=bwarea(bw);% caculate the whole number of 1 element
total/(1200*1600)% caculate the total area(%) of 1 element
black=1-total/(1200*1600)% caculate the total area(%) of 0 element(black)
```

A2. Example of calculating contact areas

```
clc
clear

imggray = imread('C:\Jian Chen\pictures\60n\second\02.jpg');
subplot(2,2,1);
imshow(imggray);
title('original picture');

imgbw1 = im2bw(imggray,0.5);
subplot(2,2,2);
imshow(imgbw1);
title( 'threshold value=0.5');

imgbw2 = im2bw(imggray, 0.25);
subplot(2,2,3);
imshow(imgbw2);
title( 'threshold value=0.25');

level = graythresh(imggray);
imgbw3 = im2bw(imggray,level);
subplot(2,2,4);
imshow(imgbw3);
title('Otsu method,threshold value=level');
total=bwarea(imgbw3);% caculate the whole number of 1 element
total/(1200*1600)% caculate the total area(%) of 1 element
black=1-total/(1200*1600)% caculate the total area(%) of 0 element(black)
level
```

A3. Newton-Raphson method - based on Hooke's law

```
clc
clear
z2=0.0005; %the initial value of the root
i=0;
p=1;%number of the sheets
z=0.055; %the total deformation z
A0=pi*9;%nominal contact area mm2
d=0.0847;% thickness of paper mm

m0=1778;
n0=4;

L=0.885;% length of the fiber unit mm
Rr=30;% radius of curvature at the point (line) where the fibers contact
each other, unit mm

Ra=0.0025; % average surface roughness
s=0.0025; %standard deviation of the caliper
RA=Ra+s;%unit mm

B0=0;
B1=((m0.^2)*(L.^2)*Rr)./n0;
B2=((m0.^2)*(L.^2))./(4*(n0.^2));

while i<=100

    z0=z2-((p+1)*(((16*(RA.^3)./(A0*(d-4*RA))).^(1/3))*(B0+B1*z2-
B2*(z2.^2)).^(1/6)).*(z2.^(1/3))+p*z2-z)./((p+1)*((16*(RA.^3)./(A0*(d-
4*RA))).^(1/3))*((1/6)*((B0+B1*z2-B2*(z2.^2)).^(-5/6)).*(B1-
B2*2*z2).*(z2.^(1/3))+((B0+B1*z2-B2*(z2.^2)).^(1/6))*(1/3)*(z2.^(-
2/3)))+p);
    if abs(z0-z2)>0.0001
        z2=z0;
    else break
    end
    i=i+1;
end
B1
B2
z2
z1=(z-p*z2)/(p+1)
c=2*z1/z
```

A4. Newton-Raphson method - based on Paetow's method

```
clc
clear
z2=0.00008; %the initial value of the root
i=0;
p=1;%number of the sheets
z1=0.0087; %the surface deformation z1
```

```
A0=pi*9;%nominal contact area mm2
d=0.0847;% thickness of paper mm

m0=1778;%proposed by schaffrath
n0=4;%proposed by schaffrath

L=0.885;% length of the fiber unit mm
Rr=30;%Radius of curvature at the point (line) where the fibers contact
each other unit mm

Ra=0.0025;%Average surface roughness,mm
s=0.0025;%Standard deviation of the caliper,mm, proposed by schaffrath
RA=Ra+s;%unit mm

Eini=27;% initial modulus
S=80;

%B0=62.6759;
B0=0;
B1=((m0.^2)*(L.^2)*(Rr))./n0;
B2=((m0.^2)*(L.^2))./(4*(n0.^2));

while i<=100

     z0=z2-(((z1.^3)./(z1.*Eini./S+2*RA))-
(((((p+1)*4*(RA.^2))./A0*((B0+B1*z2-
B2*(z2.^2)).^(0.5))*z2))./(z2*Eini./S+d-4*RA))).*(0-
(p+1)*4*((RA).^2)./A0*((((0.5*((B0+B1*z2-B2*(z2.^2)).^(-0.5))*(B1-
2*B2*z2)*z2+((B0+B1*z2-B2*(z2.^2)).^(0.5)))*(z2*Eini./S+d-4*RA))-
(((B0+B1*z2-B2*(z2.^2)).^(0.5))*z2*Eini./S)).*((z2*Eini./S+d-4*RA).^(2))));

    if abs(z0-z2)>0.000001
        z2=z0;
    else break
    end
    i=i+1;
end
B1
B2
z2
z1
z=(2*z1+z2)
c=2*z1/(2*z1+z2)
```

A5. Newton-Raphson method - multiple sheets

```
clc
clear
z2=0.00005; %the initial value of the root
i=0;

p=150;%number of the sheets
m=2.6; %the total deformation z
```

```
A0=pi*9;%nominal contact area mm2
d=0.0847;% thickness of paper mm
L=0.885;% length of the fiber unit mm
Rr=30;%unit mm
m0=1778;
n0=4;

%Ra=0.0025;
%s=0.0025;
%RA=Ra+s;%unit mm

Rz=0.01;
RA=Rz./2;

B0=0;
%B0=62.6759;
B1=((m0.^2)*(L.^2)*Rr)./n0;
B2=((m0.^2)*(L.^2))./(4*(n0.^2));

while i<=100

    z0=z2-((p*2)*(((16*(RA.^3)./(A0*(d-4*RA))).^(1/3))*(B0+B1*z2-
B2*(z2.^2)).^(1/6)).*(z2.^(1/3))+p*z2-m)./((p*2)*((16*(RA.^3)./(A0*(d-
4*RA))).^(1/3))*((1/6)*((B0+B1*z2-B2*(z2.^2)).^(-5/6)).*(B1-
B2*2*z2).*(z2.^(1/3))+((B0+B1*z2-B2*(z2.^2)).^(1/6))*(1/3)*(z2.^(-
2/3)))+p);
    if abs(z0-z2)>0.0001
        z2=z0;
    else break
    end
    i=i+1;
end

z2
z1=(m-p*z2)/(p*2)

c=2*p*z1/m
```

A6. Relationship between z_1 and z - based on Hooke's law

```
z1=[0 0.0024 0.0046 0.0067 0.0087 0.0105 0.0123 0.0140 0.0156 0.0172 0.0188
0.0202 0.0217];
z=[0  0.005  0.010  0.015  0.020  0.025  0.030  0.035  0.040  0.045  0.050  0.055
0.060];
plot(z,z1,'bo')
```

A7. Relationship between z_1 and z - based on Paetow's method

```
z1=[0 0.0024 0.0046 0.0067 0.0087 0.0105 0.0123 0.0140 0.0156 0.0172 0.0188
0.0202 0.0217];
```

```
z=[0 0.005 0.0099 0.0148 0.0197 0.0243 0.0291 0.0337 0.0382 0.0427 0.0474
0.0516 0.0561];
plot(z,z1,'bo')
```

A8. Relationship between z_1 and z - multiple sheets

```
clc
clear

%z8=[0 0.0012 0.0024 0.0035 0.0047 0.0057 0.0067 0.0077 0.0087 0.0096
0.0105 0.0115 0.0123];
%z=0:0.01:0.12;
%plot(z,z8,'bo')

%z12=[0 0.0012 0.0024 0.0035 0.0047 0.0057 0.0067 0.0077 0.0087 0.0096
0.0105];
%z=[0 0.03 0.06 0.09 0.12 0.15 0.18 0.21 0.24 0.27 0.3];
%plot(z,z12,'bo')

%z16=[0 0.0012 0.0024 0.0035 0.0047 0.0057 0.0067 0.0077 0.0087 0.0096];
%z=[0 0.04 0.08 0.12 0.16 0.20 0.24 0.28 0.32 0.36];
%plot(z,z16,'bo')

%z20=[0 0.0012 0.0024 0.0035 0.0047 0.0057 0.0067 0.0077 0.0087];
%z=[0 0.05 0.1 0.15 0.2 0.25 0.3 0.35 0.4 ];
%plot(z,z20,'bo')

%z24=[0 0.0010 0.0021 0.0030 0.0039 0.0048 0.0057 0.0065 0.0074 0.0082
0.0090];
%z=[0 0.05 0.1 0.15 0.2 0.25 0.3 0.35 0.4 0.45 0.5];
%plot(z,z24,'bo')

%z48=[0 0.001 0.0015 0.0021 0.0025 0.0030 0.0034 0.0039 0.0044 0.0048
0.0052 0.0057 0.0061 0.0065];
%z=[0 0.1 0.15 0.2 0.25 0.3 0.35 0.4 0.45 0.5 0.55 0.6 0.65 0.7];
%plot(z,z48,'bo')

%z80=[0 0.0009 0.0018 0.0027 0.0035 0.0044 0.0052 0.0059 0.0067 0.0075
0.0082 0.0089 0.0096];
%z=0:0.15:1.8;
%plot(z,z80,'bo')

%z90=[0 0.0008 0.0016 0.0024 0.0032 0.0039 0.0047 0.0053 0.0060 0.0067
0.0074 0.0080 0.0087 ];
%z=0:0.15:1.8;
%plot(z,z90,'bo')

%z100=[0 0.00073 0.0015 0.0022 0.0029 0.0035 0.0042 0.0049 0.0055 0.0061
0.0067 0.0073 0.0079];
%z=0:0.15:1.8;
%plot(z,z100,'bo')

%z110=[0 0.00066 0.0013 0.0020 0.0026 0.0032 0.0038 0.0045 0.0051 0.0056
0.0061 0.0067 0.0073 ];
```

```
%z=0:0.15:1.8;
%plot(z,z110,'bo')

%z120=[0  0.0006  0.0012  0.0019  0.0024  0.0030  0.0035  0.0041  0.0047  0.0052
0.0057 0.0062 0.0067];
%z=0:0.15:1.8;
%plot(z,z120,'bo')

%z130=[0  0.00055  0.0011  0.0017  0.0023  0.0028  0.0033  0.0038  0.0043  0.0048
0.0053 0.0058 0.0062 0.0067 0.0072];
%z=0:0.15:2.1;
%plot(z,z130,'bo')

%z140=[0  0.0007  0.0014  0.0021  0.0028  0.0034  0.0040  0.0047  0.0052  0.0058
0.0064 0.0070];
%z=0:0.2:2.2;
%plot(z,z140,'bo')

%z150=[0  0.00064  0.0013  0.0020  0.0026  0.0032  0.0038  0.0044  0.0049  0.0055
0.0060 0.0066 0.0071 0.0076];
%z=0:0.2:2.6;
%plot(z,z150,'bo')

z160=[0  0.0006  0.0012  0.0018  0.0024  0.0030  0.0035  0.0041  0.0047  0.0052
0.0057 0.0062 0.0067 0.0072 0.0077 0.0082];
z=0:0.2:3.0;
plot(z,z160,'bo')
```

A9. Force-deformation - based on Hooke's law

```
clc
clear
z=0:0.001:0.015; % total deformation
A0=28.2743334; %contact area
Ra=0.005;       %surface thickness parameter

e=27;        %E-modulus
d=0.0847;

a2=z./d;

%y1=(1/(8*(Ra.^3)))*A0.*e.*(0.36.*z+0.001).^(3);  %linear curve fitting one
sheet
y1=(1/(8*(Ra.^3)))*A0.*e.*(17.*z.^3-3.1.*z.^2+0.49.*z+0.000016).^(3);
%cubic curve fitting one sheet

plot(z,y1,'k-')
hold on
```

A10. Force-deformation - based on Paetow's method

```
clc
clear
z=0:0.00001:0.015; % total deformation
A0=28.2743334; %contact area

RA=0.005;       %surface thickness parameter

e=27;        %E-modulus
S=80;
d=0.0847;

a2=z./d;

%y1=A0.*e.*(0.38.*z+0.00078).^(3)./(((0.38.*z+0.00078).*e./S+2*RA)*4*RA*RA)
;  %linear curve fitting one sheet

y1=A0.*e.*(15.*(z.^3)-2.6*(z.^2)+0.49*z+0.000015).^(3)./(((15.*(z.^3)-
2.6*(z.^2)+0.49*z+0.000015).*e./S+2*RA)*4*RA*RA);  %cubic curve fitting one
sheet

plot(z,y1,'k-')
hold on
```

A11. Force-deformation - multiple sheets

```
clc
clear
z=0:0.0001:2.2; % total deformation
A0=28.2743334; %contact area
Ra=0.005;       %surface thickness parameter
e=27;        %E-modulus
d=0.0847;

%y1=(1/(8*(Ra.^3)))*A0.*e.*(0.36.*z+0.001).^(3);  %linear curve fitting one
sheet
y1=(1/(8*(Ra.^3)))*A0.*e.*(17.*(z.^3)-3.1*(z.^2)+0.49*z+0.0000016).^(3);
%cubic curve fitting one sheet

%y4=(1/(8*(Ra.^3)))*A0.*e.*(0.1.*z+0.00037).^(3);    %linear  curve  fitting
one sheet
y4=(1/(8*(Ra.^3)))*A0.*e.*(0.55.*(z.^3)-0.26*(z.^2)+0.13*z-0.000013).^(3);
%cubic curve fitting one sheet

%y8=(1/(8*(Ra.^3)))*A0.*e.*(0.051.*z+0.00037).^(3);   %linear curve fitting
one sheet
y8=(1/(8*(Ra.^3)))*A0.*e.*(0.069.*(z.^3)-0.064*(z.^2)+0.063*z-
0.000013).^(3);  %cubic curve fitting one sheet

%y12=(1/(8*(Ra.^3)))*A0.*e.*(0.035.*z+0.00027).^(3);  %linear curve fitting
one sheet
```

```
y12=(1/(8*(Ra.^3)))*A0.*e.*(0.01.*(z.^3)-0.025*(z.^2)+0.042*z-
0.0000098).^(3);  %cubic curve fitting one sheet

%y16=(1/(8*(Ra.^3)))*A0.*e.*(0.027.*z+0.00022).^(3);  %linear curve fitting
one sheet
y16=(1/(8*(Ra.^3)))*A0.*e.*(0.0046.*(z.^3)-0.014*(z.^2)+0.031*z-
0.00001).^(3);  %cubic curve fitting one sheet

%y20=(1/(8*(Ra.^3)))*A0.*e.*(0.022.*z+0.00017).^(3);  %linear curve fitting
one sheet
y20=(1/(8*(Ra.^3)))*A0.*e.*(0.004.*(z.^3)-0.0099*(z.^2)+0.025*z-
0.000012).^(3);  %cubic curve fitting one sheet

%y24=(1/(8*(Ra.^3)))*A0.*e.*(0.018.*z+0.00021).^(3);  %linear curve fitting
one sheet
y24=(1/(8*(Ra.^3)))*A0.*e.*(0.007.*(z.^3)-0.01*(z.^2)+0.021*z-
0.0000049).^(3);  %cubic curve fitting one sheet

%y32=(1/(8*(Ra.^3)))*A0.*e.*(0.014.*z+0.00015).^(3);  %linear curve fitting
one sheet
y32=(1/(8*(Ra.^3)))*A0.*e.*(0.00068.*(z.^3)-0.0041*(z.^2)+0.016*z-
0.0000099).^(3);  %cubic curve fitting one sheet

%y48=(1/(8*(Ra.^3)))*A0.*e.*(0.0093.*z+0.00014).^(3);       %linear    curve
fitting one sheet
y48=(1/(8*(Ra.^3)))*A0.*e.*(0.00049.*(z.^3)-0.0022*(z.^2)+0.011*z-
0.0000094).^(3);  %cubic curve fitting one sheet

%y72=(1/(8*(Ra.^3)))*A0.*e.*(0.0061.*z+0.00016).^(3);       %linear    curve
fitting one sheet
y72=(1/(8*(Ra.^3)))*A0.*e.*(0.00047.*(z.^3)-0.0015*(z.^2)+0.0073*z-
0.0000076).^(3);  %cubic curve fitting one sheet

%y80=(1/(8*(Ra.^3)))*A0.*e.*(0.0053.*z+0.00023).^(3);       %linear    curve
fitting one sheet
y80=(1/(8*(Ra.^3)))*A0.*e.*(0.000035.*(z.^3)-0.00055*(z.^2)+0.0062*z-
0.0000088).^(3);  %cubic curve fitting one sheet

%y90=(1/(8*(Ra.^3)))*A0.*e.*(0.0048.*z+0.00019).^(3);       %linear    curve
fitting one sheet
y90=(1/(8*(Ra.^3)))*A0.*e.*(0.00011.*(z.^3)-0.00067*(z.^2)+0.0057*z-
0.000022).^(3);  %cubic curve fitting one sheet

%y100=(1/(8*(Ra.^3)))*A0.*e.*(0.0044.*z+0.00018).^(3);      %linear    curve
fitting one sheet
y100=(1/(8*(Ra.^3)))*A0.*e.*(0.00006.*(z.^3)-0.0005*(z.^2)+0.0051*z-
0.0000026).^(3);  %cubic curve fitting one sheet

%y110=(1/(8*(Ra.^3)))*A0.*e.*(0.004.*z+0.00012).^(3);       %linear    curve
fitting one sheet
y110=(1/(8*(Ra.^3)))*A0.*e.*(-0.000000000000000023.*(z.^3)-
0.00027*(z.^2)+0.0045*z-0.000009).^(3);  %cubic curve fitting one sheet

%y120=(1/(8*(Ra.^3)))*A0.*e.*(0.0037.*z+0.00012).^(3);      %linear    curve
fitting one sheet
y120=(1/(8*(Ra.^3)))*A0.*e.*(-0.000017.*(z.^3)-0.00022*(z.^2)+0.0042*z-
0.0000049).^(3);  %cubic curve fitting one sheet
```

```
%y130=(1/(8*(Ra.^3)))*A0.*e.*(0.0034.*z+0.00014).^(3);      %linear   curve
fitting one sheet
y130=(1/(8*(Ra.^3)))*A0.*e.*(0.000067.*(z.^3)-0.00043*(z.^2)+0.004*z-
0.000027).^(3);  %cubic curve fitting one sheet

%y140=(1/(8*(Ra.^3)))*A0.*e.*(0.0032.*z+0.00015).^(3);      %linear   curve
fitting one sheet
y140=(1/(8*(Ra.^3)))*A0.*e.*(0.00006.*(z.^3)-0.00039*(z.^2)+0.0038*z-
0.000019).^(3);  %cubic curve fitting one sheet

%y150=(1/(8*(Ra.^3)))*A0.*e.*(0.0029.*z+0.00018).^(3);      %linear   curve
fitting one sheet
y150=(1/(8*(Ra.^3)))*A0.*e.*(0.000026.*(z.^3)-0.00027*(z.^2)+0.0035*z-
0.000019).^(3);  %cubic curve fitting one sheet

%y160=(1/(8*(Ra.^3)))*A0.*e.*(0.0027.*z+0.00017).^(3);      %linear   curve
fitting one sheet
y160=(1/(8*(Ra.^3)))*A0.*e.*(0.000039.*(z.^3)-0.00015*(z.^2)+0.0031*z-
0.000017).^(3);  %cubic curve fitting one sheet

%plot(z,y1,'r-',z,y4,'r-',z,y8,'r-',z,y12,'r-',z,y16,'r-',z,y20,'r-
',z,y24,'r-',z,y32,'r-',z,y48,'r-',z,y72,'r-',z,y80,'r-',z,y100,'r-
',z,y120,'r-',z,y140,'r-',z,y160,'r-',z,y90,'r-',z,y110,'r-',z,y130,'r-
',z,y150,'r-')
%hold on

plot(z,y1,'b-',z,y4,'b-',z,y8,'b-',z,y12,'b-',z,y16,'b-',z,y20,'b-
',z,y24,'b-',z,y32,'b-',z,y48,'b-',z,y72,'b-',z,y80,'b-',z,y100,'b-
',z,y120,'b-',z,y140,'b-',z,y160,'b-',z,y90,'b-',z,y110,'b-',z,y130,'b-
',z,y150,'b-')
hold on
```

A12. Percentages of different contact deformations

```
clc
clear
n=[1 2 4 8 12 16 20 24 32 48 72 80 100 120 140 160];
zn=[0.0125  0.0195  0.0406  0.0855  0.1299  0.16655  0.21640  0.25115  0.35230
0.52665 0.77800 0.88400 1.09045 1.29895 1.44415 1.58225];

z1=0.0057;
z2=0.0011;
z3=(zn-2.*z1-n.*z2)./(n-1)
a=2*z1
b=z2.*n
c=z3.*(n-1)

a1=a./zn
b1=b./zn
c1=c./zn

plot(n,a1,'ro-',n,b1,'g+-',n,c1,'b*-')
%plot(n,z3,'bo-')
```

```
%plot(n,zn,'bo-')
```

A13. Force-deformation of multiple sheets

```
clc
clear

ey= 0.1393;
n=150;%number of sheets

dy=0.6357*(exp(13.5392*ey)-1);
er=0.49*ey-0.027;
b=94.3930*ezp(-11.9827*ey)+12.2313;
a=dy./((exp(b*ey)-exp(b*er)));

z1=0:0.0001:ey;
y1=0.6357*(exp(13.5392*z1)-1);%loading process is expressed by using
exponential curve fitting
%plot(z1*0.0847,y1*pi*9,'r')
%hold on
z11=2.35*0.001*((y1*pi*9).^(1/3))*n;
plot(z11,y1*pi*9,'r')%for paper stacks 72sheets loading
hold on

z2=er:0.0001:ey;
y2=(a*exp(b*z2)-a*exp(b*er));
%plot(z2*0.0847,y2*pi*9,'r')
%hold on

plot(((-
1.61*0.001.*((y2*9*pi).^(0.5)))+5.83*0.001.*((y2*9*pi).^(1/3)))*n,y2*(9*pi)
,'r')%for paper stacks 72sheets unloading
hold on

%plot((-1.41*0.001.*
((y2*9*pi).^(0.5)))+5.43*0.001.*((y2*9*pi).^(1/3))*n,y2*(9*pi),'b')%for
paper stacks 72sheets unloading
%hold on
```

A14. ANSYS linear simulation program

```
/prep7

!*++++++++++++++++++++
!* Define Element Types
!*++++++++++++++++++++
et,1,185
et,2,195

!*++++++++++++++++++++++++++++++++++++
!* Define Linear Elastic Material Type 1
```

```
!*++++++++++++++++++++++++++++++++++++
mp,ex,1,2.1E12
mp,nuxy,1,0.0

!*++++++++++++++++++++++++++++++++++++++++++++++++
!* Define Initial Gap, Stable Stiffness, Stress Cap
!*++++++++++++++++++++++++++++++++++++++++++++++++
delta0 = 0.00
stiff0 = 0.0
scap   = 1.0
tb,gasket,2,,,para
tbdata, 1,delta0,stiff0,scap

!*++++++++++++++++++++++++++++++
!* Define Gasket Compression Curve
!*++++++++++++++++++++++++++++++
tb,gask,2,1,16,comp
tbpt,,0.100E-05,149662.869003885
tbpt,,0.205E-05,243122.792763698
tbpt,,0.300E-05,364887.695071591
tbpt,,0.400E-05,551490.352165534
tbpt,,0.500E-05,764320.901774533
tbpt,,0.600E-05,1049450.16754459
tbpt,,0.700E-05,1425134.85685381
tbpt,,0.750E-05,1618640.15366377
tbpt,,0.800E-05,1823723.10996388
tbpt,,0.850E-05,2061426.78029527
tbpt,,0.900E-05,2301523.47853253
tbpt,,0.950E-05,2533097.18057815
tbpt,,1.000E-05,2797961.19050222
tbpt,,1.050E-05,3101356.77696261
tbpt,,1.100E-05,3395453.32207002
tbpt,,1.140E-05,3557765.06066314


!*++++++++++++++++++++++++++++++++++
!* Define Gasket Linear Unloading Curve
!*++++++++++++++++++++++++++++++++++
tb,gask,2,1,11,lunl
tbpt,,0.50E-05,58.7466805023243E+9
tbpt,,0.60E-05,122.573537662316E+9
tbpt,,0.70E-05,181.921548829786E+9
tbpt,,0.75E-05,302.16304920081E+9
tbpt,,0.80E-05,394.982453220161E+9
tbpt,,0.85E-05,407.720266301776E+9
tbpt,,0.90E-05,547.024959964766E+9
tbpt,,0.95E-05,709.459743366462E+9
tbpt,,1.00E-05,801.191105484347E+9
tbpt,,1.05E-05,904.725036016011E+9
tbpt,,1.14E-05,1266.77579122073E+9

!*++++++++++++++++++++++++++
!* List Gasket Material Model
!*++++++++++++++++++++++++++
tblist,gask,all

!*++++++++++++++++++
!* Define Parameters
!*++++++++++++++++++
```

```
n1    =  20
n2    =  n1*100
n3    =  n1
dis1  = -0.0000114
dis2  = -0.00000001
dp    = -2.0e7
elb   =  0.0005
elg   =  0.0000847

!*++++++++++++++++
!* Generate Nodes
!*++++++++++++++++
n,1,
n,2,0.0005
n,3,0.0005,0.0005
n,4,0.0,0.0005
ngen,2,4,1,4,,0.0,0.0,elb
ngen,2,8,1,4,,0.0,0.0,elb+elg
ngen,2,12,1,4,,0.0,0.0,2*elb+elg

!*++++++++++++++++++++++++++++++++++++++++
!* Generate Front and Back SOLID185 Element
!*++++++++++++++++++++++++++++++++++++++++
et,1,185,,1
mat,1
e,1,2,3,4,5,6,7,8
e,9,10,11,12,13,14,15,16

!*++++++++++++++++++++++++++++++++
!* Generate Middle INTER195 Element
!*++++++++++++++++++++++++++++++++
et,2,195,,
type,2
mat,2
e,5,6,7,8,9,10,11,12

!*++++++++++++++++++++++++++
!* Define Boundary Condition
!*++++++++++++++++++++++++++
nsel,s,loc,z
d,all,uz
nsel,all
nsel,s,loc,x
d,all,ux
nsel,all
nsel,s,loc,y
d,all,uy
nsel,all
finish

/solu
!*++++++++++++++++++++
!* Apply Displacement
!*++++++++++++++++++++
nsel,s,loc,z,elb*2+elg
d,all,uz,dis1
nsel,all

!*++++++++++++++++++++++++++++++++++++++++++++++
```

```
!* Solve First Load Step, Compress the Elements
!*++++++++++++++++++++++++++++++++++++++++++++
nsubst,n1,n2,n3
outres,all,all
outres,svar,all
solve

!*++++++++++++++++++++++++++++++++++++++++++
!* Solve Second Load Step, Open the Elements
!*++++++++++++++++++++++++++++++++++++++++++
nsubst,n1,n2,n3
outres,all,all
outres,svar,all
nsel,s,loc,z,elb*2+elg
d,all,uz,dis2
nall
solve
finish

!*++++++++++++++++++++++++
!* Postprocess the Results
!*++++++++++++++++++++++++
/post1
set,last
pres,s
pres,epto
pres,epel
prns,epel
finish

!*+++++++++++++++++++++++++++++++++++++++++++++
!* Post26, Print and Plot Gasket Element Results
!*+++++++++++++++++++++++++++++++++++++++++++++
/post26
esol,2,3, ,s,x,press
esol,3,3, ,epel,x,delta
add,4,2, , ,press,,,-1,   ! change sign for plotting
add,5,3,,,delta,,,-1,     ! change sign for plotting
prvar,2,3,4,5
xvar,5
plvar,4

finish
```

A15. ANSYS nonlinear simulation program

```
/prep7

!*++++++++++++++++++++
!* Define Element Types
!*++++++++++++++++++++
et,1,185
et,2,195

!*++++++++++++++++++++++++++++++++++
!* Define Linear Elastic Material Type 1
```

```
!*++++++++++++++++++++++++++++++++++++
mp,ex,1,1.25E12
mp,nuxy,1,0.0

!*++++++++++++++++++++++++++++++++++++++++++++++++
!* Define Initial Gap, Stable Stiffness, Stress Cap
!*++++++++++++++++++++++++++++++++++++++++++++++++
delta0 = 0.00
stiff0 = 0.0
scap   = 1.0
tb,gasket,2,,,para
tbdata, 1,delta0,stiff0,scap

!*++++++++++++++++++++++++++++++++
!* Define Gasket Compression Curve
!*++++++++++++++++++++++++++++++++
tb,gask,2,1,17,comp
tbpt,,0.100E-05,149662.869003885
tbpt,,0.205E-05,243122.792763698
tbpt,,0.300E-05,364887.695071591
tbpt,,0.400E-05,551490.352165534
tbpt,,0.500E-05,764320.901774533
tbpt,,0.600E-05,1049450.16754459
tbpt,,0.700E-05,1425134.85685381
tbpt,,0.750E-05,1618640.15366377
tbpt,,0.800E-05,1823723.10996388
tbpt,,0.850E-05,2061426.78029527
tbpt,,0.900E-05,2301523.47853253
tbpt,,0.950E-05,2533097.18057815
tbpt,,1.000E-05,2797961.19050222
tbpt,,1.050E-05,3101356.77696261
tbpt,,1.100E-05,3395453.32207002
tbpt,,1.120E-05,3550597.44352869
tbpt,,1.140E-05,3557765.06066314

!*++++++++++++++++++++++++++++++++++++
!* Define Gasket nonlinear Unloading Curve
!*++++++++++++++++++++++++++++++++++++
tb,gask,2,1,13,nunl
tbpt,,1.14E-05,3557765.06066314
tbpt,,1.10E-05,3051054.74417485
tbpt,,1.05E-05,2454697.26710089
tbpt,,1.00E-05,2002334.74909289
tbpt,,0.95E-05,1601739.19635071
tbpt,,0.90E-05,1247009.32466748
tbpt,,0.85E-05,973496.844685101
tbpt,,0.80E-05,769636.711534213
tbpt,,0.75E-05,572145.484924132
tbpt,,0.70E-05,421063.960323727
tbpt,,0.60E-05,239142.411493941
tbpt,,0.50E-05,116568.873831624
tbpt,,0.40E-05,57822.1933293001

!*++++++++++++++++++++++++++
!* List Gasket Material Model
!*++++++++++++++++++++++++++
tblist,gask,all

!*++++++++++++++++++
```

```
!* Define Parameters
!*++++++++++++++++++
n1    =  20
n2    =  n1*100
n3    =  n1
dis1  = -0.0000043
dis2  = -0.00000001
dp    = -2.0e7
elb   =  0.0005
elg   =  0.0000847

!*+++++++++++++++
!* Generate Nodes
!*+++++++++++++++
n,1,
n,2,0.0005
n,3,0.0005,0.0005
n,4,0.0,0.0005
ngen,2,4,1,4,,0.0,0.0,elb
ngen,2,8,1,4,,0.0,0.0,elb+elg
ngen,2,12,1,4,,0.0,0.0,2*elb+elg

!*++++++++++++++++++++++++++++++++++++++++
!* Generate Front and Back SOLID185 Element
!*++++++++++++++++++++++++++++++++++++++++
et,1,185,,1
mat,1
e,1,2,3,4,5,6,7,8
e,9,10,11,12,13,14,15,16

!*++++++++++++++++++++++++++++++++
!* Generate Middle INTER195 Element
!*++++++++++++++++++++++++++++++++
et,2,195,,
type,2
mat,2
e,5,6,7,8,9,10,11,12

!*++++++++++++++++++++++++++
!* Define Boundary Condition
!*++++++++++++++++++++++++++
nsel,s,loc,z
d,all,uz
nsel,all
nsel,s,loc,x
d,all,ux
nsel,all
nsel,s,loc,y
d,all,uy
nsel,all
finish

/solu

!*++++++++++++++++++++

!* Apply Displacement
!*++++++++++++++++++
```

```
nsel,s,loc,z,elb*2+elg
d,all,uz,dis1
nsel,all

!*++++++++++++++++++++++++++++++++++++++++++++
!* Solve First Load Step, Compress the Elements
!*++++++++++++++++++++++++++++++++++++++++++++
nsubst,n1,n2,n3
outres,all,all
outres,svar,all
solve

!*++++++++++++++++++++++++++++++++++++++++
!* Solve Second Load Step, Open the Elements
!*++++++++++++++++++++++++++++++++++++++++
nsubst,n1,n2,n3
outres,all,all
outres,svar,all
nsel,s,loc,z,elb*2+elg
d,all,uz,dis2
nall
solve
finish

!*++++++++++++++++++++++
!* Postprocess the Results
!*++++++++++++++++++++++
/post1
set,last
pres,s
pres,epto
pres,epel
prns,epel
finish

!*++++++++++++++++++++++++++++++++++++++++++++++
!* Post26, Print and Plot Gasket Element Results
!*++++++++++++++++++++++++++++++++++++++++++++++
/post26
esol,2,3, ,s,x,press
esol,3,3, ,epel,x,delta
add,4,2, , ,press,,,-1,   ! change sign for plotting
add,5,3,,,delta,,,-1,     ! change sign for plotting
prvar,2,3,4,5
xvar,5
plvar,4

finish
```

Curriculum Vitae

Personal Details:

Name, Surname:	Chen, Jian
Date of Birth:	23.10.1985
Place of Birth:	Laiwu, Shandong, China
Marital Status:	Married
Nationality::	Chinese

Education:

10/2012 – 11/2016	Ph.D. student (oral examination: 11/2016) Technische Universität Darmstadt, Department of Mechanical Engineering Darmstadt, Germany
09/2009 – 06/2012	Master's degree Southeast University, Department of Mechanical Engineering Nanjing, China
09/2005 – 07/2009	Bachelor's degree China Navy Aviation Engineering Institute, Department of Mechanical Engineering Qingdao, China

Awards:

12/2010	National Second-class prize in the National Postgraduate Mathematical Contest in Modeling (GMCM).
12/2007	Province First-class Prize in the Contemporary Undergraduate Mathematical Contest in Modeling (CUMCM).

Publications:

Jian Chen, Edgar Dörsam, Dieter Spiehl, Arash Hakimi Tehrani and Jun Da: *Stress-strain behavior of paper affected by the actual contact area*. Progress in paper physics seminar, Darmstadt, Hessen, Germany; 08/2016.

Jian Chen, Jann Neumann, Hans Martin Sauer, Edgar Dörsam: *A new FEM simulation method of paper materials by using a gasket model*. 42st International Research Conference of IARIGAI, Helsinki, Finnland; 09/ 2015.

Jian Chen, Jann Neumann, Edgar Dörsam: *Investigation on deformation behavior of paper in Z-direction*. 2014 Progress in paper physics seminar, Raleigh, North Carolina, USA; 09/ 2014.